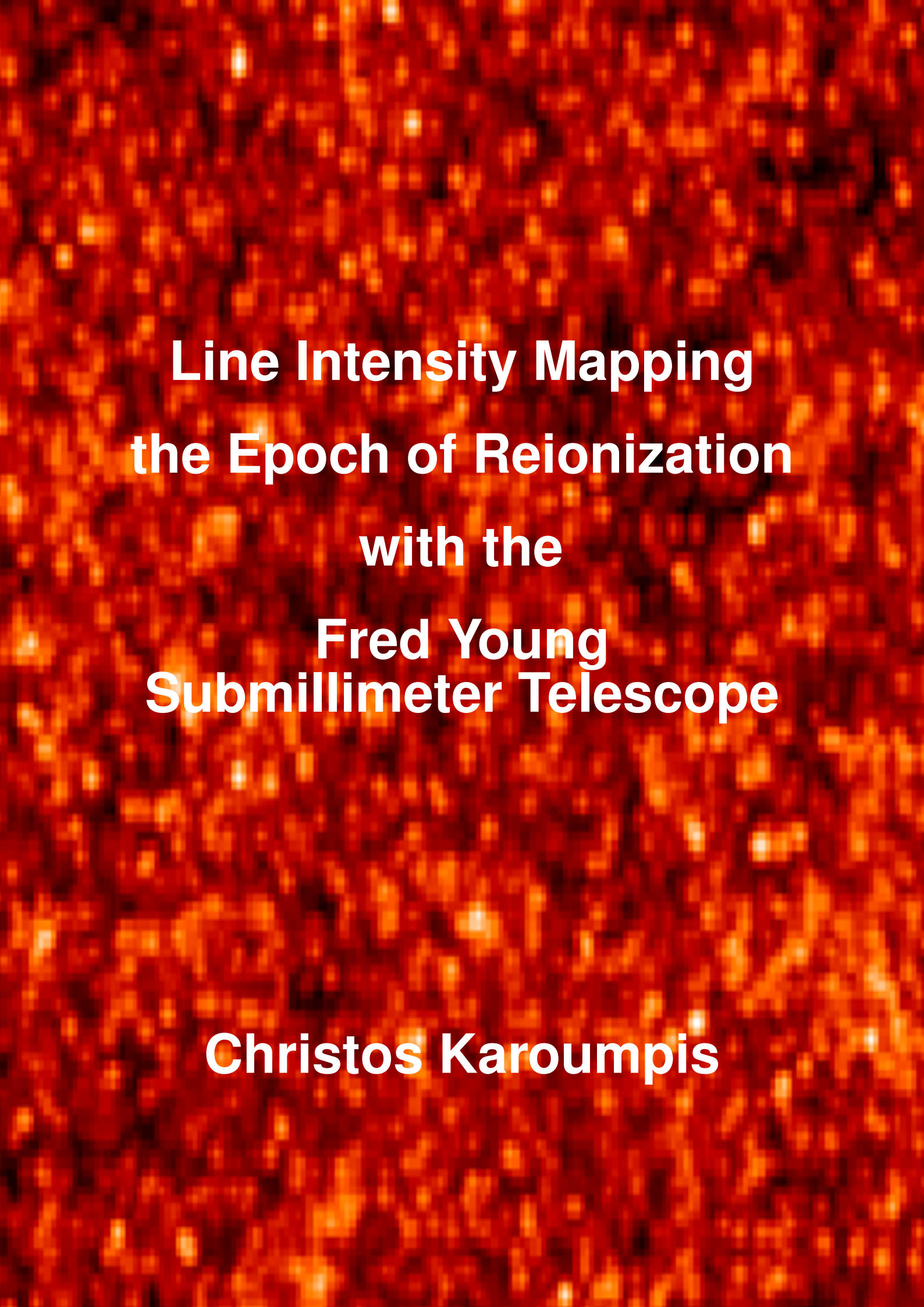
Line Intensity Mapping
the Epoch of Reionization
with the
Fred Young
Submillimeter Telescope
Christos Karoumpis

Line intensity mapping the epoch of reionization with the Fred Young Submillimeter Telescope

Dissertation
zur
Erlangung des Doktorgrades (Dr. rer. nat.)
der
Mathematisch-Naturwissenschaftlichen Fakultät
der
Rheinischen Friedrich-Wilhelms-Universität Bonn

vorgelegt von
Christos Karoumpis
aus
Thessaloniki, Griechenland

Bonn 2024

Angefertigt mit Genehmigung der Mathematisch-Naturwissenschaftlichen Fakultät
der Rheinischen Friedrich-Wilhelms-Universität Bonn

Gutachter/ Betreuer:	Prof. Dr. Frank Bertoldi
Gutachter:	Prof. Dr. Cristiano Porciani
Tag der Promotion:	15.07.2025
Erscheinungsjahr:	2025

To my mother and father, Areti and Giorgos

Look down into the abysmal distances!– attempt to force the gaze down the multitudinous vistas of the stars, as we sweep slowly through them thus–and thus–and thus! Even the spiritual vision, is it not at all points arrested by the continuous golden walls of the universe?–the walls of the myriads of the shining bodies that mere number has appeared to blend into unity?

Edgar Alan Poe, The Power of Words

Abstract

The baryonic matter in the universe is primarily hydrogen and helium gas, which existed in a neutral atomic state for approximately 400 thousand years following the Big Bang. With the formation of the first galaxies, their ionizing far-UV radiation initiated the ionization of intergalactic hydrogen, and later of helium. The ionization of hydrogen occurred between approximately 300 to 1000 million years after the Big Bang (redshift 11 to 6), a period referred to as the Epoch of Reionization (EoR). The majority of the early galaxies responsible for the reionization are too faint to be detected individually by current observational methods. However, line intensity mapping (LIM) is a novel technique that complements traditional galaxy surveys by capturing the aggregated emission from galaxies within a particular volume in both angular and frequency space, including those too faint to be detected individually.

This thesis develops models for forecasts of observations with a forthcoming LIM survey at 205 to 440 GHz using the Fred Young Submillimeter Telescope (FYST). Specifically, we predict the power spectrum (PS) of the singly ionized carbon, [CII] 158 μm (1900.5 GHz), fine-structure line emission from EoR galaxies. Our model is based on the IllustrisTNG300 hydrodynamic simulation. We find that a detection of the galaxy PS would be possible at redshift bins $z = 3.4 - 3.9$, $4.1 - 4.8$, $5.3 - 6.3$, and a detection may be possible at $z = 6.8 - 8.3$.

However, our predictions did not account for the detrimental, contaminating effect of carbon monoxide (CO) rotational line emission from lower-redshift (foreground) galaxies. These lines overlap in frequency with the higher redshift [CII] emission, and their signal must be separated or suppressed in order to detect the [CII] PS. The second part of this thesis also models the CO emission and evaluates the effectiveness of a foreground masking technique. Our findings indicate that [CII] emission dominates over CO emission above 300 GHz. However, extensive masking is necessary at lower frequencies to detect [CII]. We anticipate the recovery of the [CII] PS at $z = 3.4 - 3.9$ and $z = 4.1 - 4.8$, and likely also at $z = 5.3 - 6.3$. However, at $z = 6.8 - 8.3$ this is most challenging, necessitating the development of more effective strategies.

List of Publications

1 Relevant first author publications

This dissertation research project resulted in two first-author papers, one published in Astronomy & Astrophysics, and another submitted and currently under review in the same journal.

1. **Karoumpis C.**, Magnelli B., Romano-Díaz E., Haslbauer M., and Bertoldi F. (2022), *[CII] line intensity mapping the epoch of reionization with the Prime-Cam on FYST I. Line intensity mapping predictions using the Illustris TNG hydrodynamical simulation*, Astronomy & Astrophysics, 659, A12. DOI: https://doi.org/10.1051/0004-6361/202141293

   Author's contribution: Under the supervision of Magnelli and Bertoldi, Karoumpis conducted the scientific analysis and wrote most of the paper. The other co-authors contributed to the interpretation of the results and provided comments and revisions to the final manuscript. The refereed article is reproduced in Appendix A, while the open access version is available at arXiv:2111.12847.

2. **Karoumpis C.**, Magnelli B., Romano-Díaz E., Garcia K., Dev A., Clarke J., Wang T.-M, Bădescu T., and Bertoldi F. (2024), *[CII] line intensity mapping the epoch of reionization with the Prime-Cam on FYST. II. CO foreground masking based on an external catalog*, Astronomy & Astrophysics, submitted.

   Author's contribution: Under the guidance of Magnelli and Bertoldi, Karoumpis performed the scientific analysis and wrote most of the paper. The other co-authors assisted with the interpretation of the results and offered comments and revisions to the final manuscript. The article is reproduced in Appendix B, while the open access version is available at arXiv:2410.17330.

2 Relevant co-authored publications

The following lists publications that are complementary and related to the results and analysis presented in this dissertation. Karoumpis contributed to these papers throughout his thesis research period, but they are not part of this dissertation.

1. **CCAT-Prime Collaboration et al.** (2022) *CCAT-prime Collaboration: Science Goals and Forecasts with Prime-Cam on the Fred Young Submillimeter Telescope*, The Astrophysical

Journal Supplement Series, Volume 264, Number 1. DOI: http://doi.org/10.3847/1538-4365/ac9838

Author's contribution: Karoumpis produce part of the plots and the text of the section "4. Reionization, Structure Growth, and Galaxy Emergence through Line-intensity Mapping". An open access version is available at arXiv:2107.10364v3.

2. **Clarke J.**, Karoumpis C., Riechers D., Magnelli B., Okada Y., Dev A., Nikola T., Bertoldi F. (2024) *[CII] luminosity models and large-scale image cubes based on COSMOS 2020 and ALPINE-ALMA [CII] data back to the epoch of reionisation.*, Astronomy & Astrophysics, 689, A101. DOI: https://doi.org/10.1051/0004-6361/202450300

   Author's contribution: Karoumpis provide the script for the power spectrum calculation and assisted with the interpretation of the results and offered comments and revisions to the final manuscript. Astronomy & Astrophysics, submitted. An open access version is available at arxiv:2404.05352v3.

Contents

CHAPTER 1

Introduction

From Galileo's pioneering use of the telescope to the advanced capabilities of the Atacama Large Millimeter/submillimeter Array (ALMA) and the James Webb Space Telescope (JWST), telescopes have continually advanced in resolution, enabling increasingly detailed studies of individual celestial objects. Over decades, galaxy surveys—designed to map the distribution and properties of galaxies—have provided many insights into the formation of early stars and galaxies. However, these findings are predominantly based on rare, super-luminous galaxies, while numerous fainter galaxies, which may collectively contribute significantly to the overall radiation of the early universe, remain too faint to be individually detected in large numbers.

Here, submillimeter line intensity mapping (LIM, for a review Bernal & Kovetz 2022) emerges as a crucial technique that transcends the capabilities of traditional galaxy surveys by not observing individual galaxies but the aggregated emission from all galaxies within a particular volume, including those too faint to be detected individually. Instruments designed specifically for LIM, enable the collection of this aggregated emission over large volumes of space, providing a more comprehensive view of the galaxy evolution.

This thesis delves into the groundwork for one of the most ambitious forthcoming LIM surveys, to be conducted by the CCAT collaboration with its Fred Young Submillimeter Telescope (FYST CCAT-Prime Collaboration et al. 2023). FYST is a state-of-the-art submillimeter telescope and, along with the optical-infrared University of Tokyo Atacama Observatory, will be among the highest-altitude telescopes in the world, situated atop Cerro Chajnantor in Atacama, Chile. This location is among the most elevated and arid spots on the planet, providing exceptionally low water vapour for a substantial part of the year—a critical advantage for submillimeter and millimeter-wave astronomy.

With its 6-meter diameter, FYST is engineered to function across submillimeter to millimeter wavelengths (0.3-2 mm). Its lofty spot enables it to capture wavelengths (< 1 mm) that are typically absorbed by the atmospheric water vapor. Furthermore, its cutting-edge design facilitates fast and efficient wide-field-of-view sky mapping, achieving a mapping speed more than ten times faster than that of current facilities. Leveraging these capabilities, we have prepared an ambitious LIM survey targeting the bright submillimeter line [CII]. This line is pivotal for tracing early star formation in a statistically robust manner, offering unprecedented insights into the nascent epochs of the Universe (i.e., Stacey et al. 2018).

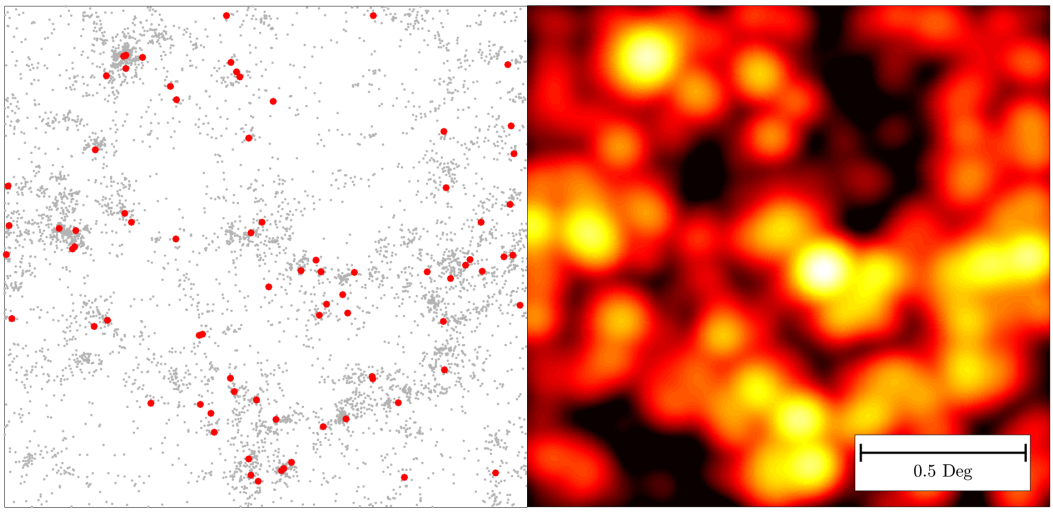

Figure 1.1: A simulated 2.5 deg^2 field with galaxy positions (left) and the corresponding CO intensity map (right), using luminosities from a Schechter function model (Breysse et al. 2016). Sources detectable with one hour of JVLA time are marked in red (see Li et al. 2016). This image demonstrates that line intensity mapping surveys are promising approaches to trace the entire galaxy population CO emission: while the VLA, with its 27 dishes, would need 4500 hours to cover the area and detect only about 1% of CO-emitting galaxies, a line intensity mapping experiment like COMAP, conducted by a single-dish telescope, needs only 1500 hours to produce a map of the intensity fluctuations of the field that traces the entirety of the CO-emitting galaxy population. Image from Kovetz et al. (2017) (courtesy of Patrick Breysse).

1.1 History of extragalactic background astronomy

The first contemplation of extragalactic background radiation – radiation of cosmic origin that due to technological limitations cannot be attributed to identifiable sources–likely began with Olbers's paradox (Olbers 1823), also known as the dark night paradox. This conundrum gained popularity in the 19th century, attracting attention from notable figures of the era such as Lord Kelvin (Kelvin 1901; Harrison 1986) and Edgar Allan Poe (Poe 1848, 1976), who each proposed solutions. The paradox poses the question of why the night sky is dark, or more formally, it challenges the notion of a static, infinitely old Universe filled with an infinite number of stars distributed across an infinite expanse, which logically would result in a sky that is perpetually bright.

The solution to this paradox came with the realization that the age of the Universe is finite and the Universe is not static but expanding, having originated from an event marking the beginning of both time and space itself through an event now known as the Big Bang (i.e., Gamow 1946). This foundational event underpins the Big Bang theory, which was further supported by the discovery of the cosmic microwave background (CMB) emission. This emission represents the radiation released when the Universe cooled from a hot plasma of subatomic particles to a state dominated by neutral hydrogen, with the expansion of the Universe shifting this radiation into the microwave frequency range, where it was detected by Penzias & Wilson (1965).

The discovery of the CMB, revealing that the Universe appears homogeneous and isotropic,

encouraged cosmologists to extend their research into other wavelengths, seeking contributions to the background radiation from the stars of galaxies—the original focus of Olbers's paradox. The theoretical work by Partridge & Peebles (1967), which proposed the possibility of detecting 'integrated background radiation' from young galaxies at infrared wavelengths, led many years later to observations by the COBE experiment, which marked the first detection of the cosmic infrared background (CIB) in the far-infrared spectrum (Puget et al. 1996; Fixsen et al. 1998; Hauser et al. 1998).

Today, it is well understood that the Cosmic Infrared Background (CIB), unlike the primordial Cosmic Microwave Background (CMB), originates from a more familiar source: the continuous thermal radiation from dust in star-forming galaxies (i.e., Dole et al. 2006; Lagache et al. 2003). Observations of the CIB provide insights into the clustering of galaxies and the underlying dark matter (DM) large-scale structure (see Sect. 1.3), while also constraining the rates of star formation and metal production over cosmic time, offering critical information about galaxies that are otherwise inaccessible through traditional surveys (i.e., Kashlinsky 2005; Pénin et al. 2012).

Today, it is well understood that the CIB, unlike the primordial CMB, originates from a more familiar source: the continuous thermal radiation from dust in star-forming galaxies (i.e., Dole et al. 2006; Lagache et al. 2003). Observations of the CIB thus provide insights not only into the clustering of galaxies and the underlying dark matter (DM) large-scale structure (see Sect. 1.3), but can also can be used to constrain the rates of star formation and metal production over cosmic time, offering critical information about galaxies inaccessible through traditional surveys (i.e., Kashlinsky 2005; Pénin et al. 2012).

However, this approach comes with the limitation of lacking direct line-of-sight information. Fortunately, galaxies emit not only continuum radiation but also atomic and molecular lines. The integrated emission from these lines produces not just angular but also spectral fluctuations, the latter offering valuable line-of-sight information.

LIM, an innovative technique suitable for deep and wide surveys, stands poised to unravel numerous unresolved questions in the realms of galaxy evolution and cosmology (Kovetz et al. 2019). In galaxy evolution, it provides insights into early star formation and its fuel—-the interstellar gas. Measurements with low sample variance from LIM will be crucial for constraining key parameters of early galaxy evolution, such as the star formation rate, the metallicity, and the gas mass of the galaxies. This deeper understanding will also help to better comprehend the impact that stars and galaxies had on the IGM, that lead to its phase transition from neutral to ionized during the EoR (Sect. 1.2). Moreover, for cosmology LIM has the potential to extend our knowledge into the dark sector of the early universe. It could trace the elusive Dark Matter, as the photons from its decays would be correlated with the underlying mass distribution, which can be inferred from galaxy surveys, weak-lensing surveys, or the intensity maps themselves (Bernal et al. 2021; Creque-Sarbinowski & Kamionkowski 2018). By mapping the evolution of the large-scale structure alongside galaxy evolution, LIM can help to refine models of DM, dark energy, modifications to Einstein's gravity, primordial non-Gaussianity, neutrinos, and light relics.

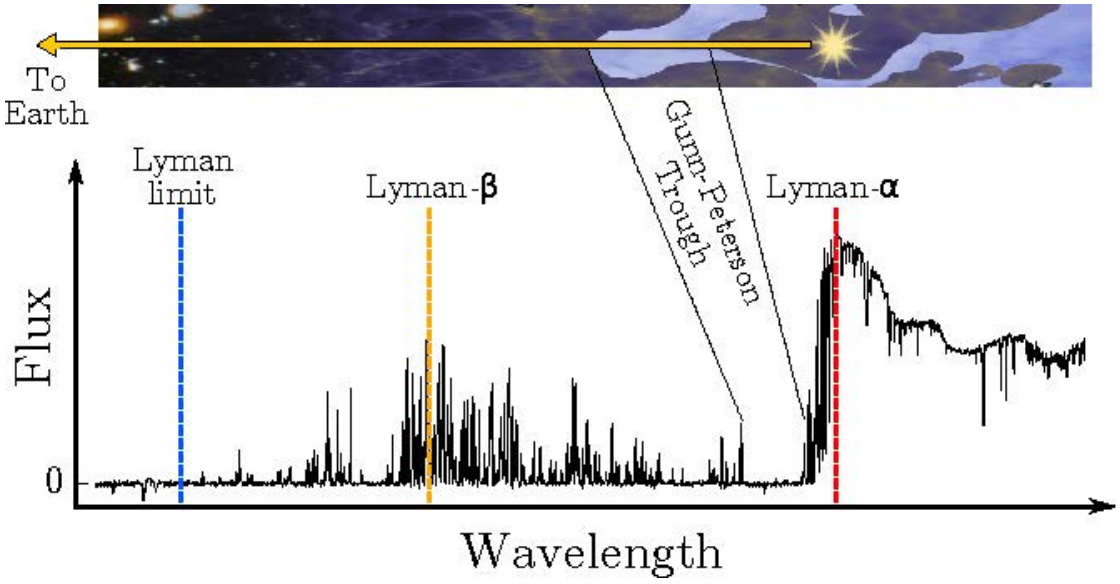

Figure 1.2: Typical emission spectrum of a redshift ~ 6 quasar (ULAS J1319+0959 at $z = 6.13$, based on Becker et al. 2015). The observed wavelength range is 620–950 nm, while the rest-frame wavelength range of the quasar is 87–133 nm. Emission from bright quasars can trace the ionization state of the intergalactic medium. Clouds of neutral hydrogen along the line of sight toward the quasar absorb at specific H recombination line frequencies, leaving absorption signatures in the quasar spectrum. In the UV, hydrogen absorbs in the s.c. Lyman series of transition lines, with Ly α ($\lambda = 121.5$ nm) being the most prominent, which is here seen as a broad emission line from the quasar. Ly α absorption from clouds at lower redshift form what is known as a Ly α forest. At $z > 5.5$ these absorption features become very strong, giving rise to a Gunn-Peterson trough from a high abundance of neutral hydrogen, which is evidence for the end of the Epoch of Reionization. Note that even the quasar Ly-α line has been mostly absorbed away on its blue side. Image from Wise (2019)

1.2 Early galaxies and the epoch of reionization

Since several years, we have been able to observe the impact that the first galaxies had on the intergalactic medium (IGM) by reionizing it. These observations are possible through studies of Lyman α line absorption, cosmic microwave background (CMB) distortions, and, in the future, the hydrogen hyperfine structure line. The hydrogen Lyman-alpha (Ly α) line, occurring at a wavelength of $\lambda_\alpha = 121.5$ nm, is the most prominent hydrogen recombination line, resulting from an electron transitioning from the $n = 2$ orbital state to the ground state. When the ultraviolet (UV) radiation from a high-redshift (z_Q) quasar—a type of galaxy exceptionally luminous due to an active supermassive black hole at its center—is redshifted to λ_α at a redshift $z < z_Q$, it gets absorbed if there is even a small amount of neutral hydrogen present (IGM neutral hydrogen fractions larger than 10^{-4}, assuming a uniform IGM Fan et al. 2006). Consequently, if there is neutral hydrogen between the quasar and the observer, photons with wavelengths shorter than λ_α in the rest frame of the quasar would be heavily absorbed. This results in a noticeable absorption in the observed spectrum of the quasar, characterized by very low flux, often approaching zero, at wavelengths shorter than $(1 + z_Q)\lambda_\alpha$. This creates what is known as the Gunn-Peterson (GP,

Gunn & Peterson 1965) trough (Fig. 1.2), which is accompanied by a truncation of the blue side of the broad Ly α emission line of the quasar.

Reionization also leaves its signature on the Cosmic Microwave Background (CMB, i.e., Planck Collaboration et al. 2016). Because of the reionization the IGM was filled with free electrons that could elastically scatter with the photons of the CMB (Thomson scattering). These interactions left signatures on the CMB by enhancing its polarization and suppressing its temperature fluctuations. These signatures can provide time-integral constraints on the evolution of ionized hydrogen fraction during the EoR.

The most promising upcoming way to trace the EoR is the LIM of the hydrogen 21 cm line. (i.e., Pritchard & Loeb 2012). The hyperfine transition line of neutral hydrogen at results from an electron spin flip in its electronic ground state. Although this has a very low transition probability, the high abundance of neutral hydrogen in the universe makes the 21 cm line one of the most prominent and easily detectable lines, one that can be observed in both emission and absorption. However, detecting the hyperfine transition line from the EoR is extremely challenging because galactic and extragalactic foreground emission components are four to five orders of magnitude stronger than the forecasted EoR signal. Despite these challenges, there have been recent results that include a tentative detection by the Experiment to Detect the Global Epoch of Reionization Signature (EDGES, Bowman et al. 2018) as well as signinficant constraints on the all-sky average power spectrum (PS) of the HI 21 cm line by the Hydrogen Epoch of Reionization Array (HERA, DeBoer et al. 2017) and the Shaped Antenna measurement of the background RAdio Spectrum 2 (SARAS2, Singh et al. 2018) experiments.

The phase transition from predominantly neutral to ionized hydrogen in the IGM coincides with the appearance of the first galaxies (e.g., Dayal & Ferrara 2018). Despite considerable debate about the role of active galactic nuclei (AGN) as significant sources of ionizing radiation (e.g., Hassan et al. 2018; Mitra et al. 2018; Garaldi et al. 2019), the prevailing models postulate that the transition began when UV emission from massive stars in the very first galaxies created ionized bubbles around them. The size of these bubbles (hundreds of kpc at $z = 8$ Lu et al. 2024) was limited by the density and clumping of the hydrogen in the IGM. As the gas density decreased with the expansion of the Universe and more galaxies formed, the bubbles grew (tens of Mpc at $z = 6.5$ Lu et al. 2024) and became more abundant, eventually (1 billion years after the Big Bang, $z \approx 6$) overlapping and filling the entire IGM. This process was not uniform throughout the Universe, as regions of higher overally density, where the most massive proto-galaxies formed, also contained a denser IGM that self-shielded from the ionizing UV emission, delaying the reionization in such regions. It is thought that reionization started from regions surrounding early low-mass galaxies, similar to those recently observed with the JWST through strong gravitational lenses (Atek et al. 2024). Since the current sample of such faint proto-galaxies is small, their gas content and star formation rates are largely unknown. In Sect. A, we show how different assumptions about the properties of such early galaxies lead to a wide range of predictions for the [CII] LIM signal that the FYST telescope will attempt to measure.

1.3 Modeling the [CII] and CO power spectra

1.3.1 Dark matter halo to galaxy connection

According to the standard cosmological model, ΛCDM, galaxies reside within larger structures known as dark matter (DM) halos—collections of DM particles orbiting within their own self-generated potential (García et al. 2023). These galaxies and their parent DM halos are organized into a complex, web-like pattern called the large-scale structure. The properties of DM halos significantly influence the evolution of galaxies. Notably, the relationship between the stellar mass of a galaxy and the mass of its host DM halo is crucial for understanding the efficiency of galaxy formation across different scales (Wechsler & Tinker 2018). This relationship is shaped by several fundamental physical processes that can either eject or heat gas, thereby inhibiting star formation and determining the observable characteristics of galaxies (e.g., Behroozi et al. 2019). In the case of smaller DM halos, the UV emission that reionized the early universe heated and dispersed the gas, challenging the ability of these halos to retain their gas essential for initiating star formation (Fig. 1.3). Moreover, stellar winds and supernovae can expel gas from these smaller halos, further hindering star formation by depleting the necessary material for new stellar generations. These mechanisms are particularly vital for comprehending the formation and evolution of the smallest galaxies of the Universe, such as ultra-faint dwarf galaxies. At the higher end of the mass spectrum, for halo masses above $10^{12} M_{\odot}$, the galaxies populating the most massive subset of the DM halos population, AGN have a significant impact. The energy released by AGN, originating from supermassive black holes at galaxy centers, can heat the surrounding gas, preventing it from cooling and collapsing into new stars (Fig. 1.3). This feedback mechanism is essential for modulating star formation in massive galaxies and elucidating the rarity of extremely massive, star-forming galaxies in the cosmos.

In the study of the connection between DM halos and galaxies, models can be broadly categorized into empirical and physical types. Empirical models leverage observational data to define the galaxy-halo relationship at a specific redshift, whereas physical models aim to capture the essence of galaxy formation by simulating or parameterizing key physical processes like gas cooling, star formation, and feedback mechanisms. This distinction is crucial for understanding the continuum these models occupy, as depicted in Figure 1.4. Moving rightward along this spectrum signifies a gradual decrease in the reliance on directly simulated physical processes, alongside an increase in the use of observational data to probe the nuances of the galaxy-halo connection. This transition, however, comes with a trade-off: the models tend to lose predictive power and their linkage to underlying physical laws becomes weaker. In the work presented here, we explore the extremes of this spectrum: the most empirical approach, which utilizes the halo occupation model through abundance matching, and the most physical approach, employing a hydrodynamic simulation. We employ the state-of-the-art Illustris TNG300 simulation, part of the broader IllustrisTNG suite of simulations, which incorporates all the aforementioned physical processes and more to simulate the evolution of galaxies on cosmological scales

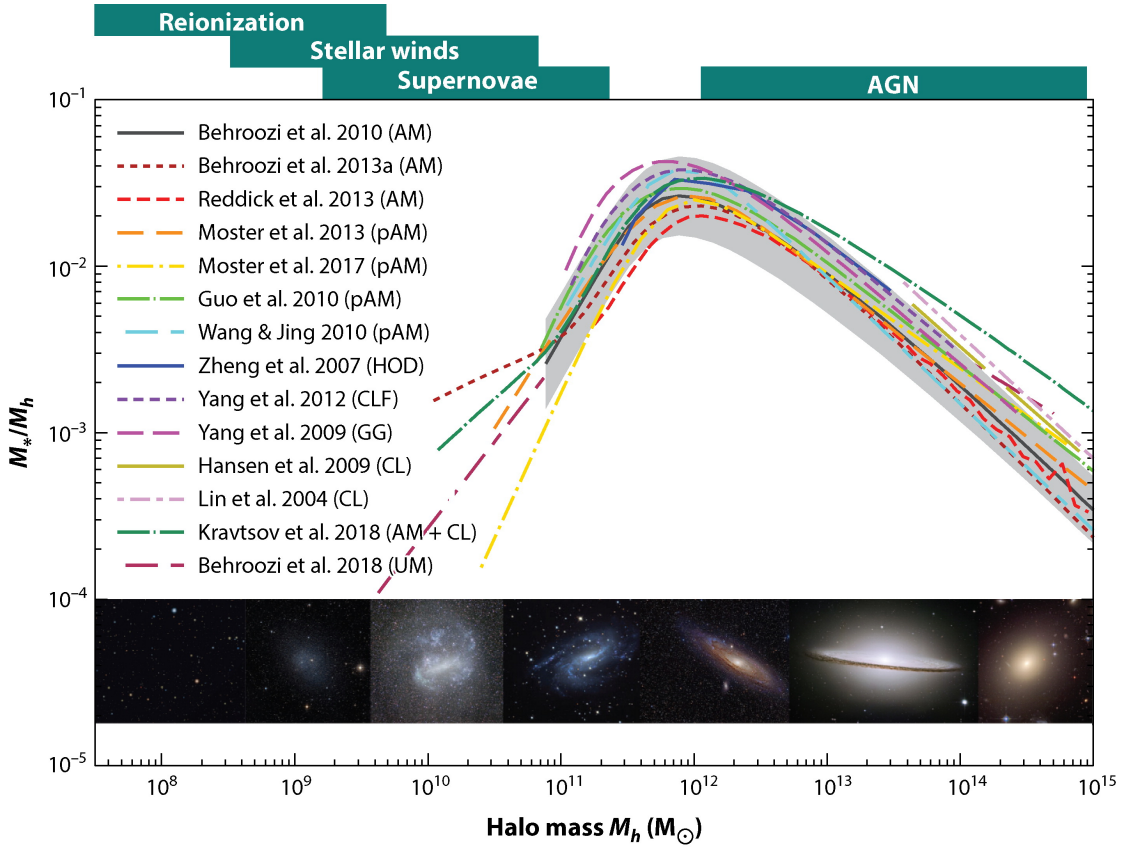

Wechsler RH, Tinker JL. 2018.
Annu. Rev. Astron. Astrophys. 56:435–87

Figure 1.3: Galaxy stellar mass to Dark Matter halo mass ratio as a function of halo mass at $z = 0$. Results are shown from a variety of methods to approximate this connection, including direct abundance matching Behroozi et al. (2010, 2013); Reddick et al. (2013), as well as parameterized abundance matching where relationships are defined through adjustable parameters to fit the stellar mass function and other observables Guo et al. (2010); Wang & Jing (2010); Moster et al. (2010, 2013). It also incorporates analyses of the halo occupation distribution (Zheng et al. 2007) and the conditional luminosity function (Yang et al. 2009, 2012), refined by two-point clustering data, and includes direct observations of central galaxies in galaxy groups and clusters Lin et al. (2004); Hansen et al. (2009); Yang et al. (2009); Kravtsov et al. (2018). The 'Universe Machine' is a comprehensive empirical model framework that tracks galaxy evolution over time, (Behroozi et al. 2019, referred to as Behroozi et al. 2018 in the plot). Upper insert: Key physical processes that may suppress star formation in galaxies across the different halo mass ranges. Lower insert: Typical galaxies residing within DM halos of given masses, illustrating the diversity of galactic structures. Plot from Wechsler & Tinker (2018) based on data compiled by Behroozi et al. (2019).

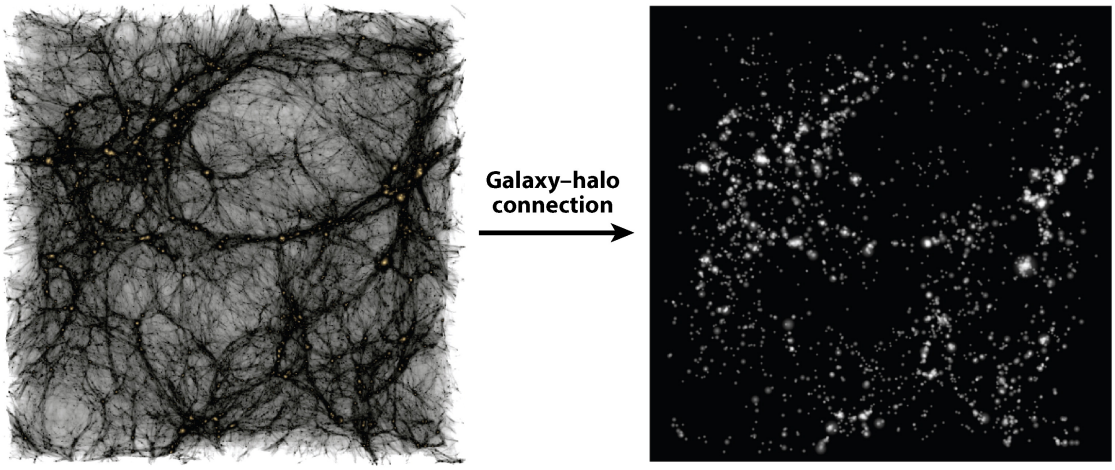

Approaches to modeling the galaxy–halo connection

Physical models ← → Empirical models

Hydrodynamical simulations	Semianalytic models	Empirical forward modeling	Subhalo abundance modeling	Halo occupation models
Simulate halos and gas; star formation and feedback recipes	Evolution of density peaks plus recipes for gas cooling, star formation, feedback	Evolution of density peaks plus parameterized star formation rates	Density peaks (halos and subhalos) plus assumptions about galaxy–(sub)halo connection	Collapsed objects (halos) plus model for distribution of galaxy number given host halo properties

Wechsler RH, Tinker JL. 2018.
Annu. Rev. Astron. Astrophys. 56:435–87

Figure 1.4: Lower panel: spectrum of approaches to the DM halo-galaxy connection. On the left, the most physically-based models, and towards the right the models more rely on observations rather than simulations or physical prescriptions, with the most empirical models on the very right. Upper left: DM distribution within a $90 \times 90 \times 30$ Mpc h^{-1} slice of a simulation. Upper right: galaxy distribution resulting from abundance matching the DM halos from the DM field on the left with observed galaxy data. Image from Wechsler & Tinker (2018).

1.3.2 IllustrisTNG suite of simulations

Hydrodynamical simulations are the most physical method for modeling the relationship between DM halos and galaxies. They uniquely integrate the gravitational forces of various matter components—DM, gas, stars, and black holes—alongside the magneto-hydrodynamical behavior of the gas. The IllustrisTNG project (Pillepich et al. 2018a) stands out as a comprehensive collection of large-scale cosmological simulations that embody this approach. As the evolutionary successor to the original Illustris initiative (Nelson et al. 2015), The Next Generation (TNG) simulations build upon their predecessor by incorporating an expanded spectrum of physical phenomena and leveraging advanced numerical techniques.

IllustrisTNG project has offered insights into the processes of galaxy formation and evolution, demonstrating the significant role of feedback mechanisms in shaping the size, morphology, and color of galaxies across time (i.e., Genel et al. 2018; Nelson et al. 2018; Tacchella et al. 2019). The simulations have furthered our understanding of the growth of supermassive black holes and their energetic feedback, which is essential for regulating star formation within galaxies and influencing the characteristics of the intra-cluster medium (i.e., Weinberger et al. 2017). Additionally, by modeling the evolution of magnetic fields, TNG has enriched our understanding of cosmic magnetism and its influence on cosmic dynamics.

The project encompasses simulations of different scales, with TNG50 being the one with the smallest volume (50^3 Mpc^3) but offering the highest mass resolution (smaller DM particle mass, $m_{\rm dm} = 4.5 \times 10^5$), ideal for studying the internal processes of galaxies (Pillepich et al. 2019). TNG100 provides a balance between volume (100^3 Mpc^3) and mass resolution ($m_{\rm dm} = 7.5 \times 10^6$), suitable for examining galaxy clusters and large-scale structures (Springel et al. 2018). TNG300, with its large volume (300^3 Mpc^3), is optimized for exploring the cosmic web and the large-scale structure of the Universe, despite its lower mass resolution ($m_{\rm dm} = 5.9 \times 10^7$) compared to TNG50 and TNG100 (Springel et al. 2018). By combining the results of the several simulations we can synthesize our understanding of physical processes across a spectrum of scales,from the scales of an individual galaxy to the scale of the large scale structure.

Despite the achievements of the IllustrisTNG project and hydrodynamical simulations in general, they are not without limitations, particularly concerning the treatment of processes that occur below their resolution limit, known as subgrid physics (Gabrielpillai et al. 2022). These simulations rely on subgrid models to approximate the effects of phenomena such as star formation, the growth of supermassive black holes, and feedback mechanisms from stars and AGN, which cannot be directly resolved due to computational constraints. The accuracy of these subgrid models is contingent upon our understanding of the underlying physics, which is often incomplete. Consequently, the results can be sensitive to the specific choices made in these models, introducing uncertainties into the predictions of the simulations.

Moreover, hydrodynamical simulations require substantial computational resources, especially as they strive for higher resolution and more complex physics. This limitation not only constrains the size and resolution of the simulated volumes but also limits the parameter space that can be explored. As a result, while these simulations provide invaluable insights into the non-linear evolution of the cosmos and the interplay between its various components, they are complemented by empirical models that offer alternative perspectives.

Empirical models, such as abundance matching, serve as valuable tools in astrophysical research

for several reasons. By directly linking observable properties of galaxies with the mass of their host DM halos based on the observed and simulated universe, abundance matching provides a straightforward and computationally efficient method to populate DM simulations with galaxies.

1.3.3 Abundance matching

The abundance matching method (i.e, Wechsler et al. 1998) is grounded in the principle that there is a monotonic relationship between certain properties of galaxies (like their stellar luminosity or SFR) and the mass of the DM halos in which they reside. Essentially, it assumes that the most luminous galaxies are found in the most massive halos. Halo mass functions derived from simulations are matched to stellar luminosity or star formation rate (SFR) functions obtained from observations to create mock populations of galaxies. The core of abundance matching is creating a one-to-one correspondence between galaxies and halos. This is done by ranking both the galaxies and halos by their chosen property (e.g., stellar luminosity or $V_{\rm max}$) and then matching them in descending order. The most luminous galaxy is matched to the most massive halo, the second most luminous galaxy to the second most massive halo, and so on.

Although, this process assumes that there are no inversions in the ranking order, realistically, the relationship between galaxy and halo properties is not perfectly monotonic and can exhibit scatter (Wechsler & Tinker 2018). To account for this, abundance matching models often include a scatter component, especially when matching properties like SFR, which can vary significantly even in halos of similar mass (i.e., Yue et al. 2015; Karoumpis et al. 2022). This scatter is modeled statistically, often as a log-normal distribution around the mean relation. The outcome of abundance matching is a mock catalog of galaxies with properties directly tied to the properties of their host DM halos.

Abundance matching is a technique grounded primarily in observational data, minimizing the reliance on extensive theoretical assumptions. However, its limitations stem directly from its dependency on deep, pencil-beam surveys (i.e., Bouwens et al. 2015). These surveys are inherently biased towards the detection of the brightest galaxies, while also being susceptible to sample variance due to their limited scope. Consequently, the extremes of the luminosity function (LF) — both the faint end, which remains largely unobserved, and the bright end, characterized by a sparse sample of galaxies — present reliability concerns. This bias affects the ability of the technique to accurately match galaxies with their corresponding DM halos, particularly for the least luminous galaxies that are underrepresented and the most luminous ones that are rare.

1.3.4 [CII] 158 μm emission from star-forming galaxies

To better understand the origin of the [CII] 158 μm emission from star-forming galaxies, it is helpful to briefly recall the quantum mechanical framework governing electron configurations, as it is crucial for understanding the mechanism behind the emission. The electron orbitals in atoms and ions are designated by the principal quantum number n (with values 1, 2, 3, ...) and the azimuthal quantum number l (with values 0, 1, 2, ...). These orbitals are typically labeled as 1s, 2s, 2p, 3s, 3p, 4s, 3d, 4p, continuing in this manner according to the increasing values of n and l. Each orbital state can accommodate $2(2l + 1)$ electrons, where the magnetic quantum number

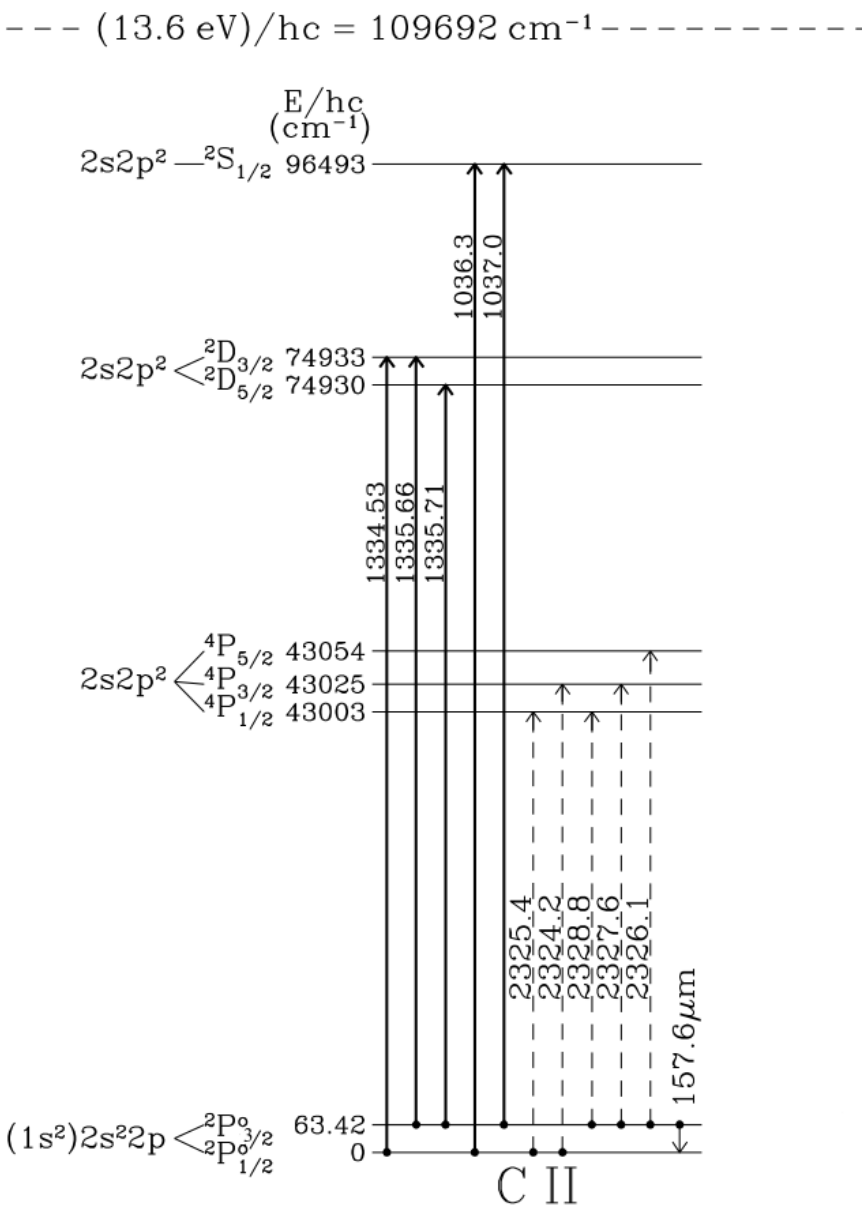

Figure 1.5: Energy level diagram for singly ionized carbon, CII. The transitions between these levels are indicated by vertical arrows, labeled with their respective wavelengths in micrometers. The prominent [CII]158μm fine structure line is an astrophysically important emission line. Together with the [OI]63mum line it is the most important probe of the warm, dense interstellar medium in star-forming galaxies, as both lines are the major cooling channels of gas that is radiatively heated by massive, young stars. Image from Draine (2011)

$m_z = m_l$ ranges from $-l$ to $+l$ and the spin quantum number m_s can be $\pm 1/2$. The azimuthal quantum number l satisfies the condition $0 \leq l < n$.

The total orbital quantum number L is the vector sum of the electron orbital angular momentum. It takes on values 0, 1, 2, 3 and higher integers, corresponding to the terms S, P, D, F, respectively. The total spin angular momentum, S, is the sum of the spin quantum numbers m_s of all electrons, which can result in $S = 0, 1/2, 1, 3/2, 2, 5/2, ...$ For singly ionized carbon, C^+, the electron configuration is $1s^2 2s^2 2p^1$, and the total orbital angular momentum quantum number L is simply the l value of the electron in the $2p$ orbital, since the vector sum of the l_i of all other electrons is zero.

The total electronic angular momentum $\mathcal{J}$ is given by the sum of L and S, with the quantum number $\mathcal{J}$ ranging from $|L - S|$ to $L + S$. Parity, denoted by p, is a property that describes the symmetry of the wave function of the electron configuration under spatial inversion. If the sum of the azimuthal quantum numbers, l_i, of all electrons is even, the parity is even and denoted by p. If the sum is odd, the parity is odd and denoted by o. This concept is important for determining selection rules for transitions between energy levels, as certain transitions are allowed or forbidden, based on the parity of the initial and final states. Gathering all quantum numbers describing a level of a multi-electron atom, the level term is expressed as ${}^{2S+1}L^p_{\mathcal{J}}$. For ionized carbon, due to spin-orbit coupling, this ${}^2P^{\rm o}$ term splits into two fine structure levels with total angular momentum $\mathcal{J} = 3/2$ and $\mathcal{J} = 1/2$. The corresponding terms are ${}^2P^{\rm o}_{3/2}$ and ${}^2P^{\rm o}_{1/2}$. The energy difference between these two levels is approximately 91.2 meV, which corresponds to the 157.74 μm (1900.537 GHz, calculated by laser magnetic resonance by Cooksy et al. 1986) fine structure line.

The fine-structure [CII]158μm transition between ${}^2P^{\rm o}_{3/2}$ and ${}^2P^{\rm o}_{1/2}$ does not involve a change in orbital angular momentum ($\Delta L = 0$) and parity, breaking two of the key selection rules for electric dipole transitions; hence it is a forbidden transition marked by brackets. Forbidden transitions still happen, e.g. as much slower magnetic dipole transitions.

The energy difference of their fine structure splitting is on par with the thermal energy, kT, of the ISM near massive, star forming regions. Consequently, collisional excitation of the ${}^2\mathrm{P}^{\rm o}_{3/2}$ level of CII by electrons, atomic and molecular hydrogen, or helium, followed by radiative decay, and emission of far-infrared photons that easily escape, carrying away the thermal energy of the gas. In the dense molecular interstellar gas of star forming regions, the submillimeter fine structure lines of ionized carbon and neutral oxygen are important cooling channels and are among the brightest emission lines in the far-infrared to millimeter spectral range (i.e., Hollenbach & Tielens 1999).

The [CII]158μm emission line (hereafter short [CII]) contributes 0.1 to 1% to the total far-infrared (FIR) luminosity of star-forming galaxies (Stacey et al. 1991). This line can in fact be used as a measure of gas heating due to massive, young stars, and thereby also serves as a proxy for the massive star formation rate on galactic scales (i.e., Leech et al. 1999).

De Looze et al. (2014b) show a correlation between the [CII] luminosity, $L_{\rm [CII]}$, of local universe galaxies and their star formation rate (SFR), across various galaxy types and gas metallicities. More recently, the ALPINE (Schaerer et al. 2020b) survey examined a sample of 118 main-sequence galaxies at redshifts $4 < z < 6$, establishing a $L_{\rm [CII]}$-to-SFR relationship similar to that found by De Looze et al. (2014b), making [CII]158 a robust SFR proxy up to $z \approx 6$

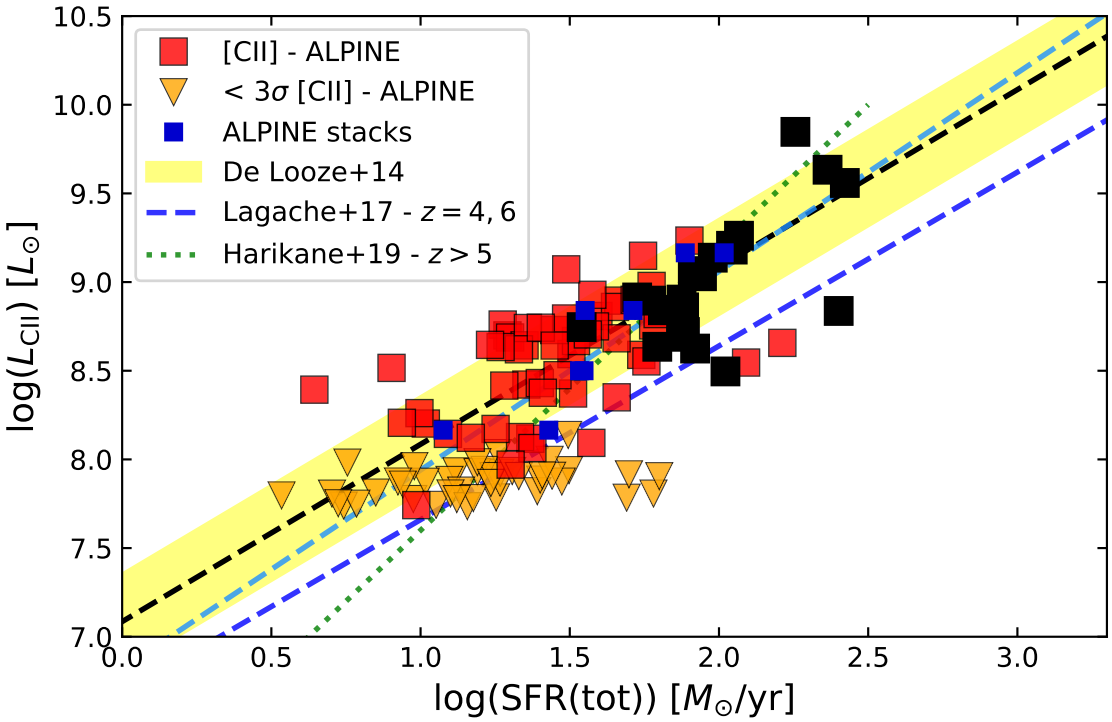

Figure 1.6: [CII] luminosity as a function of the UV+IR-derived SFR for $z \approx 4.5$ ALPINE (Schaerer et al. 2020a) sources. This plot illustrates that the SFR-$L_{[CII]}$ relation in the high-redshift universe as observed by the ALPINE survey closely aligns with local universe observations by De Looze et al. (2014a). Black squares represent [CII] detections in galaxies with continuum detection, red squares indicate SFR(UV) for non-continuum-detected sources, and orange triangles show 3σ upper limits. Blue circles depict results from stacks of ALPINE sources across four $L_{[CII]}$ bins and two redshift bins, adapted from Béthermin et al. (2020). The comparison includes a green dotted line showing the fitted relation for $z \approx 5-9$ galaxies by Harikane et al. (2020), and blue dashed lines represent model fits by Lagache et al. (2018) across the observed redshift range. Image from Schaerer et al. (2020a).

(Béthermin et al. 2020). Based on these observations, [CII]158μm LIM is a promising approach to trace early star formation.

1.3.5 CO line emission from galaxies

While most of the molecular gas in the Universe is comprised of molecular hydrogen, focusing on carbon monoxide, CO, the second most abundant molecule, for astronomical observations might seem counter-intuitive. However, Hydrogen molecules are symmetric and therefore have no electric dipole moment, and therefore no electric dipole emission is possible. Furthermore, the lowest excited rotational states have energy differences that correspond to temperatures much higher than the average kinetic temperature of the molecular gas or a few 10 K. Although CO is less abundant by a factor 10^4, its ability to emit dipole emission from low-energy rotational state transitions makes CO a bright and readily observable diagnostic of the molecular ISM, and a

strong coolant of the gas.

The energy levels for rotational transitions in a diatomic molecule are given by the quantum mechanical relation for the rotational kinetic energy (i.e., McQuarrie 1973),

$$E_{\rm rot} = \frac{\hbar^2}{2I} J(J+1),\ J = 0, 1, 2, ..., \tag{1.1}$$

where $\hbar$ is the reduced Planck constant, I is the moment of inertia of the molecule, J is the rotational quantum number of the diatomic molecule (not to be confused with $\mathcal{J}$ the spin-orbit coupling quantum number of multi-electron atoms mentioned in Sect. 1.3.4). For a transition, $\Delta J = \pm 1$, adhering to the conservation of angular momentum and the fact that the angular momentum of a photon is $\hbar$. The energy of a photon from a transition between to adjacent levels is

$$\Delta E_{\rm rot} = [J(J+1) - (J-1)J]\frac{\hbar^2}{2I} = \frac{\hbar^2 J}{I}, \tag{1.2}$$

and with $\Delta E_{\rm rot} = h\nu$, this give the frequency of the emission photon as

$$\nu = \frac{\hbar J}{2\pi I}. \tag{1.3}$$

This energy spectrum is described as a "ladder" with each "rung" corresponding to a transition frequency that is a harmonic of the base frequency. This results in a series of observable rotational transition lines, with CO(1-0) occurring at a rest frequency of 115.27 GHz and subsequent transitions following Eq. 1.3 and occurring at integer multiples of this base frequency.

The way the rotational levels of CO are populated, and thus the intensity of the emission or absorption lines, depends on the temperature of the gas. The minimum temperature required for significant excitation of the $J- > J-1$ transition can be calculated by equating the rotational energy of the upper level with the thermal energy of the gas $kT_{\rm min} \approx E_{\rm rot}$ where k is the Boltzmann constant. Following Condon & Ransom (2016), in combination with Eq. 1.1 we get

$$T_{\rm min} \approx \frac{\hbar^2}{2Ik} J(J+1),\ J = 0, 1, 2, ... \tag{1.4}$$

From this relation, it becomes clear that a cold environment primarily favors the population of lower rotational levels. For instance, the minimum temperature required for significant excitation of the $J = 1$ level is $T_{\rm min} \approx 5.6\,$K. As the environment becomes warmer, higher rotational levels are increasingly populated. For example, the $J = 4$ level requires a minimum temperature of $T_{\rm min} \approx 55.6\,$K, indicating that in warm environments, a greater contribution from higher J levels can be expected.

Adding to the complexity, the above equation represents only one of the many ISM phases a galaxy contains, making the modeling of the integrated CO luminosities very challenging. Despite these differences, on these galactic scales all the CO lines map the molecular gas, which is the fuel of star formation. In this study (Chapter 3), we make use of the correlations between the SFRs and CO (1-0) luminosities of galaxies, while also considering the impact the ISM conditions have on the intensity of the different CO rotational transitions of each galaxy. To achieve this, we use

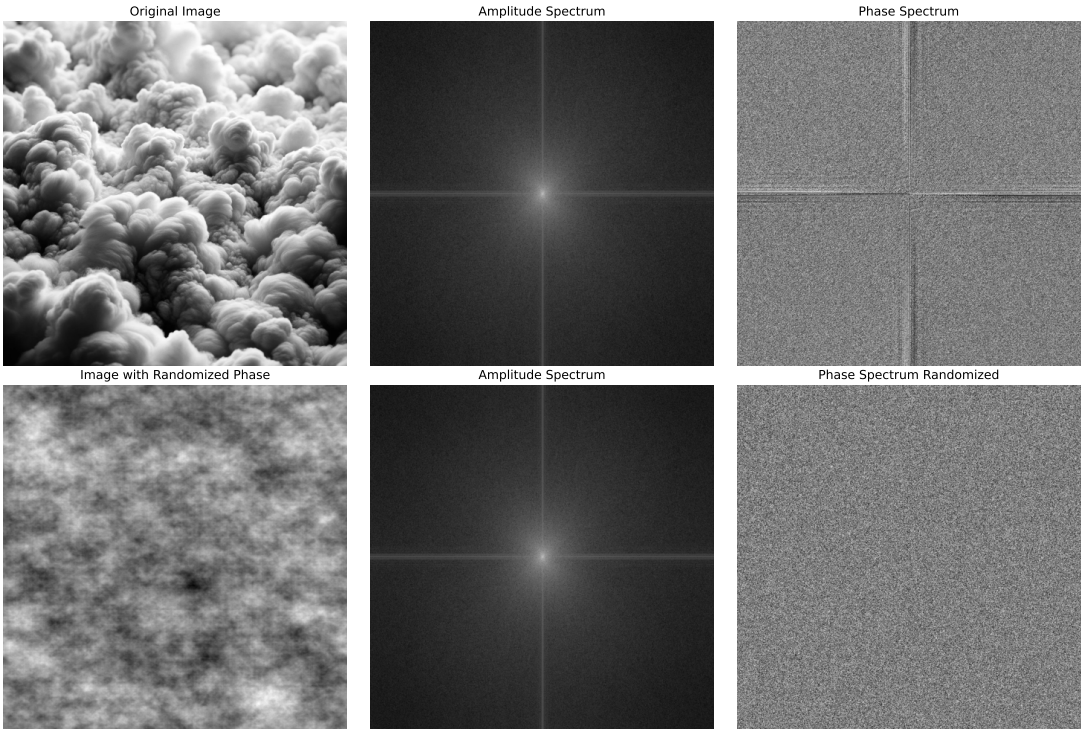

Figure 1.7: The power spectrum only captures the Gaussian components of an image. The top row displays the original image of clouds (left, image was created with the assistance of DALL·E 2, OpenAI 2024), its amplitude spectrum (middle), and its phase spectrum (right). The bottom row shows the image after randomizing its phase (left), the unchanged amplitude spectrum (middle), and the randomized phase spectrum (right). The panels on the left depict the spatial structure of the images, while the panels on the right present their Fourier transform components. In the amplitude and phase spectra, the x and y axes correspond to spatial frequencies, with brightness indicating the amplitude of these frequencies—brighter areas represent higher amplitudes or stronger frequency components. Notably, the two images share identical amplitude spectra. The amplitude spectrum, traced by the power spectrum, describes the distribution of frequency magnitudes but does not capture phase information. Without information about the phase spectrum (assuming it is random), only the Gaussian components of the original image can be traced, as evidenced by the smooth appearance of the image with randomized phase (bottom left). This transformation results in the loss of sharp edges and textures, underscoring the crucial role of the phase spectrum in preserving the non-Gaussian features and detailed structures of the original image.

as templates observations of the CO flux as a function of rotational quantum number J from the Milky Way and a stereotypical starburst galaxy, NGC253. By linearly combining these templates, we approximate the CO line luminosities for galaxies whose star formation rates fall between these two distinct extremes.

1.3.6 Fourier series and power spectrum

Our goal is to analyze the information contained in the fluctuations of the CIB induced by submillimeter lines. For this we utilize the mathematical framework of Fourier analysis. Fourier series allow us to deconstruct fluctuations into periodic waves represented by trigonometric functions. Following Weisstein (2024a) a periodic function $f(t)$ with period T can be represented as a sum of sine and cosine functions,

$$f(t) = a_0 + \sum_{n=1}^{\infty} \left[a_n \cos\left(2\pi n \frac{t}{T}\right) + b_n \sin\left(2\pi n \frac{t}{T}\right) \right], \tag{1.5}$$

where the coefficients a_0, a_n, and b_n are given by

$$a_0 = \frac{1}{T} \int_{-\frac{T}{2}}^{\frac{T}{2}} f(t)\, dt, \tag{1.6}$$

$$a_n = \frac{2}{T} \int_{-\frac{T}{2}}^{\frac{T}{2}} f(t) \cos\left(2\pi n \frac{t}{T}\right)\, dt, \tag{1.7}$$

$$b_n = \frac{2}{T} \int_{-\frac{T}{2}}^{\frac{T}{2}} f(t) \sin\left(2\pi n \frac{t}{T}\right)\, dt. \tag{1.8}$$

Using Euler's formula, we can express sines and cosines also as exponential functions. This allows us to rewrite the Fourier series as

$$f(t) = a_0 + \sum_{n=1}^{\infty} \left[\left(\frac{a_n - ib_n}{2} \right) e^{2\pi i n t/T} + \left(\frac{a_n + ib_n}{2} \right) e^{-2\pi i n t/T} \right]. \tag{1.9}$$

Defining $c_n = (a_n - ib_n)/2$ for $n > 0$, $c_{-n} = (a_n + ib_n)/2$ for $n < 0$, and $c_0 = a_0$, this simplifies to

$$f(t) = \sum_{n=-\infty}^{\infty} c_n e^{2\pi i n t/T}, \tag{1.10}$$

where c_n can be computed through the integral

$$c_n = \frac{1}{T} \int_{-\frac{T}{2}}^{\frac{T}{2}} f(t) e^{-2\pi i n t/T}\, dt. \tag{1.11}$$

Following Weisstein (2024b) we transition from periodic to aperiodic signals by allowing T to approach infinity. In this limit, the discrete frequencies $2\pi\ n/T$ become a continuous variable, ω, and the sum over n becomes an integral over ω. This leads to the continuous Fourier Transform (FT, $F(\omega)$) and its inverse ($f(t)$):

$$F(\omega) = \int_{-\infty}^{\infty} f(t) e^{-i\omega t}\, dt, \tag{1.12}$$

$$f(t) = \frac{1}{2\pi} \int_{-\infty}^{\infty} F(\omega) e^{i\omega t} \, d\omega. \tag{1.13}$$

The power spectrum is a concept that emerges naturally from the Fourier transform, representing the distribution of power of a function across different frequencies. For a given signal $f(t)$, its power spectrum $P(\omega)$ is defined in terms of its Fourier transform $F(\omega)$ as

$$P(\omega) = |F(\omega)|^2, \tag{1.14}$$

where $|F(\omega)|$ is the magnitude of the Fourier transform. This metric is highly effective at revealing underlying patterns and identifying dominant frequency components within the signal.

However, the power spectrum has a serious limitation: it lacks the information about the spatial arrangement of these frequencies that is encoded in the phase spectrum. Ignoring the phase information and assuming that the phase of each frequency component is random leads to a description of the image as an ensemble of Gaussian functions, due to the principles outlined by the central limit theorem, which states that the sum of a large number of independent random variables will tend towards a Gaussian distribution.

This can be seen in Fig. 1.7, which shows a fictitious image of clouds and the same image after the Fourier phase has been randomised. The scales of the structures and voids are reproduced, but without any texture or sharp detail. The original phase spectrum is clearly different from the randomised case, with clear correlations in the large scales, manifesting the presence of non-Gaussian features. The phase spectrum dictates how the spatial frequencies are aligned to reproduce features such as sharp edges and texture. In the absence of this alignment (i.e. with random phase), the unique structural features of the image blur into a homogeneity that resembles Gaussian noise. This limitation is the reason why, in the project presented in Chapter 3, we suggest that assessing the extent of CO contamination in a [CII] LIM tomography scan solely by measuring its power spectrum is challenging.

There are indeed other statistics, such as the voxel intensity distribution and the three-point correlation function, that capture this phase-space correlation. However, when analysing the LIM tomography scans in this project, we focus on the power spectrum because it is a simple statistic that is less sensitive to observational noise, sample variance and foreground contamination. Although it does not follow the non-Gaussianities, it is still related to the line luminosity function of the galaxy population. One of the directions we propose for the future (section 4.2) is the addition of metrics that are sensitive to the phase information and thus to the non-Gaussianities.

1.3.7 Power spectra of submillimeter LIM tomography scans

In this work, we focus on the LIM of submillimeter atomic/ionic and molecular lines emitted from the dense environments of galaxies. The most important metric for the emission from a galaxy distribution is the luminosity function, which represents the number density of galaxies per unit volume per logarithmic interval of luminosity. In this section, we will investigate how the power spectrum of LIM tomography scans is connected to the [CII] line luminosity function of the underlying galaxy population.

We will make use several comoving distance measures,typically expressed in cMpc, which factor out the expansion of the universe. Specifically, we will use the comoving angular distance,

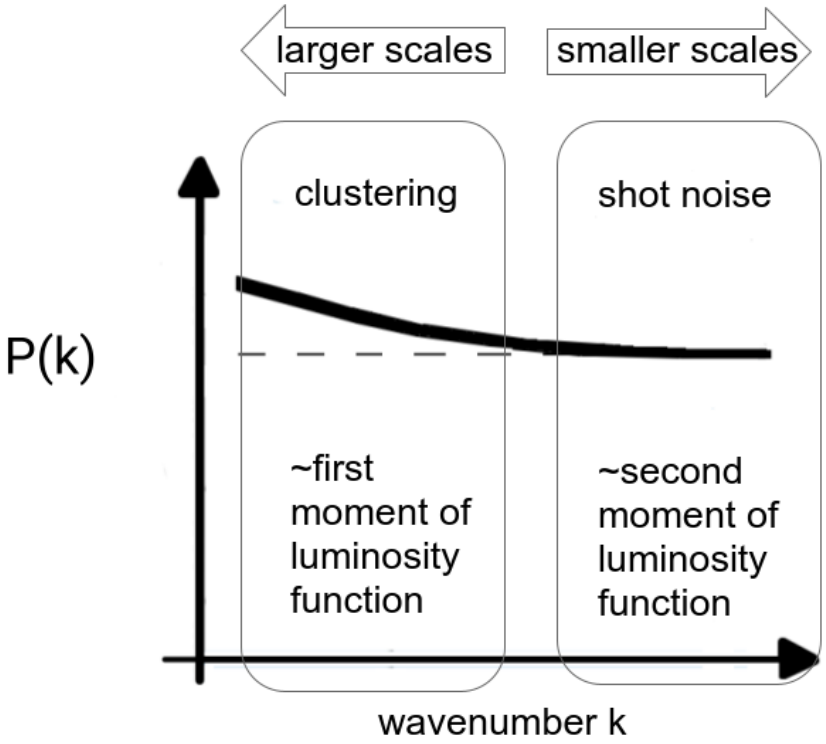

Figure 1.8: Power spectrum, $P(k)$, as a function of the wavenumber, k, illustrating the contributions from clustering and shot noise on different scales. On larger scales (left side of the figure), the power spectrum is dominated by the clustering signal, which is related to the first moment of the luminosity function. On smaller scales (right side of the figure), shot noise becomes significant, corresponding to the second moment of the luminosity function. The dashed line represents the shot noise component of the power spectrum. The arrows at the top indicate the direction towards larger and smaller scales.

$D_{\rm A}$, defined as the ratio of physical size to the angular size as viewed from Earth.

We will also use the comoving luminosity distance, $D_{\rm L}$, defined by the relationship between bolometric flux, S, which is the total energy per unit area per unit time received from the source across all wavelengths, and bolometric luminosity, L, which represents the total energy emitted per unit time by the source across all wavelengths. The relationship is given by,

$$D_{\rm L} = \left(\frac{L}{4\pi S}\right)^{1/2}. \tag{1.15}$$

The comoving radial distance, $\chi(z)$, to an object at redshift z is given by

$$\chi(z) = \int_0^z \frac{c\,dz'}{H(z')}, \tag{1.16}$$

where $H(z)$ is the Hubble parameter that describes the rate of expansion of the universe as a function of redshift.

In this section we will examine the power spectrum of a redshift slice of a LIM survey defined by the observed frequency, $\lambda_{\rm rest}(1+z)^2$, where $\lambda_{\rm rest}$ is the rest-frame wavelength of the targeted line. To account for the line-of-sight scale in a LIM survey, we will use the derivative of the comoving radial distance with respect to the observed frequency. This leads to the line-of-sight distance scaling factor, given by

$$y_{\rm [CII]} = \frac{\lambda_{\rm rest}(1+z)^2}{H(z)}, \tag{1.17}$$

The units of $y_{\rm [CII]}$ are typically expressed as [cMpc/Hz], which represent the comoving distance per unit of observed frequency. This factor is essential for converting frequency intervals into comoving distances along the line of sight in intensity mapping surveys.

Here we focus on the 3D power spectrum spherically averaged in Fourier space, represented as $P(k)$, a key metric for measuring the presence of cosmic structures. The power spectrum consists of two main components (Fig. 1.8): shot noise, $P_{\rm shot}$, which accounts for the discrete and stochastic nature of sources, and the clustering signal component, $P^{\rm clust}(k)$, which reflects that the spatial distribution of galaxies follows the underlying DM large-scale structure. The power spectrum for a specific line, such as the [CII] line, is expressed as

$$P_{\rm [CII]}(k) = P^{\rm shot}_{\rm [CII]} + P^{\rm clust}_{\rm [CII]}(k), \tag{1.18}$$

In the case of a population of galaxies within a redshift slice (with a given $D_{\rm L}$ and $D_{\rm A}$), the scale-independent $P^{\rm shot}_{\rm [CII]}$ can be expressed as (following Uzgil et al. 2014)

$$P^{\rm shot}_{\rm [CII]} = \int \frac{dn}{d\log L_{\rm [CII]}} \left(\frac{L_{\rm [CII]}}{4\pi D_L^2} y_{\rm [CII]} D_A^2\right)^2 d\log L_{\rm [CII]}\ . \tag{1.19}$$

Defining the luminosity function ($dn/d\log L_{\rm [CII]}$) as the number density of galaxies per unit volume per logarithmic interval of [CII] luminosity, eq. 1.19 shows that shot noise is related to the second moment of the luminosity function and is therefore dominated by the few luminous sources at the bright end of the luminosity function. Note that the shot noise component is scale-independent because it arises from random, uncorrelated fluctuations, rather than spatial correlations between sources, which are scale-dependent. The clustering signal in the power spectrum, can be expressed as

$$\begin{aligned} P^{\rm clust}_{\rm [CII]}(k) &= \bar{I}^2_{\rm [CII]} \bar{b}^2_{\rm [CII]} P_{\delta\delta}(k) \\ &= \left(\int \frac{dn}{d\log L_{\rm [CII]}} \frac{L_{\rm [CII]}}{4\pi D_L^2} y_{\rm [CII]} D_A^2 d\log L_{\rm [CII]}\right)^2 \bar{b}^2_{\rm [CII]} P_{\delta\delta}(k), \end{aligned} \tag{1.20}$$

where $\bar{I}_{\rm [CII]}$ is the mean intensity of the line, $P_{\delta\delta}$ is the DM power spectrum, and $\bar{b}_{\rm [CII]}$ is the bias relating [CII] line emission to the underlying DM distribution. The DM power spectrum, $P_{\delta\delta}(k)$, responsible for the scale-dependent nature of the clustering signal component, peaks at a scale well constrained by observational cosmology, specifically $k_{\rm eq} = 0.01034 \pm 0.00006\,{\rm Mpc}^{-1}$, set

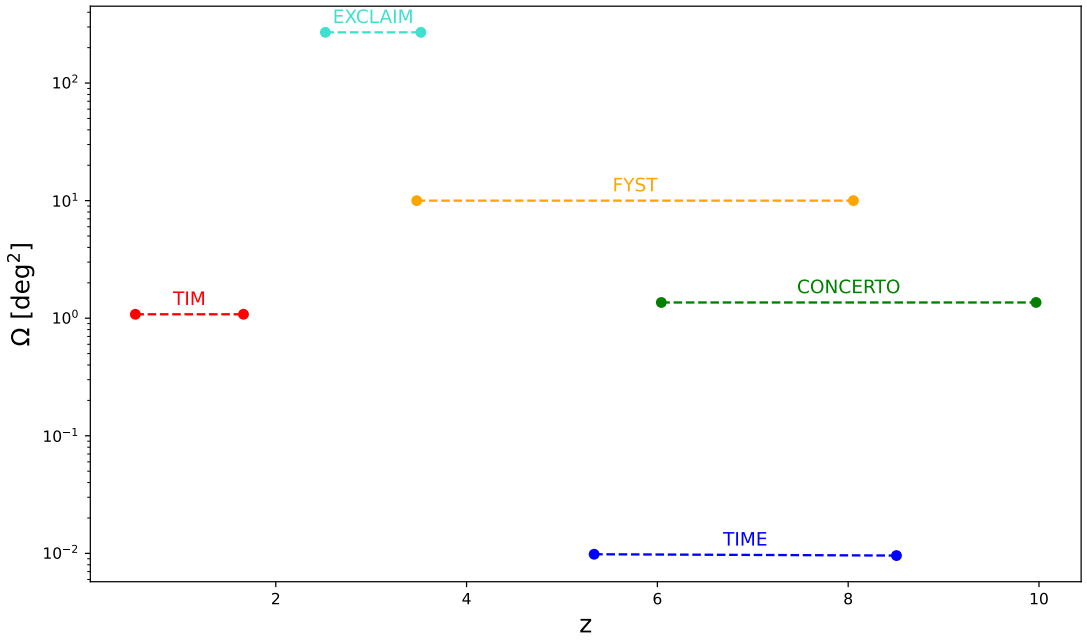

Figure 1.9: Redshift range and total sky coverage (summing different patches when required) probed by each upcoming line intensity mapping experiment targeting [CII]. The experiments are represented by lines of different colors, with the name of each experiment annotated below its respective line. The data was taken from Bernal & Kovetz (2022)

by the Hubble scale at the matter-radiation equality, which occurs at $z_{\rm eq} = 3387 \pm 21$ (Planck Collaboration et al. 2020). From Equation 1.20, it is clear that the clustering signal is related to the first moment of the luminosity function, indicating that it is sensitive to the entire galaxy population. Measuring the [CII] power spectrum at both shot noise and clustering signal dominated scales allows for better constraints on the [CII] line models, given the different relationships of these components with the [CII] luminosity function.

1.4 Experimental Landscape

1.4.1 FYST LIM survey

The Fred Young Submillimeter Telescope (FYST) is equipped with two primary scientific instruments for its regular survey operations. Prime-Cam (Vavagiakis et al. 2018) is central to our scientific objectives and detailed here. It features imaging camera modules as well as broadband, low-resolving-power direct-detection spectrometer modules. The second instrument is the CCAT Heterodyne Array Instrument (CHAI Graf et al. 2019), designed for high-efficiency, velocity-resolved sub-millimeter mapping of key diagnostic emission lines from the Milky Way and nearby galaxies. After an initial one-year commissioning period, the relative allocation of observing time will approximately three-quarters for Prime-Cam and one-quarter for CHAI.

Prime-Cam (Fig. 1.12) utilizes the central 4.9 degrees of the 8 degrees diameter field of view of FYST. As a 1.8 m diameter cryostat, Prime-Cam hosts seven optically and electronically independent instrument modules arranged hexagonally around a central module, each capable of covering an up to 1.3° diameter field of view. Five of these modules are broadband and polarization-sensitive, designed for observations at frequencies around 220, 280, 350, 410, and 850 GHz. Of particular interest to our project are the two imaging spectrometer modules dedicated to LIM across the 205 to 440 GHz spectral range. These EoR-Spec (Cothard et al. 2020) modules use a cryogenic imaging Fabry–Pérot interferometer (FPI, Perot & Fabry 1899; Zou et al. 2022) for spectral scanning. These modules are specifically optimized for detecting the 158 μ m [CII] line emission from redshifts $z = 3.5$ to 8.05. The FPI features two parallel, highly reflective silicon-substrate-based (SSB) mirrors located at the Lyot stop. This configuration enables specific wavelengths of radiation to constructively interfere after multiple reflections, provided the path difference between these reflections is an integer multiple of the wavelength. This interference occurs at specific angles of incidence for given wavelengths, producing bright fringes of transmitted and reflected radiation. The FPI steps through frequencies between 210 and 425 GHz and illuminates one broadband, non-polarization sensitive detector array centered around 370 GHz (0.8 mm) and two arrays centered around 260 GHz (1.1 mm).

The spectral range entering the FPI is finely controlled: the short wavelength cutoff for each array is determined by low-pass filters placed directly in front of the arrays, while the longer wavelength cutoff is defined by the feedhorn design of each pixel on the detector array. This setup results in concentric fringes, allowing the measurement of intensity not just at a single wavelength, but over a range of wavelengths. The relationship between wavelength and angle of incidence yields multiple solutions, forming first, second, and third-order fringes. The optical design of EoR-Spec projects the second-order fringe on the two 205-300 GHz arrays and the third-order fringe on the 300-430 GHz array, each achieving a spectral resolving power $R = \lambda/\Delta\lambda = 100$. The configuration of two low-frequency arrays and one high-frequency array is deliberate, enhancing the detection of the more elusive low-frequency (high-redshift) LIM signal compared to the more easily detectable high-frequency (low-redshift) signal.

The EoR-Spec bands employ arrays with similar design, each featuring for each pixel a feed-horn coupled to a waveguide, which terminates in a Kinetic Inductance Detector (Day et al. 2003; Duell et al. 2020, KID,). In KIDs, a superconductor is integrated into an electrical circuit tuned to resonate at a specific frequency. When electromagnetic radiation impacts the superconductor, it alters the resonant frequency of the circuit. The measured frequency changes relate to the change in incident intensity, rendering KIDs exceptionally sensitive light detectors.

The primary focus of EoR-spec will be the FYST LIM survey, also known as the Deep Spectroscopic Survey (DSS, CCAT-Prime Collaboration et al. 2023), a 4000-hour imaging survey of two field in the sky. Each field will be scanned for 2000 hours, covering frequencies in the 205 to 430 GHz range to target the [CII] line over the redshift range $3.4 < z < 8.3$. The DSS will focus on two ≈ 5 deg^2 fields (Fig. 1.10): the Extended COSMOS field (E-COSMOS, Aihara et al. 2018) and the Extended Chandra Deep Field South (E-CDFS, Lehmer et al. 2005). These fields were selected for their extensive multi-wavelength ancillary data, enabling cross-correlation with optical, infrared, and radio observations. By observing deeply in these regions, the DSS aims to map large-scale structures at high redshifts and explore the reionization history of the universe.

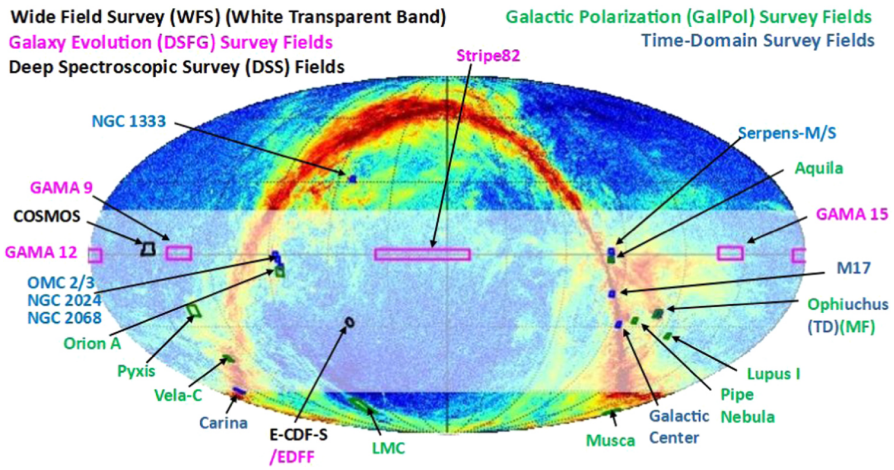

Figure 1.10: Map of FYST line intensity mapping the EoR survey fields, highlighted in black in equatorial coordinates overlaying the Planck dust polarization map (Planck Collaboration et al. 2013). Additional survey fields related to galaxy evolution, galactic polarization, and time-domain sciences are indicated in magenta, green, and blue respectively. Image from CCAT-Prime Collaboration et al. (2023).

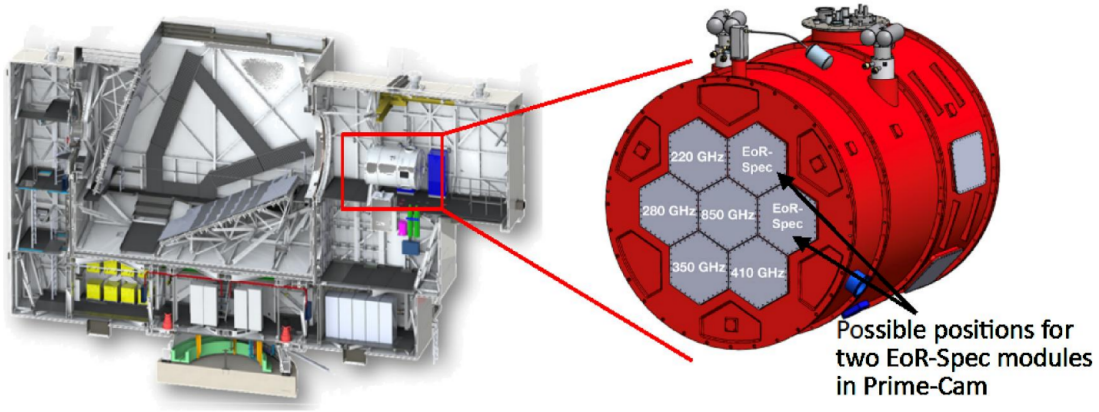

Figure 1.11: Cross-section of the FYST CAD Model (left) showing the instrument bay where Prime-Cam will be installed, and the design layout of the Prime-Cam instrument (right), illustrating the arrangement of seven instrument module entrance windows. These include five polarization-sensitive modules operating at nominal center frequencies from 220 to 850 GHz, and two spectrometer modules (EoR-Spec, Vavagiakis et al. 2018), which will conduct the [CII] LIM survey forecasted in this work. Image from Nikola et al. (2023).

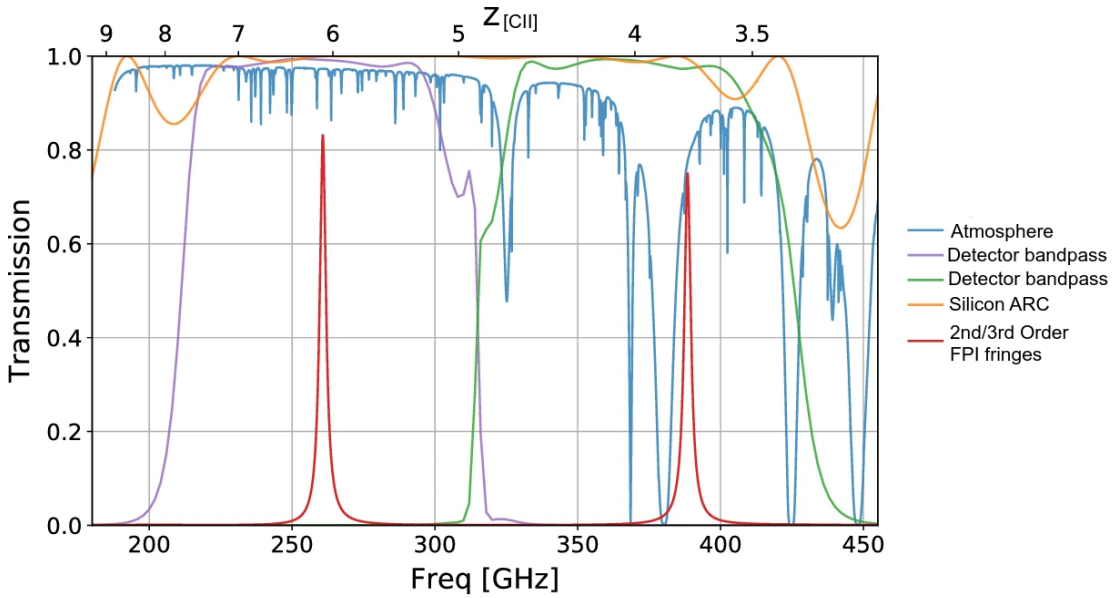

Figure 1.12: Atmospheric transmission and an example of FPI fringes for the detection of the redshifted [CII] line using the EoR-Spec instrument on Prime-Cam, part of FYST. The plot shows the transmission efficiency of the instrument over the frequency range 205 to 430 GHz, relevant for detecting [CII] emission from galaxies during the EoR. The secondary axis corresponds to the redshift ($z_{[\mathrm{CII}]}$) of the galaxies emitting the [CII] line, demonstrating the redshift range that EoR-Spec can observe. The blue curve represents the atmospheric transmission, highlighting regions of low and high transparency due to absorption by water vapor and other molecules in the atmosphere of the Earth. The purple and green curves represent the bandpasses of the two detector arrays: 205-300 GHz and 300-430 GHz, which capture the second and third-order FPI fringes, respectively. These fringes are produced by the FPI which uses two highly reflective silicon substrate mirrors to create constructive interference at specific wavelengths, resulting in bright transmission fringes, illustrated in red. The second-order FPI, detected by the 205-300 GHz array, and the third-order fringe, detected by the 300-430 GHz array, are both optimized to measure radiation intensity over a broad frequency range. This optimization enables EoR-Spec to detect faint [CII] emission from galaxies at high redshifts ($z_{[\mathrm{CII}]} \approx 3.4 - 8.3$). The orange curve shows the effect of the Silicon Anti-Reflection Coating (ARC), which reduces reflection losses at the detector surface, enhancing overall transmission across the operational frequency range of the instrument. Image adapted from Cothard et al. (2020).

1.4.2 Other upcoming surveys

In the rapidly evolving field of LIM techniques, a wide range of experiments focusing on the [CII] line are poised to significantly advance our understanding of early galaxies. These experiments employ spectro-imagers mounted on high-altitude telescopes or on balloons undertaking dedicated flights.

On the ground-based telescope front, we have the CarbON CII Line in post-rEionisation and ReionisaTiOn epoch (CONCERTO, CONCERTO Collaboration et al. 2020) project, which utilizes the Atacama Pathfinder Experiment (APEX) telescope in Chile, and the Tomographic Ionized-carbon Mapping Experiment (TIME, Crites et al. 2014; Sun et al. 2021) in Arizona, USA. Both projects aim to map the [CII] emissions in the early universe, targeting redshift ranges of 4.5 to 8.5. CONCERTO employs a Martin-Puplett interferometer (Martin & Puplett 1970) coupled with a focal plane array of KID detectors, while TIME uses a millimeter-wavelength grating spectrometer coupled with Transition Edge Sensor (TES Irwin et al. 1996) bolometers.

In the balloon-borne category, we have the Tomographic Ionized-carbon Mapping Experiment (TIM, Vieira et al. 2020) and Experiment for Cryogenic Large-Aperture Intensity Mapping EXCLAIM (EXCLAIM, Switzer et al. 2021) projects. TIM, expected to fly over Antarctica, will target the [CII] line at redshifts of $0.5 < z < 1.5$, while EXCLAIM, set to fly over North America, will explore the $2.5 < z < 3.5$ redshift range. The spectro-imager of TIM will be an integral-field spectrometer operating from 240 to 420 microns, coupled to 3600 KIDs with a 2-meter low-emissivity carbon fiber telescope. EXCLAIM will utilize an array of six superconducting integrated grating-analog spectrometers, each coupled to 355 KID detectors.

The field is expected to see many more experiments joining the [CII] LIM research, especially given the recent advancements in on-chip spectrometer technology. An on-chip spectrometer is a highly miniaturized device integrated onto a semiconductor chip, enabling compact and efficient spectral analysis of astronomical objects. This technology marks a significant leap in astronomical instrumentation, offering a smaller, lighter, and potentially less costly alternative to traditional spectrometers, which are typically large, complex, and require precise optical alignment. On-chip spectrometers leverage microfabrication techniques to integrate all necessary optical or electromagnetic components onto a single, small chip, significantly reducing size and weight while maintaining or enhancing performance capabilities.

Proposed instruments like the Large Submillimeter Telescope (LST Kawabe 2018) and the Atacama Large Aperture Submillimeter Telescope (AtLAST van Kampen et al. 2024) are ideally equipped to leverage the strengths of both the survey catalog technique and the LIM technique. For instance, Kohno et al. (2020) propose a three-band (200, 255, and 350 GHz) imaging spectrograph equipped with approximately 1.5 million detectors. This setup utilizes integrated superconducting spectrometer (ISS) technology alongside a large-format imaging array to map wide fields at medium resolution (R = 2,000). This approach allows for the use of the same dataset to both generate detailed galaxy catalogs and perform statistical analyses as a line intensity map. Such a dual methodology will significantly enhance the scientific yield, merging the benefits of both techniques to explore the Universe with an unprecedented level of detail and efficiency.

Still, all experiments observing from within the atmosphere, including those conducted via balloon, encounter challenges in mapping large scales dominated by atmospheric foregrounds. To address this, launching a dedicated space observatory for LIM is proposed. Silva et al. (2021)

outline a space mission that includes a full sky survey and a deep patch survey covering 400 square degrees, operating across a frequency range of 100 - 2000 GHz, with a spectral resolution of R=300, and an angular resolution of 10 arcseconds at 300 GHz. The focal plane is expected to utilize 64 on-chip filter-bank spectrometers. This observatory would ideally be positioned around the L2 Sun-Earth Lagrange point to optimize observing conditions, minimizing interference and maximizing the quality of astronomical data.

CHAPTER 2

Line intensity mapping predictions using the Illustris TNG hydrodynamical simulation

This chapter is a summary of the article published in Astronomy and Astrophysics (A&A) as:

C. Karoumpis, B. Magnelli, E.Romano-Díaz, M. Haslbauer, and F. Bertoldi. (2022), A&A 659, A12.

This publication presents work conducted by Karoumpis under the supervision of Magnelli and Bertoldi. The other co-authors contributed to the interpretation of the results and provided comments and revisions to the final manuscript. The refereed article can be found in Appendix A, while the open access version is found under the reference arXiv:2111.12847.

2.1 Context

In the formative period spanning 300 to 1000 million years after the Big Bang, the emergence of proto-galaxies and the change in the phase of the of the intergalactic medium from neutral to ionized mark a crucial epoch known as the Epoch of Reionization (EoR for a review see Zaroubi 2013). The influence of early galaxy formation on this reionization process is widely recognized. The ultra-violet (UV) light escaping from the early galaxies is believed to have been responsible for the ionization of the intergalactic medium. However, the precise dynamics of these interactions are not yet fully understood and specifically the kind of the galaxies that produced the majority of the ionizing UV emission (e.g., Robertson 2022). The prevailing theory is that numerous faint galaxies were the main source behind the energy budget of the reionization. Unfortunately this sources are too faint and distant to be detected by current observational facilities, including the state-of-the-art *James Webb Space Telescope* (JWST, Boylan-Kolchin et al. 2015). In response, line intensity mapping (LIM; e.g., Kovetz et al. 2019; Bernal & Kovetz 2022) has been developed as a promising observational technique. This method involves quantifying the cumulative emissions of spectral lines from entire galaxy populations. It captures these emissions across specified redshifts and sky coordinates, thereby tracing the contribution of both bright and dim galactic bodies.

2.2 Aims

This research aims to forecast observations of the three-dimensional intensity power spectrum (PS) of the [CII] 158 μm line across various redshifts, from approximately 3.5 to 8. These redshifts coincide with and follow the EoR. The predictions are specifically tailored to simulate forthcoming observations using the Prime-Cam spectro- imager, which is mounted on the Fred Young Submillimeter Telescope (FYST, CCAT-Prime Collaboration et al. 2023). The primary goal of this study are to assess the potential detectability of the [CII] PS. Additionally, the study seeks to understand the implications of such measurements on the models of star formation, early galaxy evolution as well as models of the reionization of the Universe.

2.3 Methods

Employing the advanced capabilities of the Illustris TNG300-1 ΛCDM simulation (TNG300; Pillepich et al. 2018b), our study produced simulated [CII] tomographic scans across four redshift intervals: $z = 3.7, 4.3, 5.8$, and 7.4. We estimated star formation rates (SFRs) within dark matter (DM) halos using two distinct methodologies. Firstly, directly from the intrinsic SFRs computed within the simulation. Secondly, through abundance matching the DM halo of the simulation with SFRs derived from the dust-corrected UV luminosity function of high-redshift galaxies. To establish a connection between [CII] luminosity ($L_{[\mathrm{CII}]}$) and SFR, we applied three scaling relations. One relations came from a semi-analytic galaxy formation model, another was derived from a hydrodynamical simulation of a high-redshift galaxy, and the third was based on empirical data from a recent high-redshift [CII] galaxy survey. By integrating the two approaches on the DM halo-galaxy SFR relation with the three SFR-to-$L_{[\mathrm{CII}]}$ relations, we calculated six alternative scenarios for the [CII] intensity power spectrum for each spectral band selected by FYST. This range of predictions enabled a detailed and robust assessment of the detectability of the [CII] PS, given the expected observational capabilities of FYST.

2.4 Results

The model-dependent predictions for the [CII] intensity power spectrum show significant variability, with differences exceeding a factor of 10. These differences depend on the selection of halo-to-galaxy SFR and the SFR-to-$L_{[\mathrm{CII}]}$ relations. Within a survey area of $4^o \times 4^o$ conducted by FYST, our projections forecast detections of the [CII] PS of the tomographies centered at $z = 3.7, 4.3$ and 5.8 and a tentative detection for the tomography centered at $z = 7.4$. The survey design supports measurements of the PS at diverse scales. It enables a detection both in sub-10 Mpc scales, where the shot noise predominates and at scales greater than 50 Mpc, where the clustering signal component become more significant. This fact positions the survey as a groundbreaking experiment in line intensity mapping, capable of imposing constraints on both the relationships between SFR and $L_{[\mathrm{CII}]}$ as well as between halos and galaxy SFRs.

2.5 Conclusions

The FYST LIM survey is poised to significantly advance our understanding of galaxy formation and the role of the interstellar medium during the Epoch of Reionization. By mapping the [CII] emission across a wide range of scales and redshifts, the survey aims to provide critical constraints on the relationships between DM halos, star formation, and interstellar medium cooling processes pivotal during the early epochs of the Universe.

CHAPTER 3

CO foreground masking based on an external catalog

This chapter is a summary of the article submitted for publication in Astronomy and Astrophysics (A&A) as:

C. Karoumpis, B. Magnelli, E. Romano-Díaz, K. Garcia, A. Dev, J. Clarke, T.-M. Wang, T. Bădescu, and F. Bertoldi.

This publication presents work conducted by Karoumpis under the supervision of Magnelli and Bertoldi. The other coauthors contributed to the interpretation of the results and provided comments and revisions to the final manuscript. The submitted article can be found in Appendix B.

3.1 Context

The Fred Young Submillimeter Telescope (FYST, CCAT-Prime Collaboration et al. 2023) Line Intensity Mapping (LIM; e.g., Kovetz et al. 2019; Bernal & Kovetz 2022) survey is strategically designed to trace the star formation taking place in the galaxies during and right after the epoch of reionization, by analyzing the power spectrum (PS) of the singly ionized carbon 158 μm fine-structure line, known as [CII]. The [CII] line is the brightest submillimeter line of the star forming galaxies (Stacey et al. 2018) and it is a tracer of their star formation rate (De Looze et al. 2014a), making it an invaluable tool for understanding the sources that powered the change in the phase of the intergalactic medium during the epoch of reionization.

3.2 Aims

The principal aim of this study is to methodically quantify and address the contamination of the post-EoR [CII] signal caused by the line foreground emissions. Specifically,the aim was to forecast the lines that pose a substantial challenge namely the carbon monoxide (CO) rotational line emissions, with upper quantum numbers ranging from 3 to 12 from galaxies at redshifts lower than that of the [CII] emitters. Moreover, this research evaluates the effectiveness of a masking technique that leverages an external catalog to exclude voxels predicted to host intense

CO emitters. By doing so, the study aims to pave the way for more accurate measurements of the [CII] power spectrum, thereby enhancing the reliability of our understanding of early star formation as well as the evolution of proto-galaxies.

3.3 Methods

This investigation employs the advanced IllustrisTNG300-1 simulation (TNG300; Pillepich et al. 2018b) to create mock CO intensity maps, which are derived from empirical relationships between the star formation rates (SFRs) and the CO luminosities of galaxies. These maps are then integrated with previously generated mock [CII] maps to perform a comprehensive assessment of the efficacy of the proposed masking technique. The technique utilizes an external catalog, characterized by properties akin to those expected from a forthcoming deep Euclid survey (Euclid Collaboration et al. 2022), to identify and mask potential CO interlopers systematically. This approach is intended to minimize the CO signal contamination in the [CII] measurements, thereby isolating the targeted [CII] signal for analysis.

3.4 Results

Our preliminary analysis demonstrates that, before the implementation of our masking strategy, the forecasted LIM tomography is significantly compromised by CO foregrounds especially at the lower frequency bands of the FYST LIM spectro-imager. Specifically, in the 225 GHz band, where [CII] emissions are registered at redshifts ranging from 6.8 to 8.3, the [CII] PS is observed to be an order of magnitude lower than the CO interference. Notably, in the 280 GHz band (where [CII] is emitted at redshifts of 5.3 to 6.3) and the 350 GHz band (where [CII] is emitted at redshifts of 4.1 to 4.8), the level of the CO mean intensity is of the same order of magnitude with that of the [CII] line. Conversely, in the 410 GHz band (where [CII] emissions occur at redshifts of 3.4 to 3.9), the [CII] signal notably exceeds the level of CO contamination. The optimal depth of masking, which is quantified by the proportion of the survey volume that should be masked in order to effectively mitigate the CO interference on the [CII] PS, exhibits substantial variability across these bands. It is determined to be less than 10% at 350 and 410 GHz, approximately 40% at 280 GHz, and reaches up to 60% at 225 GHz. With the specified masking depths appropriately applied, we anticipate not only the successful detection of the [CII] PS at 410 GHz and 350 GHz but also a possible detection at 280 GHz. However, at 225 GHz, even extensive masking fails to sufficiently suppress the dominant CO signal, indicating that the deployment of alternative, potentially more sophisticated and model dependent decontamination strategy might be necessary to effectively extract and analyze the [CII] signal in this particularly challenging band.

3.5 Conclusions

Our models predict a dichotomy where, above 300 GHz ($z_{[\mathrm{CII}]} = 5.5$), the [CII] signal is expected to be dominant, and the required masking is minimal. Below this frequency, dealing with the CO foregrounds becomes more challenging since they are at the same level or higher than the

targeted signal. However, a detection at the end of the EoR ($z_{[\mathrm{CII}]} = 5.8$) remains very possible. Future research will need to adopt different model-dependent approaches to retrieve the signal in the lower frequency channels of FYST, which correspond to higher redshift galaxies.Our study lays the foundation for future LIM research into the high-redshift universe. Developing advanced decontamination techniques to extract the [CII] high-redshift signal, along with detailed modeling of astrophysical and atmospheric foregrounds for accurate forward modeling, are essential next steps.

CHAPTER 4

Summary and outlook

4.1 Summary

Both studies presented here are in preparation for the upcoming FYST LIM EoR survey. The first study produces a set of predictions for the target [CII] signal from (post)EoR galaxies, using two approaches to model the DM-galaxy SFR connection: a hydrodynamical simulation (TNG300) and an abundance matching technique that matches a DM halo catalog with high-redshift dust-corrected UV observations. Furthermore, the study considers three different SFR-to-$L_{[\mathrm{CII}]}$ relations to forecast intensities across a range of redshifts ($z = 3 - 8$). One is based on observations, another from a semi-analytic model, and the third derived from a zoom-in hydrodynamical simulation of a high-redshift galaxy. In all cases, the mean intensity is found to significantly decrease towards lower frequencies (higher [CII] emitter redshifts) due to increasing distance of the galaxies and the decline of the cosmic star formation rate density (SFRD). Notably, the predictions differ up to an order of magnitude between models. Further, the study delves into the spatial fluctuations of these [CII] intensities by calculating the three-dimensional spherically-averaged PS, which is the metric intended to be measured with the FYST spectro-imager.

The predicted [CII] intensity power spectrum varies by up to a factor of 30, influenced by the choice of halo-to-galaxy SFR and SFR-to-$L_{[\mathrm{CII}]}$ relations. The level of shot noise in the power spectrum (corresponding to small, Mpc-scale fluctuations) is predominantly affected by the chosen SFR-to-$L_{[\mathrm{CII}]}$ relation and to a lesser extent by the M_{h}-SFR relation. Meanwhile, the level of the clustering component of the power spectrum (corresponding to large, tenths of Mpc-scale fluctuations) primarily depends on the cosmic SFRD incorporated in the model and, to a smaller degree, on the selected SFR-to-$L_{[\mathrm{CII}]}$ relation. Furthermore, the anticipated signal-to-noise ratio (S/N) for the FYST [CII] LIM survey is also estimated, focusing on the various factors that influence the detection capabilities of the survey over four tomographic scans at different redshifts. The analysis combines three major sources of noise: instrumental white noise, sample variance within each Fourier wavenumber range (k-bin), and attenuation due to smoothing by the instrumental beam. The instrumental white noise is calculated based on the survey size, total observing time, and noise equivalent intensities of the spectro-imager. Sample variance refers to the statistical uncertainty due to the finite number of averaged Fourier modes that affects the accuracy of the intrinsic power spectrum estimate. Finally, the beam smoothing

attenuation is the loss of signal detail due to the finite resolution of the instrument, which smooths out variations over small spatial scales.

Each of these factors contributes differently across various scales, affecting the S/N ratio over k-space. We find that the S/N is highest at lower k values, where the clustering signal dominates, and decreases at higher k-values where the shot noise becomes significant and beam smoothing attenuates the signal severely. The detection of the [CII] power spectrum is therefore more feasible at larger scales (lower k) for all models and redshifts, with the challenge increasing at smaller scales (higher k) due to higher noise and resolution effects. The study quantifies in detail the trade-offs between resolution, coverage, and noise, providing a roadmap for optimizing survey parameters to achieve the best possible scientific outcomes. Based on these predictions, we explored the potential for [CII] power spectrum measurements in four selected FYST frequency bands, predicting a detection at 410, 350, and 280 GHz, and a tentative detection at 225 GHz. However, these predictions did not account for the challenge of foregrounds, which was the focus of the second paper.

The second study addressed the challenge of CO emission contamination when observing the [CII] line. By producing a range of predictions based on TNG300, it quantified the impact of CO emission, particularly from low-J transitions at lower redshifts, and tested a foreground masking technique using an external catalog. The study first examines the line intensities of [CII] and CO across the FYST frequency bands, demonstrating that the mean intensity of the CO lines does not vary as significantly with frequency as the mean intensity of [CII], due to the smaller differences in the luminosity distances and the SFRs of the galaxy populations emitting the low-J CO lines that dominated the CO emission. The findings indicate that [CII] becomes the dominant line at frequencies higher than 300 GHz. This preliminary analysis helps to inform a masking strategy aimed at minimizing CO contamination of the [CII] line intensity maps while preserving the [CII] signal. The effectiveness of the masking technique is rigorously evaluated by its impact on the power spectrum (PS) of the signals, focusing on minimizing the CO contribution without significantly distorting the [CII] signal. The study employs a three-step approach to evaluating the impact of masking, starting with its effects on the CO PS alone, then the [CII] PS alone, and finally the combined effects on the CO+[CII] PS. Various masking depths are tested to find the optimal balance where CO contamination is minimized.

Interestingly, the results show that while masking can significantly reduce CO interference, it also introduces a masking bias to the [CII] PS, especially at deeper masking levels. This fact should be accounted for when estimated the optimal masking depth. The study concludes that large portions of the survey volume must be masked to effectively remove CO contamination—approximately 60% at 225 GHz and 40% at 280 GHz. At higher frequencies, centered at 350 and 410 GHz, the required masking was substantially less, under 10%. The technique proved effective at 350 and 410 GHz, offering a strong likelihood of successful [CII] detection. Although it presented challenges at 280 GHz, there remains a serious possibility of success. However, the results indicated that this masking method is unlikely to be sufficient at 225 GHz, highlighting the need for alternative decontamination strategies at lower frequencies. Based on this result, the study emphases the importance of developing advanced decontamination techniques and further modeling of astrophysical foregrounds to improve the detectability of the [CII] power spectrum in future high-redshift LIM surveys.

Estimating the optimal masking depth for cleaning a real LIM tomography is fairly straightforward, but understanding the extent of decontamination achieved at that depth introduces greater complexity. This challenge arises from the fact that CO and [CII] emitters exhibit similar spatial frequency characteristics, complicating the task of distinguishing between them based solely on the distribution of the intensities of their Fourier modes. In our study we take an approach according to which we construct a weighted voxel histogram, where each voxel is weighted by the square of its intensity, and the histogram is adjusted using the PS measurement of the tomography masked at the optimal depth. Analyzing this histogram for signs of bimodality can indicate a successful shift from a CO-dominated to a [CII]-dominated state. However, this method is only effective for data with low instrumental white noise, approximately five times lower than expected for 2000 hours of observations.

The predictions in both papers were developed by post-processing the mock galaxy catalogs derived from the TNG300 simulation. We used the DM halo catalogs from TNG300 snapshot cubes to create a $4^o x 4^o$ observational cone catalog spanning from $z = 0$ to $z = 10$. Given the limited knowledge of line emission in the early universe, we employed various scaling relations to generate a spectrum of predictions for both the targeted [CII] and the CO foreground emissions, ranging from the most pessimistic to the most optimistic scenarios. Collectively, the results of these two studies illustrate how upcoming line intensity mapping surveys could significantly enhance our understanding of the early universe over the next decade, complementing high-resolution data from state-of-the-art telescopes like JWST and ALMA with statistically robust, unbiased wide-field measurements.

By measuring the [CII] PS in the frequencies and scales traced by FYST, we will be able to trace the evolution of the star formation rate in early galaxies. Measurements based on surveys of single-object observations of high-redshift galaxies are biased towards brighter sources and due to their pencil-shaped fields suffer from the problem of high sample variance. LIM on the other hand, enables wide-field, low-sample-variance surveys that capture the integrated emission from all galaxies, including the numerous faint ones believed to have powered the phase change in the IGM during the epoch of reionization. This approach will provide critical insights into this early and largely unexplored period of the Universe.

4.2 Outlook

Building on the foundations laid by this work, future research can expand in several directions: refining the modeling of line emission in the early universe, developing innovative foreground decontamination techniques, and combining submillimeter line models with LIM observations to extract valuable astrophysical parameters through forward modeling. Furthermore, the upcoming FYST LIM survey data will be crucial for testing our masking techniques and assessing the accuracy of our predictions of the [CII] power spectrum.

4.2.1 Improving models of submillimeter line emission from high-redshift galaxies

One limitation of our study was our reliance on a single realization of the TNG300 simulation box for creating mock observations. Consequently, due to sample variance, the actual survey

results may deviate from our simulations, even if all our assumptions are correct. A potential solution is to use actual galaxy catalogs from fields targeted by upcoming LIM surveys. This is particularly useful for foregrounds originating from redshifts where most galaxies have already been observed at other frequencies, unlike the high-redshift [CII] line. This approach would enable more accurate forecasting of the LIM survey foreground, specifically tailored to these fields, allowing us to refine and test decontamination methods based on these tailored forecasts.

Another approach involves employing machine learning algorithms that can generate a large number of realizations of a simulation cube, each aligned with the underlying parameters of simulations like TNG300. This efficiently reduces the sample variance in predictions of the [CII] signal from high redshifts, which have not been extensively observed at other frequencies.

Improvements can be made not only to the catalogs on which the models are applied, but also to the models themselves. Moving beyond simple scaling relations, one could post-process the gas particles in simulations, to better model thermal, radiative, and chemical processes for producing line luminosities. This process could then be expedited and applied to galaxy catalogs using machine learning algorithms.

4.2.2 Line de-blending techniques for CO foreground mitigation

The masking technique used here is reliable and straightforward. However, it is far from the most efficient: a single kiloparsec CO-bright galaxy results in the masking of a megaparsec voxel. There are more complex techniques that could be used that, instead of simply masking contaminated voxels, de-blend the contributions of different lines (Cheng et al. 2020). These techniques are based on templates of the CO SLEDs fitted to the tomography along the line of sight. Although these methods involve more assumptions than the masking techniques, they have the significant advantage of preserving the full survey volume.

4.2.3 Atmospheric foreground

Although CO foregrounds at lower frequencies (below 300 GHz) pose significant challenges for an Earth-based observatory like FYST, the atmospheric foreground emission is an important contaminant. Interestingly, at frequencies above 300 GHz, where CO is less of a concern, the atmospheric foreground becomes a critical factor (Choi et al. 2020). This challenge can be addressed proactively by simulating mock time-ordered data. Since atmospheric foreground components vary with time, it is critical to address these variations early in the processing stage while the data remain in time-ordered form.

4.2.4 Forward modeling

Another issue that requires further investigation is the translation of PS measurements into constraints on key astrophysical parameters. In general, the higher the quality of the measurements, the fewer assumptions are needed to extract astrophysical information. This suggests that, at least in the early stages of observations, we will likely rely on forward modeling (for a review, Cranmer et al. 2020) to derive constraints on the astrophysics of galaxies. In this process, the predicted power spectrum is compared with the actual results, and extreme models are rejected as

implausible. Consequently, models for submillimeter lines should become more sophisticated than those currently in use, which were originally developed only to test feasibility and to plan survey scanning and masking strategies. Such improvements could be achieved by using machine learning algorithms to generate numerous realizations of mock data. These realizations would mimic simulations processed at the level of gas particles (as discussed in Sect. 4.2.1), each representing different values of key astrophysical parameters. Finally, the prediction should not be limited to the metric of the PS, but should extend to one- and three-point statistics, which are sensitive to non-Gaussianities (see Sect. 1.3.6), which are crucial for estimating the level of foreground pollution (Appendix B) and for tracing cosmological parameters.

In general, the future of forward modeling in astrophysics will be shaped by advances in techniques such as active learning and model-aware inference (Cranmer et al. 2020). Active learning optimizes the efficiency of forward modeling, by guiding simulations in choosing initial conditions that provide the most informative results for inference, using the information provided by all previous runs. This approach aims to obtain maximum information while keeping the number of realizations low. On the other hand, model-aware inference-also called differentiable simulation-allows the inference process to engage directly with the internal mechanics of the simulation. Rather than treating the simulation as a black box that returns only final results, model-aware inference taps into intermediate variables, gradients, or internal physical models used in the simulation. This access allows algorithms to track the influence of specific parameters throughout the simulation process, thereby improving the accuracy of parameter estimation. For example, by making simulators differentiable, it becomes possible to apply gradient-based optimization techniques, leading to faster convergence and more accurate fitting of complex models. By integrating these methods, forward modeling becomes increasingly adaptive, enabling faster and more accurate analysis of complex, high-dimensional data sets. These innovations are expected to significantly improve simulation-based inference, making it a cornerstone of future astrophysical studies.

4.2.5 Validating models and masking technique with upcoming FYST data

The upcoming FYST LIM survey marks an exciting time for the field. Once the first data are collected, we will have the opportunity to rigorously test our masking techniques against real observations and determine how accurately our predictions align with the observed [CII] power spectrum. These results will not only validate—or challenge—the models and methods we have developed but it will also refine our understanding of the early universe, particularly in terms of the star formation history and the role of faint galaxies during the epoch of reionization.

Bibliography

Aihara, H., Armstrong, R., Bickerton, S., et al. 2018, PASJ, 70, S8

Atek, H., Labbé, I., Furtak, L. J., et al. 2024, Nature, 626, 975

Becker, G. D., Bolton, J. S., Madau, P., et al. 2015, MNRAS, 447, 3402

Behroozi, P., Wechsler, R. H., Hearin, A. P., & Conroy, C. 2019, MNRAS, 488, 3143

Behroozi, P. S., Conroy, C., & Wechsler, R. H. 2010, ApJ, 717, 379

Behroozi, P. S., Wechsler, R. H., & Conroy, C. 2013, ApJ, 770, 57

Bernal, J. L., Caputo, A., & Kamionkowski, M. 2021, Phys. Rev. D, 103, 063523

Bernal, J. L. & Kovetz, E. D. 2022, A&ARv, 30, 5

Béthermin, M., Fudamoto, Y., Ginolfi, M., et al. 2020, A&A, 643, A2

Bouwens, R. J., Illingworth, G. D., Oesch, P. A., et al. 2015, ApJ, 803, 34

Bowman, J. D., Rogers, A. E. E., Monsalve, R. A., Mozdzen, T. J., & Mahesh, N. 2018, Nature, 555, 67

Boylan-Kolchin, M., Weisz, D. R., Johnson, B. D., et al. 2015, MNRAS, 453, 1503

Breysse, P. C., Kovetz, E. D., & Kamionkowski, M. 2016, Monthly Notices of the Royal Astronomical Society: Letters, 457, L127

CCAT-Prime Collaboration, Aravena, M., Austermann, J. E., et al. 2023, ApJS, 264, 7

Cheng, Y.-T., Chang, T.-C., & Bock, J. J. 2020, ApJ, 901, 142

Choi, S. K., Austermann, J., Basu, K., et al. 2020, Journal of Low Temperature Physics, 199, 1089

CONCERTO Collaboration, Ade, P., Aravena, M., et al. 2020, A&A, 642, A60

Condon, J. J. & Ransom, S. M. 2016, Essential Radio Astronomy

Cooksy, A. L., Blake, G. A., & Saykally, R. J. 1986, ApJ, 305, L89

Cothard, N. F., Choi, S. K., Duell, C. J., et al. 2020, Journal of Low Temperature Physics, 199, 898

Cranmer, K., Brehmer, J., & Louppe, G. 2020, Proceedings of the National Academy of Science, 117, 30055

Creque-Sarbinowski, C. & Kamionkowski, M. 2018, Phys. Rev. D, 98, 063524

Crites, A. T., Bock, J. J., Bradford, C. M., et al. 2014, in Millimeter, Submillimeter, and Far-Infrared Detectors and Instrumentation for Astronomy VII, ed. W. S. Holland & J. Zmuidzinas, Vol. 9153, International Society for Optics and Photonics (SPIE), 613 – 621

Day, P. K., LeDuc, H. G., Mazin, B. A., Vayonakis, A., & Zmuidzinas, J. 2003, Nature, 425, 817, pubMed-not-MEDLINE

Dayal, P. & Ferrara, A. 2018, Phys. Rep., 780, 1

De Looze, I., Cormier, D., Lebouteiller, V., et al. 2014a, A&A, 568, A62

De Looze, I., Cormier, D., Lebouteiller, V., et al. 2014b, A&A, 568, A62

DeBoer, D. R., Parsons, A. R., Aguirre, J. E., et al. 2017, PASP, 129, 045001

Dole, H., Lagache, G., Puget, J. L., et al. 2006, A&A, 451, 417

Draine, B. T. 2011, Physics of the Interstellar and Intergalactic Medium

Duell, C. J., Vavagiakis, E. M., Austermann, J., et al. 2020, in Society of Photo-Optical Instrumentation Engineers (SPIE) Conference Series, Vol. 11453, Millimeter, Submillimeter, and Far-Infrared Detectors and Instrumentation for Astronomy X, ed. J. Zmuidzinas & J.-R. Gao, 114531F

Euclid Collaboration, Moneti, A., McCracken, H. J., et al. 2022, A&A, 658, A126

Fan, X., Carilli, C. L., & Keating, B. 2006, ARA&A, 44, 415

Fixsen, D. J., Dwek, E., Mather, J. C., Bennett, C. L., & Shafer, R. A. 1998, The Astrophysical Journal, 508, 123

Gabrielpillai, A., Somerville, R. S., Genel, S., et al. 2022, MNRAS, 517, 6091

Gamow, G. 1946, Phys. Rev., 70, 572

Garaldi, E., Compostella, M., & Porciani, C. 2019, MNRAS, 483, 5301

García, R., Salazar, E., Rozo, E., et al. 2023, MNRAS, 521, 2464

Genel, S., Nelson, D., Pillepich, A., et al. 2018, MNRAS, 474, 3976

Graf, U. U., Honingh, N., Barrueto, I., et al. 2019, in Proc. of the 30th Int. Symp. on Space Terrahertz Technology (Curran Associates), 77

Gunn, J. E. & Peterson, B. A. 1965, ApJ, 142, 1633

Guo, Q., White, S., Li, C., & Boylan-Kolchin, M. 2010, MNRAS, 404, 1111

Hansen, S. M., Sheldon, E. S., Wechsler, R. H., & Koester, B. P. 2009, ApJ, 699, 1333

Harikane, Y., Ouchi, M., Inoue, A. K., et al. 2020, ApJ, 896, 93

Harrison, E. 1986, Nature, 322, 417

Hassan, S., Davé, R., Mitra, S., et al. 2018, MNRAS, 473, 227

Hauser, M. G., Arendt, R. G., Kelsall, T., et al. 1998, ApJ, 508, 25

Hollenbach, D. J. & Tielens, A. G. G. M. 1999, Rev. Mod. Phys., 71, 173

Irwin, K. D., Hilton, G. C., Wollman, D. A., & Martinis, J. M. 1996, Applied Physics Letters, 69, 1945

Karoumpis, C., Magnelli, B., Romano-Díaz, E., Haslbauer, M., & Bertoldi, F. 2022, A&A, 659, A12

Kashlinsky, A. 2005, Phys. Rep., 409, 361

Kawabe, R. 2018, in Atacama Large-Aperture Submm/mm Telescope (AtLAST), 18

Kelvin, L. 1901, The London, Edinburgh, and Dublin Philosophical Magazine and Journal of Science, 2, 161

Kohno, K., Kawabe, R., Tamura, Y., et al. 2020, in Society of Photo-Optical Instrumentation Engineers (SPIE) Conference Series, Vol. 11453, Millimeter, Submillimeter, and Far-Infrared Detectors and Instrumentation for Astronomy X, ed. J. Zmuidzinas & J.-R. Gao, 114530N

Kovetz, E., Breysse, P. C., Lidz, A., et al. 2019, BAAS, 51, 101

Kovetz, E. D., Viero, M. P., Lidz, A., et al. 2017, arXiv e-prints, arXiv:1709.09066

Kravtsov, A. V., Vikhlinin, A. A., & Meshcheryakov, A. V. 2018, Astronomy Letters, 44, 8

Lagache, G., Cousin, M., & Chatzikos, M. 2018, A&A, 609, A130

Lagache, G., Dole, H., & Puget, J. L. 2003, MNRAS, 338, 555

Leech, K. J., Völk, H. J., Heinrichsen, I., et al. 1999, MNRAS, 310, 317

Lehmer, B. D., Brandt, W. N., Alexander, D. M., et al. 2005, ApJS, 161, 21

Li, T. Y., Wechsler, R. H., Devaraj, K., & Church, S. E. 2016, ApJ, 817, 169

Lin, Y.-T., Mohr, J. J., & Stanford, S. A. 2004, ApJ, 610, 745

Lu, T.-Y., Mason, C. A., Hutter, A., et al. 2024, MNRAS, 528, 4872

Martin, D. H. & Puplett, E. 1970, Infrared Physics, 10, 105

McQuarrie, D. 1973, Statistical Mechanics, Harper's chemistry series (Harper and Row)

Mitra, S., Choudhury, T. R., & Ferrara, A. 2018, MNRAS, 473, 1416

Moster, B. P., Naab, T., & White, S. D. M. 2013, MNRAS, 428, 3121

Moster, B. P., Somerville, R. S., Maulbetsch, C., et al. 2010, ApJ, 710, 903

Nelson, D., Pillepich, A., Genel, S., et al. 2015, Astronomy and Computing, 13, 12

Nelson, D., Pillepich, A., Springel, V., et al. 2018, MNRAS, 475, 624

Nikola, T., Stacey, G. J., Freundt, R. G., et al. 2023, in Physics and Chemistry of Star Formation: The Dynamical ISM Across Time and Spatial Scales, ed. V. Ossenkopf-Okada, R. Schaaf, I. Breloy, & J. Stutzki, 352

Olbers, H. W. 1823, Astronomisches Jahrbuch für das Jahr 1826, also appeared in Edinburgh New Philosophical Journal, 1, 141-150 (1826)

OpenAI. 2024, dALL-E.

Partridge, R. B. & Peebles, P. J. E. 1967, ApJ, 148, 377

Pénin, A., Doré, O., Lagache, G., & Béthermin, M. 2012, A&A, 537, A137

Penzias, A. A. & Wilson, R. W. 1965, ApJ, 142, 419

Perot, A. & Fabry, C. 1899, ApJ, 9, 87

Pillepich, A., Nelson, D., Springel, V., et al. 2019, MNRAS, 490, 3196

Pillepich, A., Springel, V., Nelson, D., et al. 2018a, MNRAS, 473, 4077

Pillepich, A., Springel, V., Nelson, D., et al. 2018b, MNRAS, 473, 4077

Planck Collaboration, Ade, P. A. R., Aghanim, N., et al. 2013, A&A, 557, A52

Planck Collaboration, Ade, P. A. R., Aghanim, N., et al. 2016, A&A, 594, A13

Planck Collaboration, Aghanim, N., Akrami, Y., et al. 2020, A&A, 641, A1

Poe, E. A. 1848, Eureka: A Prose Poem (New York: Putnam)

Poe, E. A. 1976, The Science Fiction of Edgar Allan Poe, ed. H. Deaver (Harmondsworth: Penguin), 17–174

Pritchard, J. R. & Loeb, A. 2012, Reports on Progress in Physics, 75, 086901

Puget, J. L., Abergel, A., Bernard, J. P., et al. 1996, A&A, 308, L5

Reddick, R. M., Wechsler, R. H., Tinker, J. L., & Behroozi, P. S. 2013, ApJ, 771, 30

Robertson, B. E. 2022, ARA&A, 60, 121

Schaerer, D., Ginolfi, M., Béthermin, M., et al. 2020a, A&A, 643, A3

Schaerer, D., Ginolfi, M., Béthermin, M., et al. 2020b, A&A, 643, A3

Silva, M. B., Kovetz, E. D., Keating, G. K., et al. 2021, Experimental Astronomy, 51, 1593

Singh, S., Subrahmanyan, R., Udaya Shankar, N., et al. 2018, ApJ, 858, 54

Springel, V., Pakmor, R., Pillepich, A., et al. 2018, MNRAS, 475, 676

Stacey, G. J., Aravena, M., Basu, K., et al. 2018, in Society of Photo-Optical Instrumentation Engineers (SPIE) Conference Series, Vol. 10700, Proc. SPIE, 107001M

Stacey, G. J., Geis, N., Genzel, R., et al. 1991, ApJ, 373, 423

Sun, G., Chang, T. C., Uzgil, B. D., et al. 2021, ApJ, 915, 33

Switzer, E. R., Barrentine, E. M., Cataldo, G., et al. 2021, Journal of Astronomical Telescopes, Instruments, and Systems, 7, 044004

Tacchella, S., Diemer, B., Hernquist, L., et al. 2019, MNRAS, 487, 5416

Uzgil, B. D., Aguirre, J. E., Bradford, C. M., & Lidz, A. 2014, ApJ, 793, 116

van Kampen, E., Bakx, T., De Breuck, C., et al. 2024, arXiv e-prints, arXiv:2403.02806

Vavagiakis, E. M., Ahmed, Z., Ali, A., et al. 2018, in Society of Photo-Optical Instrumentation Engineers (SPIE) Conference Series, Vol. 10708, Millimeter, Submillimeter, and Far-Infrared Detectors and Instrumentation for Astronomy IX, ed. J. Zmuidzinas & J.-R. Gao, 107081U

Vieira, J., Aguirre, J., Bradford, C. M., et al. 2020, arXiv e-prints, arXiv:2009.14340

Wang, L. & Jing, Y. P. 2010, MNRAS, 402, 1796

Wechsler, R. H., Gross, M. A. K., Primack, J. R., Blumenthal, G. R., & Dekel, A. 1998, ApJ, 506, 19

Wechsler, R. H. & Tinker, J. L. 2018, ARA&A, 56, 435

Weinberger, R., Springel, V., Hernquist, L., et al. 2017, MNRAS, 465, 3291

Weisstein, E. W. 2024a, Fourier Series, https://mathworld.wolfram.com/FourierSeries.html, from MathWorld–A Wolfram Web Resource

Weisstein, E. W. 2024b, Fourier Transform, https://mathworld.wolfram.com/FourierTransform.html, from MathWorld–A Wolfram Web Resource

Wise, J. H. 2019, arXiv e-prints, arXiv:1907.06653

Yang, X., Mo, H. J., & van den Bosch, F. C. 2009, ApJ, 695, 900

Yang, X., Mo, H. J., van den Bosch, F. C., Zhang, Y., & Han, J. 2012, ApJ, 752, 41

Yue, B., Ferrara, A., Pallottini, A., Gallerani, S., & Vallini, L. 2015, MNRAS, 450, 3829

Zaroubi, S. 2013, Astrophysics and Space Science Library, Vol. 396, The Epoch of Reionization, ed. T. Wiklind, B. Mobasher, & V. Bromm, 45

Zheng, Z., Coil, A. L., & Zehavi, I. 2007, ApJ, 667, 760

Zou, B., Choi, S. K., Cothard, N. F., et al. 2022, in Society of Photo-Optical Instrumentation Engineers (SPIE) Conference Series, Vol. 12190, Millimeter, Submillimeter, and Far-Infrared Detectors and Instrumentation for Astronomy XI, ed. J. Zmuidzinas & J.-R. Gao, 121902B

APPENDIX A

[CII] line intensity mapping the epoch of reionization with the Prime-Cam on FYST I. Line intensity mapping predictions using the Illustris TNG hydrodynamical simulation

The publication *Karoumpis et al. A&A (2022) 659, A12* is reproduced below in its original form with permission by ESO.

A&A 659, A12 (2022)
https://doi.org/10.1051/0004-6361/202141293

Astronomy & Astrophysics

[CII] line intensity mapping the epoch of reionization with the Prime-Cam on FYST

I. Line intensity mapping predictions using the Illustris TNG hydrodynamical simulation

C. Karoumpis[1], B. Magnelli[1], E. Romano-Díaz[1], M. Haslbauer[2,3], and F. Bertoldi[1]

[1] Argelander Institut für Astronomie, Universität Bonn, Auf dem Hügel 71, 53121 Bonn, Germany
e-mail: karoumpis@astro.uni-bonn.de
[2] Helmholtz-Institut für Strahlen- und Kernphysik, University of Bonn, Nussallee 14-16, 53115 Bonn, Germany
[3] Max-Planck-Institut für Radioastronomie, Auf dem Hügel 69, 53121 Bonn, Germany

Received 12 May 2021 / Accepted 16 November 2021

ABSTRACT

Aims. We predict the three-dimensional intensity power spectrum (PS) of the [CII] 158 μm line throughout the epoch of (and post) reionization at redshifts from ≈3.5 to 8. We study the detectability of the PS in a line intensity mapping (LIM) survey with the Prime-Cam spectral-imager on the *Fred Young* Submillimeter Telescope (FYST).
Methods. We created mock [CII] tomographic scans in redshift bins at $z \approx 3.7$, 4.3, 5.8, and 7.4 using the Illustris TNG300-1 ΛCDM simulation and adopting a relation between the star formation activity and the [CII] luminosity ($L_{[CII]}$) of galaxies. A star formation rate (SFR) was assigned to a dark matter halo in the Illustris simulation in two ways: (i) we adopted the SFR computed in the Illustris simulation and, (ii) we matched the abundance of the halos with the SFR traced by the observed dust-corrected ultraviolet luminosity function of high-redshift galaxies. The $L_{[CII]}$ is related to the SFR from a semi-analytic model of galaxy formation, from a hydrodynamical simulation of a high-redshift galaxy, or from a high-redshift [CII] galaxy survey. The [CII] intensity PS was computed from mock tomographic scans to assess its detectability with the anticipated observational capability of the FYST.
Results. The amplitude of the predicted [CII] intensity power spectrum varies by more than a factor of 10, depending on the choice of the halo-to-galaxy SFR and the SFR-to-$L_{[CII]}$ relations. In the planned $4° \times 4°$ FYST LIM survey, we expect a detection of the [CII] PS up to $z \approx 5.8$, and potentially even up to $z \approx 7.4$. The design of the envisioned FYST LIM survey enables a PS measurement not only in small (<10 Mpc) shot noise-dominated scales, but also in large (>50 Mpc) clustering-dominated scales making it the first LIM experiment that will place constraints on the SFR-to-$L_{[CII]}$ and the halo-to-galaxy SFR relations simultaneously.

Key words. galaxies: high-redshift – galaxies: statistics – galaxies: evolution – radio lines: galaxies – dark ages, reionization, first stars – large-scale structure of Universe

1. Introduction

The epoch of reionization (EoR), which took place 300–1000 million years after the Big Bang, was a period of radical changes in the Universe. The appearance of the first proto-galaxies was followed by the second known hydrogen phase transition–after the one that occurred during recombination–this time from neutral to fully ionized. What triggered this transition and its relation to the appearance of the first light sources is still under investigation. The star formation in galaxies, especially those with low stellar mass, is assumed to be the primary energy source behind the reionization (e.g., Zaroubi 2013; McQuinn 2016), even though there have been many debates on the role of the active galactic nuclei (AGN) as alternative energy sources (e.g., Madau & Haardt 2015; Kulkarni et al. 2017; Chardin et al. 2017; Hassan et al. 2018; Mitra et al. 2018; Garaldi et al. 2019). The EoR was followed by a period of rapid galaxy maturation (1–1.5 million years after the Big Bang, from now on post-EoR) when galaxies build up their stellar mass and the rest of the characteristic properties (e.g., gas and dust mass, star formation rate), approaching those observed in local galaxies. Although there is a consensus picture developing on the observational characteristics (e.g., rest-frame UV, IR, submillimeter, and radio luminosity) of post-EoR galaxies (e.g., Madau & Dickinson 2014), most of those are still biased toward the brightest objects, with the few exceptions that already seem to report tensions with the current galaxy evolution models (e.g., Yang et al. 2019; Breysse et al. 2021).

Detecting the faintest EoR galaxies that, according to theoretical models, (e.g., Kuhlen & Faucher-Giguère 2012) powered the reionization of the Universe, as well as their immediate descendants, is one of the next challenges in observational astronomy. Although they are large in numbers, these faint sources might not be easily detectable by traditional galaxy surveys, even in those performed by the most powerful telescopes to date or the coming *James Webb* Space Telescope (JWST; Robertson et al. 2013; Álvarez-Márquez et al. 2019). An answer to this observational challenge might instead come from the line intensity mapping (LIM) technique, a method extensively used in 21-cm fluctuation research and currently utilized by several new projects focusing on different atomic and molecular lines (Kovetz et al. 2017). LIM measures the integrated

emission of spectral lines from galaxies, with its data products being three-dimensional tomographic scans for which line-of-sight distance information is directly acquired through its frequency dependence. As all photons coming from the targeted angle and line frequency are measured, that is, including those from galaxies too faint to be individually detected by any traditional galaxy survey, LIM of infrared lines can trace the total cosmic star formation rate density (SFRD) during the (post-)EoR, allowing thereby to estimate the total contribution of star-forming (SF) galaxies to the energy budget of the reionization. (e.g., Basu et al. 2004; Righi et al. 2008; Lidz et al. 2011; Gong et al. 2011, 2012, 2017; Breysse et al. 2014; Mashian et al. 2015; Yue et al. 2015; Yue & Ferrara 2019; Lidz & Taylor 2016; Comaschi & Ferrara 2016; Kovetz et al. 2017; Dumitru et al. 2019; Padmanabhan 2019; Chung et al. 2020). Additionally, due to its low angular and spectral resolution requirements, it can be performed over a large portion of the sky by dedicated, small-aperture, wide field of view instruments. This way, LIM will also trace the incipient large-scale structure of the matter distribution in the early Universe, which otherwise would be inaccessible to deep pencil-beam-like observations from the JWST. Finally, by cross-correlating maps of lines that trace different phases of the interstellar and intergalactic medium, LIM can provide a thorough picture of the phase transition of the intergalactic medium during the (post-)EoR (e.g., Gong et al. 2012; Dumitru et al. 2019).

The astrophysical information will be extracted from the intensity maps using a two-point statistics, more in concrete the power spectrum. The comoving three-dimensional spherically averaged power spectrum (PS) of the tomographic scans will be the primary measurement of the upcoming first generation of LIM experiments. Not only is PS a promising tool for constraining astrophysical parameters, but it also is the most feasible measurement as well: the mean intensity measurement will be challenged by the smoothness of the FIR continuum foreground emission, while the accuracy of higher-order statistics measurements will be seriously limited by their sample variance.

Among all the possible lines emitted by high-redshift galaxies, the fine structure line of single ionized carbon, [CII], at rest-frame 157.7 µm is of particular interest. Indeed, because the [CII] line is a dominant coolant in different phases of the interstellar medium (Carilli & Walter 2013), it is the brightest line in typical SF galaxies and corresponds to about 0.1–1% of their total bolometric luminosity (Crawford et al. 1985; Stacey et al. 1991; Wright et al. 1991; Lord et al. 1996). It has excellent potential as a dust-unbiased probe of the interstellar gas and the star formation activity of galaxies (e.g., De Looze et al. 2014). Finally, it is an ideal target for ground-based telescopes because its observed frequencies for galaxies at $z \approx 4-10$ lie in the submillimeter (submm) atmospheric windows.

In the coming decade, several new experiments will try to trace the evolution of the [CII] PS during the (post-)EoR. Examples include the Tomographic Intensity Mapping Experiment (TIME; Crites et al. 2014) mounted on the Arizona Radio Observatory (ARO) 12 meters radio telescope and the CarbON CII line in post-rEionisation and ReionisaTiOn epoch (CONCERTO; Serra et al. 2016; Lagache et al. 2018) mounted on the Atacama Pathfinder EXperiment (APEX) 12 meters radio telescope. In this paper, we focus our analysis on the capabilities of the Prime-Cam spectro-imager that will be mounted on the *Fred Young* Submillimeter Telescope (FYST[1]; Stacey et al. 2018; Vavagiakis et al. 2018; Choi, in prep.). FYST is a 6-meters diameter telescope with a large field of view, while the Prime-Cam spectro-imager will include a state-of-the-art Fabry-Perot (sub)millimetric spectrometer. FYST will be located at a high altitude (5600m) on Cerro Chajnantor, 600 meters above the ALMA plateau. With its large field of view and exquisite location, FYST will efficiently perform large (sub)mm surveys focusing primarily on intensity mapping and cosmic microwave background observations.

To test the feasibility of the [CII] LIM experiment with FYST as well as to optimize its survey strategy, accurate predictions of the [CII] PS at the (post-)EoR are now urgently needed. To make such predictions in the Λ cold dark matter (CDM) framework, one usually starts from a mock dark matter (DM) halo lightcone catalog. Then, based on the DM halo properties, one predicts the star formation rate (SFR) of galaxies occupying them, either by using physical or empirical models. The former couple semi-analytic models of galaxy formation to DM-only simulations (Gong et al. 2012; Dumitru et al. 2019). The later match observations of UV galaxy surveys with analytic predictions of the DM halo mass function or halo catalogs coming from DM-only simulations, for example, by using the technique called abundance matching (e.g., Yue et al. 2015; Chung et al. 2020). Alternatively, there are also empirical models which, instead of using high-redshift observations, are calibrated using the cosmic infrared background (Serra et al. 2016) or [CII] surveys of local galaxies (Padmanabhan 2019). The different methods of assigning SFRs to galaxies in those DM halos can lead to a factor of four differences in [CII] PS forecasts (Chung et al. 2020).

The next step is to translate the SFR of each galaxy into a [CII] line luminosity ($L_{[\mathrm{CII}]}$) using a SFR-to-$L_{[\mathrm{CII}]}$ relation. Despite the complex emission mechanisms, the [CII] emission strongly correlates with the SFR of galaxies in the local Universe. However, for galaxies at higher redshifts, we have to rely on much sparser empirical constraints. Thus, previous works on high-redshift [CII] PS have either used scaling relations based on local Universe observations (e.g., Spinoglio et al. 2012; De Looze et al. 2014; Herrera-Camus et al. 2015) or simulations of high-redshift galaxies (e.g., Vallini et al. 2015). The different SFR-to-$L_{[\mathrm{CII}]}$ scaling relations can lead to up to two orders of magnitude differences in the predicted [CII] PS (Yue & Ferrara 2019).

The combination of these two very uncertain steps seems to result in more than two orders of magnitude inconsistencies in the [CII] PS predictions found in the literature (Gong et al. 2012; Silva et al. 2015; Serra et al. 2016; Chung et al. 2020; Dumitru et al. 2019; Padmanabhan 2019). Still, a consistent comparison between these forecasts is challenging because they are based on different assumptions and cosmological models (e.g., different spatial and mass resolution, ways of generating the DM-halo catalog). These discrepancies hamper the design of LIM surveys and prevent us from assessing realistically the constraints one will obtain from LIM experiments. In this paper, we produce a set of alternative [CII] PS predictions to study their differences coherently, allowing the optimization of the FYST LIM survey strategy. To do so, we start from a common dark matter cone built using the DM halo catalog of the Illustris TNG300-1 (from now on TNG300-1) hydrodynamical simulation. Subsequently, we apply different models of occupying the DM halos with mock galaxies as well as various SFR-to-$L_{[\mathrm{CII}]}$ coupling relations. Finally, from all these versions of mock [CII] tomographic scans, we predict the range of possible values probed by the [CII] PS during the (post-)EoR and study the detectability of this signal by the Prime-cam spectro-imager mounted on the FYST.

[1] http://www.ccatobservatory.org

Our paper is organized as follows. In Sect. 2, we present our DM halo lightcone catalog, the two different methods used to populate its DM halos with galaxies (hydrodynamical simulation and abundance matching), and the three different SFR-$L_{[CII]}$ scaling relations used in this paper. In Sect. 3, we present our predictions of the [CII] mean intensity and [CII] PS at various redshifts and study the detectability of the PS with the FYST LIM survey. Finally, in Sect. 4 we discuss our results in the context of other state-of-the-art observatories targeting (post-)EoR galaxies.

This paper is part of a two-paper series. In the second paper, we will investigate ways of removing foreground contamination of astrophysical origin like the cosmic infrared background and carbon monoxide lines coming from lower redshift galaxies (Cheng et al. 2016; Sun et al. 2018).

We assume the same ΛCDM cosmology as in Illustris TNG: $\Omega_m = \Omega_{dm} + \Omega_b = 0.3089$, $\Omega_b = 0.0486$, $\Omega_\Lambda = 0.6911$, $\sigma_8 = 0.8159$, $n_s = 0.9667$, and $H_o = 100\,h\,\mathrm{km\,s^{-1}\,Mpc^{-1}}$ with $h = 0.6774$. This is consistent with Planck Collaboration XIII (2016).

2. Methods

2.1. Our common dark matter halo cone

The starting point in creating our multiple versions of the mock [CII] tomographic scans was producing a common DM halo cone, that is, a catalog of DM halos positioned in a three-dimensional space with a geometry similar to that observed by a telescope. This DM cone, which extends from an imaginary observer with a reverse time evolution along the line-of-sight, has a sky coverage of a $4° \times 4°$ region (i.e., the envisioned size of the Prime-Cam fields) and extends from $z = 0$ to $z \sim 10$, that is, well within the EoR. While DM halos at $z < 3.5$ are irrelevant for the present paper, they will be of utmost importance when we discuss ways of removing foreground contamination of astrophysical origin which affects the detection of the [CII] PS (Karoumpis et al., in prep.).

To construct this DM halo cone, we used the DM halo (Subfind object[2]) catalogs of the TNG300-1[3] simulation (for a detailed description of the simulation see Sect. 2.2). The DM halos were calculated using a two-step criterium: the first one consists of applying the friends-of-friends (FOF, Huchra & Geller 1982) algorithm, while the second step is a selection refinement following the Subfind (Rodriguez-Gomez et al. 2015) algorithm. The FOF algorithm was applied to the full DM particle distribution in order to create groups of DM particles with an inter-particle distance lower than 0.2× the mean interparticle separation. Because the algorithm was applied only to the DM particles, the other types of particles (gas, stars, BHs) were assigned to the same groups as their nearest DM particle. Every group was then refined by selecting only the gravitationally bound particles in every FOF group, that are classified into halos by the Subfind algorithm, requiring each halo to contain at least 20 particles, regardless of type. We note that there is the possibility to have more than one Subfind object in a FOF group, although this is rare for the (post-)EoR reshift, for example, only 6% of the FOF groups of the common DM halo cone have more than one Subfind object at $z = 5.8$. In that case, the most massive object was considered as the central halo and the remaining as its satellites. Because a DM particle in the TNG300-1 simulation has a mass of $5.9 \times 10^7\,M_\odot$, we only considered halos with masses greater than $3 \times 10^9\,M_\odot$, that is, with more than 50 DM particles. We verified that above this mass range, its inferred halo mass function, agrees with the theoretical predictions from Murray et al. (2013) and Sheth & Tormen (1999). We note that for the redshift range of interest ($z \sim 3.5-9$) galaxies residing in halos less massive than $3 \times 10^9\,M_\odot$ should have a negligible contribution to the reionization as their star formation activity is suppressed by photo-heating from the intergalactic medium (Thoul & Weinberg 1996; Gnedin 2000; Finlator et al. 2011; Noh & McQuinn 2014).

To convert the box-shaped geometry of the TNG300-1 simulation into a cone, we first placed the observer at one of the corners of the $z = 0$ cube and had them "look out" at it. We then remapped the Cartesian coordinates of the TNG300-1 halo catalog into right ascension (RA), declination (Dec), and distance from the observer. We converted the distance from the observer into a cosmological redshift and added to it the peculiar velocity of DM halos along the line-of-sight to get the observed redshift. Finally, we repeated these steps, placing along the line-of-sight new data cubes so that their simulated redshift matches the cosmological redshift seen by the observer. To eliminate the occurrence of periodically repeating structures, we applied three randomization transformations on every cube: random rotation, mirroring, and translation (see Croton et al. 2006).

2.2. The connection between galaxies and their dark matter halos

The next step in creating our [CII] tomographic scans was to populate with galaxies the DM halos of our common DM halo cone. We did so in two alternative ways. In Sect. 2.2.1, we populated them with the simulated galaxies from the TNG300-1 box itself. In Sect. 2.2.2, we populated the halos with galaxies following an abundance matching technique assuring that the observed high-redshift dust-corrected UV luminosity function of Bouwens et al. (2015) is reproduced.

2.2.1. The galaxies of the TNG300-1

The most physical way to model the halo-to-galaxy relation is to use hydrodynamical simulations. Indeed, these simulations combine the gravitational evolution of the different matter constituents (i.e., DM, gas, stars, and black holes), together with the magneto-hydrodynamical behavior of the gas component.

The Illustris TNG project (Pillepich et al. 2018b; Donnari et al. 2019) is an updated version of the original Illustris simulation (Nelson et al. 2015) and is to-date the most advanced example of large hydrodynamical simulations ran in a cosmological context. Here, we made use of their largest simulation box, the TNG300-1 ($L_{box} = 302.6\,\mathrm{Mpc}$, $M_{DM} = 5.9 \times 10^7\,M_\odot$, $M_{baryon} = 1.1 \times 10^7\,M_\odot$), enabling us to simulate a $4° \times 4°$ survey and accurately study the effect of clustering on the [CII] PS up to scales of 100 Mpc.

The TNG300-1 halo (i.e., Subfind object; see Sect. 2.1) catalogs obtained from the baryonic simulation provided as well, at each time output, the properties of the galaxy[4] hosted by each of these DM halos. Among these properties, two of them are of

[2] Object identified by the Subfind algorithm. Many refer to the Subfind objects as subhalos, here we refer to them as halos.
[3] https://www.tng-project.org/

[4] The definition of a simulated galaxy here is that of a Subfind object with stellar particles. As a result, the halos in our catalog do not host more than one galaxy, with the central halos containing the main galaxies and the rest, the satellites.

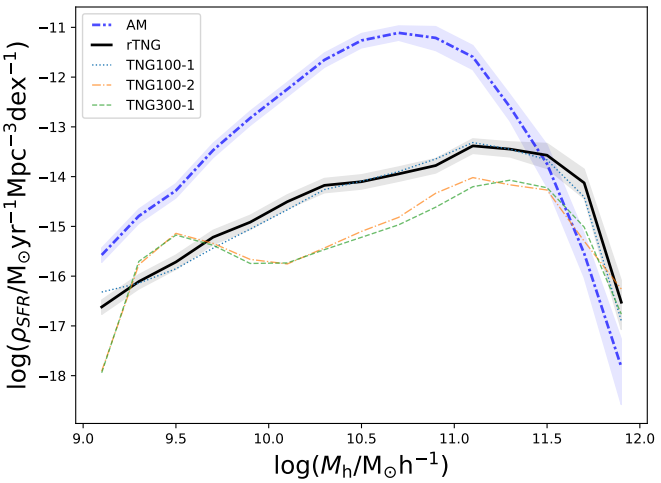

Fig. 1. Contribution of different halo mass range to the cosmic comoving star formation rate density at $z = 5.8$. The dotted blue, long-dash-dotted orange, and dashed green lines are inferred from the TNG100-1, TNG100-2, and TNG300-1 simulations, respectively. The solid black line is inferred from the renormalized TNG300-1 simulation (rTNG), according to Eq. (1). The dash-dotted light blue line is inferred by abundance matching (AM) our TNG300-1-based DM halo cone to the dust-corrected UV luminosity function of Bouwens et al. (2015, see Sect. 2.2.2). Gray and blue shaded areas are the 68% confidence integrals for rTNG and AM results, respectively, taking into account both the effects of the Poisson error and the sample variance.

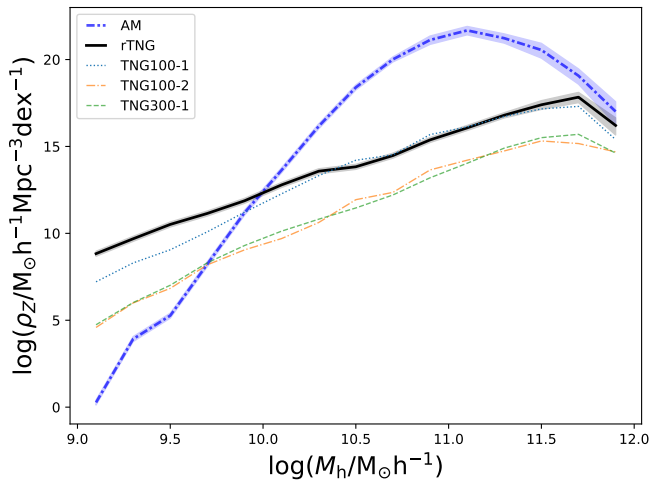

Fig. 2. Contribution of different halo mass range to the cosmic comoving mass density of metals locked in stars at $z = 5.8$. Lines and shaded areas are the same as in Fig. 1.

particular interest for us: their SFR and metallicity from which we predict their [CII] luminosity (see Sect. 2.3).

Being the simulation with the largest box in the project, TNG300-1 is naturally not the one with the best mass and spatial resolution. Compared to the flagship TNG100-1 simulation ($L_{\rm box} = 110.7$ Mpc, $M_{\rm DM} = 7.5 \times 10^6\,M_\odot$, $M_{\rm gas} = 1.4 \times 10^6\,M_\odot$), it has a factor of 8 (2) lower mass (spatial) resolution. In Fig. 1, we show how the cosmic SFR density inferred from these two simulations differs, especially for halos with $M_{\rm h} < 10^{11}\,M_\odot$, where there is an order of magnitude discrepancy. The reason is that during the TNG run, there are no on-the-fly adjustments or rescaling to achieve resolution convergence (Pillepich et al. 2018b). Specifically, for star formation, the difference is related to how gas turns into stars in the Illustris TNG simulations (Pillepich et al. 2018a,b). Stars form stochastically on a given timescale (i.e., $t_{\rm SFR}$) from gas cells that exceed a given density threshold (i.e., $\varrho_{\rm SFR}$). These timescales and density thresholds are the same at all resolutions, with $t_{\rm SFR} = 2.2$ Gyr and $\varrho_{\rm SFR} = 0.1$ neutral hydrogen atoms per cm^3. A better spatial and mass resolution leads to the sampling of higher gas density regions, allowing more gas to fuel star formation. More SF fuel leads to a higher SFR at fixed halo mass, with increasing resolution (Pillepich et al. 2018a,b). Because the metallicity is a function of stellar mass and SFR (Eq. (14)), we notice similar discrepancies at $M_{\rm h} < 10^{11}\,M_\odot$ between the cosmic mass density of metals (i.e., $\varrho_{\rm Z}$) predicted at $z = 5.8$ by the TNG300-1 and TNG100-1 simulations (Fig. 2).

Thanks to the set of TNG realizations, we could quantify how the different resolutions affect the predictions of these simulations. TNG100-1 and TNG300-1 each come with a series of lower resolution realizations of the same volume, with eight and 64 times more massive DM particles (i.e., TNG100-2, TNG100-3, TNG300-2, and TNG300-3). Despite the changes in box size and initial conditions, the cosmic SFR density predicted from TNG100-2 is in very good agreement with that of TNG300-1 (Fig. 1). Based on the minor influence of the different simulation volumes on the results and following Pillepich et al. (2018a), we assumed that the outcome of the TNG100-1 simulation, which has the finest (DM and baryonic) mass resolution, is the best estimate of the galactic SFR and rescaled the SFR of the TNG300-1 galaxies on a halo-by-halo basis, as:

$$\mathrm{SFR}(M_{\rm h};\,\mathrm{rTNG}) = \mathrm{SFR}(M_{\rm h};\,\mathrm{TNG300-1}) \times \frac{\overline{\mathrm{SFR}}(M_{\rm h} \in [M_{\rm h} \pm 0.25\,\mathrm{dex}];\,\mathrm{TNG100-1})}{\overline{\mathrm{SFR}}(M_{\rm h} \in [M_{\rm h} \pm 0.25\,\mathrm{dex}];\,\mathrm{TNG100-2})}. \quad (1)$$

We applied the same halo-by-halo correction to the metallicities of each galaxies,

$$\mathrm{Z}(M_{\rm h};\,\mathrm{rTNG}) = \mathrm{Z}(M_{\rm h};\,\mathrm{TNG300-1}) \times \frac{\overline{\mathrm{Z}}(M_{\rm h} \in [M_{\rm h} \pm 0.25\,\mathrm{dex}];\,\mathrm{TNG100-1})}{\overline{\mathrm{Z}}(M_{\rm h} \in [M_{\rm h} \pm 0.25\,\mathrm{dex}];\,\mathrm{TNG100-2})}. \quad (2)$$

From now on, predictions inferred from this rescaled cone catalog will be denoted "rTNG".

Finally, as one can see in Fig. 1, the curve of the cosmic SFR density inferred from TNG100-1 at $M_{\rm h} < 10^{10}\,M_\odot$ does not have the same shape as those inferred from the TNG100-2 and TNG300-1 simulations, which exhibit a peak at $M_{\rm h} = 10^{9.5}\,M_\odot$. Indeed, at $M_{\rm h} < 10^{10}\,M_\odot$ independently of the redshift, the lower resolution of the TNG100-2 and TNG300-1 simulations drastically affect the formation and evolution of galaxies residing in such low-mass halos resulting in either an overestimation or an underestimation of their number density depending on the $M_{\rm h}$-bin. There, our simple halo-by-halo rescaling approach could not be applied, which forced us to limit this cone catalog to galaxies hosted by $M_{\rm h} > 10^{10}\,M_\odot$ halos. The importance for the [CII] PS of (post-)EoR galaxies located in DM halos with $3 \times 10^9 < M_{\rm h}/M_\odot < 10^{10}$ was thus only assessed using the alternative method of abundance matching.

2.2.2. Abundance matching

Abundance matching (AM) is a method based on the simple hypothesis that the most massive galaxies occupy the most massive halos. Starting from the observed stellar mass function at

a given redshift, one creates a mock population of galaxies and then matches them accordingly to the halos. The DM mass is, however, not the only halo property that can be matched to the observed stellar mass function. According to the latest studies of the halo-to-galaxy relation (Wechsler & Tinker 2018), it is not even the optimal choice: using mass as the matching quantity neglects the fact that when a halo enters the gravity field of a larger neighboring halo, it is affected by intense tidal stripping; matching the mass of this halo after the stripping would hence result into incorrect galaxy properties. Therefore, we chose to perform our abundance matching technique using a halo property less influenced by the tidal stripping than its mass. Following Kravtsov et al. (2004) and Béthermin et al. (2017), we used the maximum value of the spherically-averaged rotation curve of the halo, that is, $V_{\rm max}$.

Unfortunately, there exists to date no observational constraints on the galaxy stellar mass function at the EoR. Fortunately, at such high redshift, performing AM using a SFR function well constrained by HST observations is to first order as appropriate as using a stellar mass function (Yue et al. 2015; Yue & Ferrara 2019). Indeed, at $z \gtrapprox 4$, the probability for a galaxy hosted on a $M_{\rm h} > 10^{10}\,M_{\odot}$ halo to be non-SF is close to zero (Béthermin et al. 2017) and there exists a tight correlation between the stellar mass and the SFR of SF galaxies at all redshifts probed to-date, the so-called main sequence of SF galaxies (e.g., Speagle et al. 2014). We also note that performing the AM using the SFR function instead of the stellar mass function has the advantage to reduce the number of steps from AM to $L_{\rm [CII]}$, as the [CII] luminosity of high-redshift galaxies is expected to scale with their SFRs (e.g., Olsen et al. 2015; Vallini et al. 2015; Lagache et al. 2018; Schaerer et al. 2020). We started, therefore, from the observed UV luminosity function, which is described by a Schechter function (Schechter 1976), written in terms of magnitude:

$$\frac{{\rm d}n}{{\rm d}M_{\rm UV}} = 0.4\ \ln(10)\,\phi_*\,x^{(1+\alpha)}\,e^{-x}\,, \tag{3}$$

where $x = 10^{0.4\,(M^*_{\rm UV}-M_{\rm UV})}$, with $M_{\rm UV}$ being the dust-attenuated absolute AB magnitude, α is the faint-end slope parameter, ϕ_* is the characteristic number of galaxies per comoving volume, and $M^*_{\rm UV}$ is the characteristic absolute magnitude, at which the luminosity function exhibits a rapid change in its slope (Schechter 1976). According to Bouwens et al. (2015), in the redshift range 4 to 9:

$$\begin{aligned} M^*_{\rm UV} &= -20.96 + 0.01\,(z-6),\\ \phi_* &= 0.46\times10^{-3\,-0.27\,(z-6)},\\ \alpha &= -1.87 - 0.10\,(z-6). \end{aligned} \tag{4}$$

In order to derive the SFR of our mock galaxy population, we needed to take into account the dust attenuation and calculate the dust-corrected UV luminosity function, which subsequently could be converted into a SFR function. Following Yue & Ferrara (2019), we used the coefficients of Koprowski et al. (2018), where the dust-corrected absolute magnitude is

$$M'_{\rm UV} = M_{\rm UV} - A_{1600}, \tag{5}$$

where

$$A_{1600} = 4.85 + 2.10\,\beta(\geq 0), \tag{6}$$

is the dust attenuation at 1600 Å and β is the measured UV spectral slope, that is,

$$f_\lambda \propto \lambda^\beta. \tag{7}$$

The spectral slope β depends on $M_{\rm UV}$ and was fitted by

$$\beta = \beta_{-19.5} + \frac{{\rm d}\beta}{{\rm d}M_{\rm UV}}(M_{\rm UV} + 19.5). \tag{8}$$

From Bouwens et al. (2015) we have:

$$\begin{aligned} \beta_{-19.5} &= -1.97 - 0.06\,(z-6),\\ \frac{{\rm d}\beta}{{\rm d}M_{\rm UV}} &= -0.18 - 0.03\,(z-6). \end{aligned} \tag{9}$$

The dust-corrected UV luminosity function was then related to the measured UV luminosity function via

$$\frac{{\rm d}n'}{{\rm d}M'_{\rm UV}}(M'_{\rm UV}, z) = \frac{{\rm d}n}{{\rm d}M_{\rm UV}}(M_{\rm UV}, z). \tag{10}$$

We assumed that the dust-corrected UV luminosity is linked to the DM mass halo function via a monotonic $M_{\rm h} - M'_{\rm UV}$ relation with a 0.2 dex log-normal scatter (Corasaniti et al. 2017). In order to match our dust-corrected luminosity function to the halo mass function, we had to assume a monotonic function without scatter: this way, there is an exact, "direct" match of DM halos ordered by their mass and galaxies ordered by their UV magnitude. To get to this direct luminosity function, we re-wrote the dust corrected UV luminosity function as:

$$\frac{{\rm d}n'}{{\rm d}M'_{\rm UV}} = \left(\frac{{\rm d}n'}{{\rm d}M'_{\rm UV}}\right)_{\rm direct} * P_{\rm s}, \tag{11}$$

where "$*$" denotes the convolution operation and $P_{\rm s}$ describes the log-normal scatter of the $M_{\rm h} - M'_{\rm UV}$ relation. $M_{\rm h} - M'_{\rm UV,\,direct}$ is a monotonic relation without scatter, suitable for the AM method, that is,

$$\left(\frac{{\rm d}n'}{{\rm d}M'_{\rm UV}}\right)_{\rm direct} = \frac{{\rm d}N}{{\rm d}\log M_{\rm h}}\frac{{\rm d}\log M_{\rm h}}{{\rm d}M'_{\rm UV}}, \tag{12}$$

where N is the number of DM halos. To perform the abundance matching of our dust-obscured UV luminosity function to the DM halo mass function via this direct dust-obscured UV luminosity function technique, we used the code of Yao-Yuan Mao[5] that provides a python wrapper around the deconvolution kernel described in Behroozi et al. (2010). In this way, we obtained for each DM halo within our cone, the direct dust-corrected UV absolute magnitude ($M'^{\rm direct}_{\rm UV}$) and the "observed" dust-correct UV absolute magnitude (i.e., $M'_{\rm UV}$) of its embedded galaxy. We should stress that these direct magnitudes were only used to perform the abundance matching, while the SFR of galaxies residing in these DM halos were computed from their observed magnitude. To do so, we converted their dust-corrected UV absolute magnitude, into SFR following Kennicutt (1998), that is,

$${\rm SFR} = \frac{4\pi\times3.08\times10^{19}\times10^{-0.4\,(M'_{\rm UV}+48.6)}}{l_{\rm UV}}, \tag{13}$$

where $l_{\rm UV} = 8.9\times10^{27}\,{\rm erg\,s^{-1}Hz^{-1}}\,(M_{\odot}/{\rm yr})^{-1}$ (Yue et al. 2015, assuming a metallicity of 0.1 $Z_{\odot}$, a stellar age of 10% the Hubble time, and a Salpeter initial mass function between 0.1−100 $M_{\odot}$).

One of the $L_{\rm [CII]}$-SFR coupling relations used (Vallini et al. 2015, introduced in Sect. 2.3), also depends on the metallicity of

[5] https://github.com/yymao/abundancematching

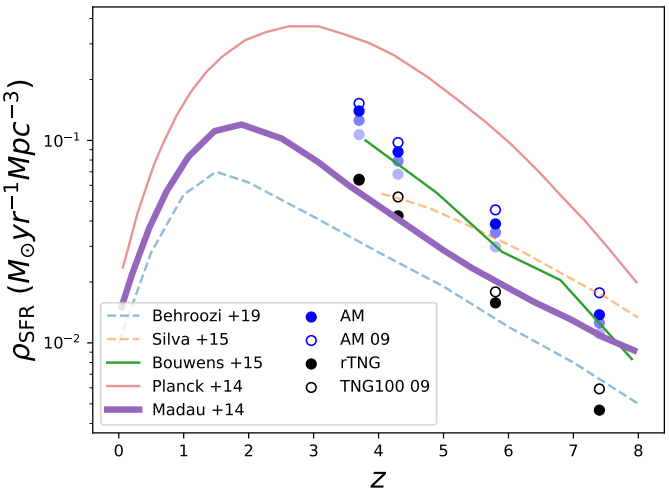

Fig. 3. Redshift evolution of the cosmic SFRD as inferred from our rTNG (black dots) and AM (dark blue dots) models. Our AM results are also presented for a slightly different dust correction similar to that used in Bouwens et al. (2015, blue dots) and for a cone catalog restricted to galaxies not brighter than the brightest SF galaxies observed in the pencil-beam survey of Bouwens et al. (2015, light blue dots). The empty blue and black circles is our AM and TNG100 prediction for the lower halo mass limit of $M_h = 3 \times 10^9\,M_\odot$. The solid green, red, and purple lines present observational constraints from Bouwens et al. (2015), Planck Collaboration XXX (2014), and Madau & Dickinson (2014), respectively. The dashed blue line is the UNIVERSE Machine prediction (Behroozi et al. 2019) and the dashed orange line is the SFRD that comes from analytically integrating the M_h-to-SFR relation of Silva et al. (2015) over all halo masses.

our galaxies. Those metallicities were inferred using the fundamental metallicity relation (Mannucci et al. 2010),

$$\begin{aligned}\log(Z) = {} & 0.21 + 0.37\log\left(M_*/10^{10}\right) - 0.14\ \log(\mathrm{SFR}) \\ & - 0.19\ \log^2\left(M_*/10^{10}\right) - 0.054\log^2(\mathrm{SFR}) \\ & + 0.12\ \log\left(M_*/10^{10}\right)\ \log(\mathrm{SFR}),\end{aligned} \tag{14}$$

where the stellar mass, M_*, of our AM galaxies was obtained from the latest measurement of the mass-to-UV-light ratio (Duncan et al. 2014),

$$\log\left(M_*\right) = -1.69 - 0.54\,M_{\mathrm{UV}}. \tag{15}$$

The fact that the DM halos were connected to the [CII] emission according to the above observational relations means that the only mass resolution that limits the AM method is that of the DM particle. With this method, we could thus investigate the influence of galaxies formed in low mass halos –that is, $3 \times 10^9 < M_h/M_\odot < 10^{10}$– not accounted for in our rTNG simulation. We did so by applying the AM twice: assuming a DM halo mass lower limit of $10^{10}\,M_\odot$ (i.e., matching the limit of our rTNG catalog) and considering an even lower limit of $3{\times}10^9\,M_\odot$.

In Fig. 3, we compare the redshift evolution of the cosmic SFR densities (SFRD) as predicted by our rTNG and AM models to observational constraints and simulation predictions from the literature. Our rTNG predictions are in good agreement with measurements from Madau & Dickinson (2014), which at these redshifts are mostly based on the dust-corrected UV luminosity functions of Bouwens et al. (2012a,b). On the contrary, our AM predictions lie significantly above $\times(2{-}3)$ these observations, although with values not as high as constraints from the Planck Collaboration XXX (2014). This was to be expected because the SFRD inferred in Bouwens et al. (2015) and from which our AM model is based also lies above the measurements of Madau & Dickinson (2014). We note, however, a 20–30% disagreement between our AM-based SFRD and those inferred in Bouwens et al. (2015). Part of this disagreement comes from adopting here different dust correction and l_{UV} values than in Bouwens et al. (2015, see blue dots in Fig. 3); furthermore our large simulated volume contains galaxies with higher SFRs than the brightest SF galaxies observed in Bouwens et al. (2015, see the light blue dots in Fig. 3). Last, our AM-based SFRD increases by 10–30% when accounting for the contribution of galaxies residing in $3 \times 10^9 < M_h/M_\odot < 10^{10}$ halos and not accounted for in our rTNG simulation (Fig. 3). For comparison we also plot the SFRD of the TNG100 snapshots, applying also the lower ($3 \times 10^9 < M_h/M_\odot$) DM halo mass limit, getting 0–10% higher values than the SFRD of rTNG.

Finally, to test for any potential influence of baryonic substructures (i.e., massive DM halos hosting more than one massive galaxy) on our AM result, we reapplied our method but this time by matching the UV luminosity function with the rTNG galaxies, based on their stellar masses, instead of the rTNG DM halos (Figs. 1 and 2). As it can be noticed, there is no significant deviation from the original AM result for $M_h > 10^{10}\,M_\odot$, suggesting that the number of halos hosting more than one galaxy is insignificant at our redshifts and halo mass bins of interest. The two results differ only at $M_h < 10^{10}\,M_\odot$ where the low mass resolution of the TNG300-1 simulation significantly affects its baryonic matter predictions (see Sect. 2.2.1), making the result of AM with DM halos more reliable.

2.3. The [CII] emission of galaxies at the (post-)EoR

The correlation between the [CII] luminosity and the SFR of galaxies results from the balance between the stellar feedback heating up the gas and the ability of [CII] to cool it by radiating energy away. Despite the simplicity of this premise, modeling the exact physics of the [CII] line emission is complex, as it originates from various phases of the interstellar medium (ISM). Those include photo-dissociation regions (PDRs), the warm ionized medium (WIM), and the warm and cold neutral medium (WNM, CNM; Croxall et al. 2017; Madden et al. 1997; Kaufman et al. 1999; Graciá-Carpio et al. 2011; Cormier et al. 2012; Appleton et al. 2013; Velusamy & Langer 2014; Pineda et al. 2014). In spite of these intricacies, a tight relation between SFR and $L_{[\mathrm{CII}]}$ has been reported in local galaxies (De Looze et al. 2014; Herrera-Camus et al. 2015). This relation seems to hold at $z > 4$, albeit with an increasing scatter (Carniani et al. 2018; Fujimoto et al. 2019, 2020; Schaerer et al. 2020). This scatter is, however, not surprising and actually predicted by hydrodynamical simulations and semi-analytical models (Vallini et al. 2015; Pallottini et al. 2015, 2017a,b; Olsen et al. 2017; Katz et al. 2017; Lagache et al. 2018). It seems to result from the interplay of different factors such as variation in metallicities, gas mass, and interstellar radiation fields of the galaxies during the (post-)EoR.

In this paper, we used three different scaling relations to study their influences on our [CII] PS forecasts:

1. Lagache et al. (2018, hereafter L18) assume that the bulk of the [CII] luminosity of high-redshift galaxies comes from their PDRs. They use a semi-analytic model of galaxy formation combined with the photo-ionization code `Cloudy` (Ferland et al. 2013, 2017) to calculate the luminosity of 28 000 mock galaxies at $z > 4$. They find that the [CII]

luminosity is a function of the SFR and the redshift of a galaxy,

$$\log\left(\frac{L_{[\rm CII]}}{L_\odot}\right) = (1.4-0.07\,z)\,\log\left(\frac{\rm SFR}{M_\odot\,{\rm yr}^{-1}}\right)+7.1-0.07\,z, \quad (16)$$

with a ∼0.5 dex scatter.

2. Vallini et al. (2015, hereafter V15) model a two-phase ISM consisting of PDRs and a CNM. They combine a radiative transfer hydrodynamical simulation of a $z = 6.6$ galaxy located in a $M_{\rm h} = 1.7\times10^{11}\,M_\odot$ halo with a subgrid ISM model and the PDR-code UCL_PDR (Bell et al. 2005, 2007; Bayet et al. 2009). Running their subgrid model for a range of SFR values, SFR = $[0.1-100\,M_\odot\,{\rm yr}^{-1}]$, they find that the [CII] luminosity depends not only on the SFR but also on the metal content of galaxies,

$$\log\left(\frac{L_{[\rm CII]}}{L_\odot}\right) = 7.0 + 1.2\,\log\left(\frac{\rm SFR}{M_\odot\,{\rm yr}^{-1}}\right) + 0.021\,\log\left(\frac{Z_g}{Z_\odot}\right) + 0.012\,\log\left(\frac{\rm SFR}{M_\odot\,{\rm yr}^{-1}}\right)\log\left(\frac{Z_g}{Z_\odot}\right) - 0.74\,\log^2\left(\frac{Z_g}{Z_\odot}\right). \quad (17)$$

There is no explicit redshift evolution and scatter predictions for this relation as it is derived from a $z = 6.6$ simulation. A scatter of ∼0.2 dex and ∼0.1 dex is, however, implicitly introduced by the distribution of metallicity at a given SFR in our rTNG and AM simulations. A redshift evolution is also implicitly introduced by the slight increase of the mean metallicity of galaxies from $z \sim 7.4$ to $z \sim 3.7$, but this evolution is mostly insignificant for these mean relations. Finally, we note that the mean relations inferred from the rTNG and AM models significantly differ at SFR $< 1\,M_\odot\,{\rm yr}^{-1}$, that is, SFRs where in the AM model galaxies have significantly lower metallicities and therefore lower [CII] luminosities than in the rTNG simulation.

3. Schaerer et al. (2020, hereafter A20) combine 75 [CII] robust detections and 43 upper limits, obtained by the ALMA Large Program to INvestigate C + (ALPINE) survey (Le Fèvre et al. 2020), with 36 earlier [CII] observations. They gather a sample of 154 main-sequence galaxies located between $4.4 < z < 9.1$. According to their Bayesian fit, the [CII] luminosity of a galaxy and its observational scatter are correlated to its SFR as:

$$\log\left(\frac{L_{[\rm CII]}}{L_\odot}\right) = (6.43\pm0.16) + (1.26\pm0.10)\log\left(\frac{\rm SFR}{M_\odot{\rm yr}^{-1}}\right). \quad (18)$$

While these three relations are overall in good agreement, their associated scatter considerably differs (Fig. 4). On the one hand, one should note that the scatter of A20 includes observational uncertainties and possible selection biases. Indeed, although the number of [CII] detections of high-redshift galaxies is growing, it is still not large enough for a detailed statistical analysis. On the other hand, calculating the intrinsic scatter with simulations is also challenging: hydrodynamical simulations of high-redshift galaxies still suffer from the small number of simulated objects and the limits imposed by the mass resolution on the modeling of the ISM. Therefore, one should be aware that scatter either reported from the observations or predicted by the simulations is still uncertain. We examine in Sects. 3.1 and 3.2 the influence of this scatter on the predicted mean [CII] line intensities and PS, respectively.

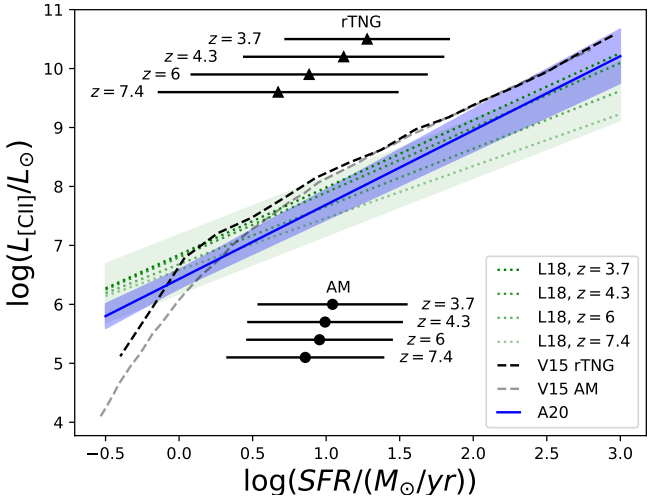

Fig. 4. SFR−$L_{[\rm CII]}$ relation applied to our cone, as predicted in L18 at $z \sim 3.7, 4.3, 5.8$, and 7.4 (green dotted lines) and observed in A20 at $4.4 < z < 9.1$ (blue line) along with its 1σ scatter (blue shaded region). For clarity, the redshift-independent 1σ scatter of 0.5 dex inferred in L18 is only shown around their $z = 5.8$ mean relation (green shaded region). The mean metallicity-dependent SFR − $L_{[\rm CII]}$ relation of V15 applied to our rTNG and AM models are shown by the dark and light gray dashed lines, respectively. The horizontal black lines represent the SFR ranges containing 25%−75% of the cumulative cosmic SFRD at $z \sim 3.7, 4.3, 5.8$, and 7.4 in our rTNG (triangles) and AM (circles) models. These ranges highlight the SFRs of galaxies that contribute the most to the cosmic SFRD at these redshifts.

2.4. [CII] tomographic scans of the (post-)EoR

From the cone catalogs generated in the previous sections, we created our mock three-dimensional tomographic scans, that is, data cubes in which each slice corresponds to a $4^\circ \times 4^\circ$ region of the sky and contains the cumulative [CII] emission of galaxies within a particular redshift range (equivalently frequency range). The properties of these three-dimensional tomographic scans–that is, frequency and spatial resolutions–were tailored to the specifications of the two spectrally/spatially multiplexing Fabry-Perot interferometers that will be placed in front of two of the Prime-Cam modules (Vavagiakis et al. 2018). This EoR spectrograph will observe the sky using four spectral windows of 40 GHz bandwidth each, that is, probing the [CII] line emitted at (z = [6.76−8.27], [5.34−6.31], [4.14−4.76], [3.42−3.87]), centered at $\nu_{[\rm CII]}/(1+7.45) = 225$ GHz, $\nu_{[\rm CII]}/(1+5.79) = 280$ GHz, $\nu_{[\rm CII]}/(1+4.43) = 350$ GHz, and $\nu_{[\rm CII]}/(1+3.64) = 410$ GHz; with spectral resolutions of 2.1, 2.7, 3.6, and 4.4 GHz; and beam full width at half maximum (FWHM) of 0.88, 0.77, 0.65 and 0.62 arcmin, respectively. For each of our cone catalogs, we thus generated four tomographic scans according to the beam size and spectral resolution of these four spectral windows. As a result, our 225, 280, 350, and 410 GHz tomographic scans include $(253\times253\times19)$, $(313\times313\times15)$, $(369\times369\times11)$, and $(387\times387\times9)$ voxels, respectively. The measured [CII] intensity in one of these voxels with observed central frequency, ν_0, is:

$$I_{[\rm CII]} = \frac{1}{(\Delta\theta_{\rm b})^2}\sum\frac{1}{\Delta\nu_0}\frac{L^j_{[\rm CII]}}{4\pi\,r_j^2(1+z_j)^2}, \quad (19)$$

where $\Delta\theta_{\rm b}$ is the angular size of the voxel, $\Delta\nu_0$ is its bandwidth, and r_j is the comoving distance of the jth galaxy which resides at a redshift z_j and have a [CII] luminosity $L^j_{[\rm CII]}$. We summed

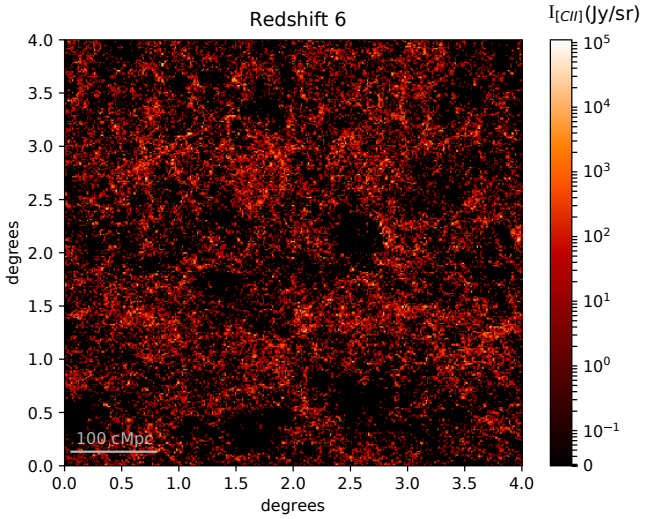

Fig. 5. [CII] line intensity map at $z = 5.8$ ($\nu_{\rm obs} = 280$ GHz) as predicted from our rTNG cone catalog using the SFR-$L_{\rm [CII]}$ scaling relation of Vallini et al. (2015).

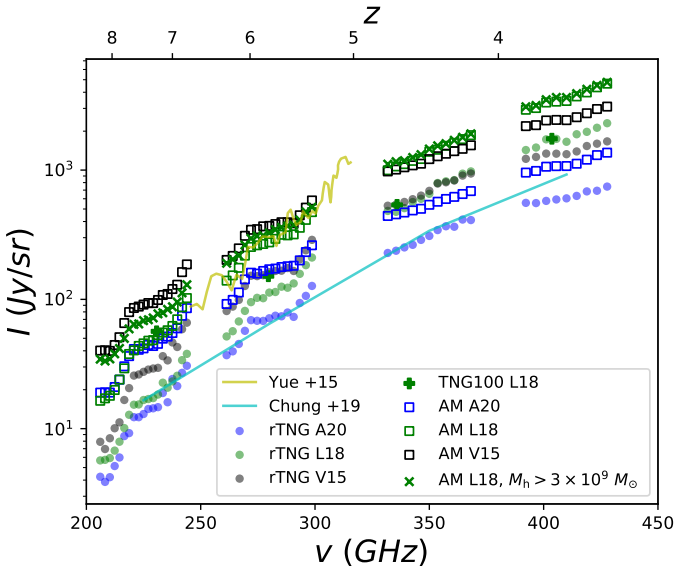

Fig. 6. Mean [CII] line intensity as a function of the observed frequency (equivalently, emitted redshift). Predictions from our rTNG and AM models are shown by dots and open squares, respectively. Symbols are color-coded according to the used SFR-to-$L_{\rm [CII]}$ relation, blue symbols for A20, green symbols for L18, and black symbols for V15. L18 is also plotted including the contribution of 3×10^9–$10^{10}\,M_\odot$ halos for our AM model (green x-shaped points) and the TNG100-1 snapshots (green plus-shaped points; see text for more details). Predictions from Yue et al. (2015, yellow line) and Chung et al. (2020, turquoise line) are also shown for comparison.

over every galaxy in the line-of-sight of our voxel that has a redshift yielding [CII] observed-frame frequency emission within the frequency range of our voxel, that is,

$$\frac{\nu_{\rm [CII]}}{\nu_0 + \Delta\nu_0/2} - 1 \leq z_j \leq \frac{\nu_{\rm [CII]}}{\nu_0 - \Delta\nu_0/2} - 1. \quad (20)$$

Figure 5 presents one "slice" of our [CII] tomography, corresponding to the [CII] line intensity map at $z = 5.8$ ($\nu_{\rm obs} = 280$ GHz) as predicted from our rTNG cone catalog using the SFR-$L_{\rm [CII]}$ scaling relation of V15. This map provides a visual intuition for the dimensions of the survey and the cosmological structures enclosed in it.

3. Results

3.1. The mean [CII] line intensity

In this section, we explore the effect of our different modeling approaches on the predicted mean [CII] line intensities emitted by (post-)EoR galaxies as a function of redshifts (equivalently observed frequencies).

The mean [CII] intensity, $\bar{I}_{\rm [CII]}$, estimated for all frequency channels of all our mock three-dimensional tomographic scans is shown in Fig. 6. All models predict a significant drop in $\bar{I}_{\rm [CII]}$ as we move to lower observing frequencies, equivalently to higher redshifts. This drop results naturally from (i) the cosmological dimming of the flux density of higher-redshift galaxies and (ii) the decline of the cosmic SFRD from $z \sim 3$ to $z \sim 8$ (Fig. 3). Despite all models following this general redshift trend, there is up to an order of magnitude offset between their predictions. Firstly, forecasts based on the same SFR-to-$L_{\rm [CII]}$ relation but different halo-to-galaxy SFR relation differs by a factor two at $z = 3.7, 4.3$, and 5.8 and a factor of three at $z = 7.4$, with the AM model yielding systematically higher mean [CII] line intensities. Secondly, forecasts based on the same halo-to-galaxy SFR relation but different SFR-to-$L_{\rm [CII]}$ relations also exhibit differences: at all redshifts, V15 yields a factor of two higher mean [CII] line intensities than A20; L18, the only relation with a significant redshift evolution, yields mean [CII] line intensities that are similar to those based on V15 at $z = 3.7$ and 4.3, and lie between V15 and A20 at $z = 5.8$, and in agreement with A20 at $z = 7$.

To track the origin of these differences to some specific parameters in our models, we study the analytical form of $\bar{I}_{\rm [CII]}$, which is given in unit of Jy/sr by,

$$\bar{I}_{\rm [CII]} = \int \frac{L_{\rm [CII]}}{4\pi D_L^2}\, y_{\rm [CII]}\, D_A^2\, \frac{{\rm d}n}{{\rm d}\log L_{\rm [CII]}}\, {\rm d}\log L_{\rm [CII]}, \quad (21)$$

where $y_{\rm [CII]} = \lambda_{\rm [CII],rest}(1+z)^2/H(z)$ is the derivative of the comoving radial distance with respect to the observed frequency, and $D_{\rm A}$ and $D_{\rm L}$ are the comoving angular and luminosity distances (e.g., Uzgil et al. 2014). Then, assuming a generalized form of the SFR-$L_{\rm [CII]}$ relation,

$$\log\left(\frac{L_{\rm [CII]}}{L_\odot}\right) = A\ \log({\rm SFR}) + B + \sigma_{\rm L}, \quad (22)$$

we can write,

$$\bar{I}_{\rm [CII]} = 10^B \int \frac{{\rm d}n}{{\rm d}\log({\rm SFR})} 10^{(\sigma_{\rm L}^2/2)} \frac{{\rm SFR}^A}{4\pi D_L^2}\, y_{\rm [CII]} D_A^2\, {\rm d}\log({\rm SFR}), \quad (23)$$

where the factor $10^{(\sigma_{\rm L}^2/2)}$ comes from the log-normal form of the SFR-to-$L_{\rm [CII]}$ relation and which implies that,

$$\bar{L}_{\rm [CII]} = {\rm med}(L_{\rm [CII]}) \times 10^{(\sigma_{\rm L}^2/2)}, \quad (24)$$

where ${\rm med}(L_{\rm [CII]})$ is the median value of $L_{\rm [CII]}$. Given that $A \sim 1$, a valid assumption within the SFR ranges that contribute the most to the SFRD (see horizontal lines in Fig. 4), it comes from Eq. (23) that the mean [CII] intensity is proportional to $\int \frac{{\rm d}n}{{\rm d}\log({\rm SFR})} {\rm SFR}\ {\rm d}\log({\rm SFR})$, that is, the cosmic SFRD. This explains the discrepancies between the rTNG and AM models that share the same SFR-to-$L_{\rm [CII]}$ relation: the factor of two in

$\bar{I}_{[CII]}$ at $z = 3.7$, 4.3, and 5.8 and the factor of three at $z = 7.4$ can be tracked back to SFRD differences between these two models (see Fig. 3).

Similarly, discrepancies in $\bar{I}_{[CII]}$ predicted from models based on the same halo-to-galaxy SFR but different SFR-to-$L_{[CII]}$ relations can be understood in light of Eqs. (22) and (23). Assuming again, that $A \sim 1$, we can define two distinct sets of mean SFR-to-$L_{[CII]}$ relations, based on their B value. This way, we have an optimistic set that corresponds to $B \approx 6.9$ of the V15 relation and a pessimistic one that corresponds to $B = 6.4$ of the A20 relation. L18 relation, due to its redshift evolution, belongs to the optimistic set at $z = 3.7$ and 4.3 and the pessimistic set at $z = 5.8$ and 7.4. As a result, mean [CII] line intensities predictions from V15 models are optimistic, whereas predictions from the A20 models are pessimistic through the whole redshift range. Predictions of L18 models are close to the ones of V15 at $z = 3.7$ and $z = 4.3$ and approach the forecasts of A20 models at higher redshifts.

We also tested the influence of $3 \times 10^9 - 10^{10}\ M_\odot$ halos on the forecasted $\bar{I}_{[CII]}$ of the two techniques. For our AM approach, we repeated the procedure with a lower halo mass limit of $3 \times 10^9\ M_\odot$. We find that the contribution of low mass halos is only significant for the L18 relation, as it is the only one that predicts bright [CII] luminosities for low SF galaxies (SFR $< 1\ M_\odot\,\mathrm{yr}^{-1}$; Fig. 4). However, even in this case, the mean [CII] intensity predicted by the AM method only increases by a factor 1.1 and 1.5 at $z = 5.8$ and $z = 7$, respectively (Fig. 6). To test the influence of $3 \times 10^9 - 10^{10}\ M_\odot$ halos for our rTNG approach, we calculated their mean [CII] intensity within the high-resolution TNG100-1 simulation at the central redshift of our FYST spectral window (Fig. 6). Again, we find that the contribution of these low mass halos is only significant in the case of the L18 relation, with only an increase of the mean [CII] intensity by a factor 1.3 and 2.5 at $z = 5.8$ and $z = 7$, respectively. A difference is notable only in the two higher-redshift tomographic scans because at higher redshifts, the contribution to the global SFRD of the low-SFR galaxies (SFR $< 1\ M_\odot\,\mathrm{yr}^{-1}$) hosted mainly in low-mass DM halos ($M_\mathrm{h} < 10\ M_\odot$) is greater (the trend is visible in Fig. 4).

In Fig. 6, we also compare our results to those from Yue et al. (2015) and Chung et al. (2020). Yue et al. (2015) use the Bouwens et al. (2015) UV luminosity function to perform AM and the V15 SFR-to-$L_{[CII]}$ relation. Their results are thus naturally in excellent agreement with our AM-V15 predictions. Chung et al. (2020) use instead the UNIVERSE Machine forward modeling in combination with the L18 relation. At all redshift, their results systematically agree with our most pessimistic predictions. This is true even at low redshift, where L18 corresponds to the most optimistic SFR-to-$L_{[CII]}$ relation.

Although the [CII] LIM foreground contamination is out of the scope of this paper, we expect that the subtraction of the smooth, IR continuum foreground will largely suppress the [CII] mean intensity, leaving only the intensity fluctuations around the mean (Breysse et al. 2017). It is for this reason, that we do not consider the possibility of a direct mean intensity measurement.

3.2. The three-dimensional power spectrum of the [CII] line

In this section, we use the three-dimensional spherically-averaged power PS to measure the spatial fluctuations in our [CII] tomographic scans and characterize their dependencies with respect to the underlining halo-to-galaxy SFR and the SFR-to-$L_{[CII]}$ relation. We demonstrate in particular how such measurements, which represent the spatial distribution of galaxies weighted by their luminosities, can be used to statistically constrain the halo-to-galaxy SFR and the SFR-to-$L_{[CII]}$ relation without the help of any auxiliary data.

3.2.1. Forecasts

To calculate the three-dimensional spherically-averaged PS, we converted our tomographic scans from the angular-frequency space to the three-dimensional comoving space and from there to the Fourier space by computing their Fourier transform. The minimum and maximum scales of the PS accessible to our analysis naturally depends on the "observing" properties of our tomographic scans. For example, the largest physical scale along the line-of-sight (i.e., $r_{\parallel,\mathrm{max}}$) is defined using the highest and lowest redshifts (i.e., z_max and z_min, respectively) probed by our spectrometer, whereas the smallest scale along the line-of-sight (i.e., $r_{\parallel,\mathrm{min}}$) is defined by the redshift of two consecutive channels ($z_\mathrm{chn,i}$ and $z_\mathrm{chn,i+1}$), that is,

$$r_{\parallel,\mathrm{max}} = \frac{c}{H_0} \int_{z_\mathrm{min}}^{z_\mathrm{max}} \frac{\mathrm{d}z}{\sqrt{\Omega_\mathrm{m}(1+z)^3 + \Omega_\Lambda}}, \tag{25}$$

$$r_{\parallel,\mathrm{min}} = \frac{c}{H_0} \int_{z_\mathrm{chn,i}}^{z_\mathrm{chn,i+1}} \frac{\mathrm{d}z}{\sqrt{\Omega_\mathrm{m}(1+z)^3 + \Omega_\Lambda}}, \tag{26}$$

where c is the speed of light. In the plane of the sky, the largest and smallest scales (i.e., $r_{\perp,\mathrm{max}}$ and $r_{\perp,\mathrm{min}}$, respectively) probed by our tomographic scans are instead given by,

$$r_{\perp,\mathrm{max}} = D_A(z_\mathrm{cen})\ \Delta\theta_S, \tag{27}$$

$$r_{\perp,\mathrm{min}} = D_\mathrm{A}(z_\mathrm{cen})\ \Delta\theta_\mathrm{b}, \tag{28}$$

where $D_\mathrm{A}(z_\mathrm{cen})$ is the comoving angular distance to the central redshift of our tomographic scans (i.e., z_cen), $\Delta\theta_S$ is the solid angle covered by our survey in radians, and $\Delta\theta_\mathrm{b}$ is the FWHM of our telescope beam also in radians. Moving to the Fourier space, the largest and smallest scales in the comoving coordinates (from now on, represented by wavenumbers k in units of Mpc^{-1}; $k_\parallel$ and $k_\perp$ for the line-of-sight and sky plane scales respectively) become,

$$k_\mathrm{min} = \frac{2\pi}{r_\mathrm{max}}, \tag{29}$$

$$k_\mathrm{max} = \frac{2\pi}{2r_\mathrm{min}}. \tag{30}$$

For the LIM FYST survey, this translates in $k_\parallel \in [10^{-3}\,\mathrm{Mpc}^{-1}, 10^{-1}\,\mathrm{Mpc}^{-1}]$ and $k_\perp \in [10^{-2}\,\mathrm{Mpc}^{-1}, 2\,\mathrm{Mpc}^{-1}]$ for all our tomographic scans. The scales $k \in [10^{-2}\,\mathrm{Mpc}^{-1}, 10^{-1}\,\mathrm{Mpc}^{-1}]$ are thus available in three dimensions, whereas $k \in [10^{-1}\,\mathrm{Mpc}^{-1}, 2\,\mathrm{Mpc}^{-1}]$ are only available in two dimensions. The importance of this three to two dimensions transition for our sensitivity estimates is discussed in Sect. 3.2.3.

Having defined the limits of the Fourier space accessible by our tomographic scans, their spherically-averaged PS is given by

$$P(k) = \frac{\langle \tilde{I}^2_{[CII]}(k) \rangle}{2\pi^2 V_\mathrm{box}}, \tag{31}$$

where $\tilde{I}_{[CII]}(k)$ is the Fourier transform of these [CII] tomographic scans and $V_\mathrm{box} = r^2_{\perp,\mathrm{max}} \times r_{\parallel,\mathrm{max}}$ is their volume in comoving units. We performed this calculation using a Fast Fourier Transform algorithm, following Jeong (2010).

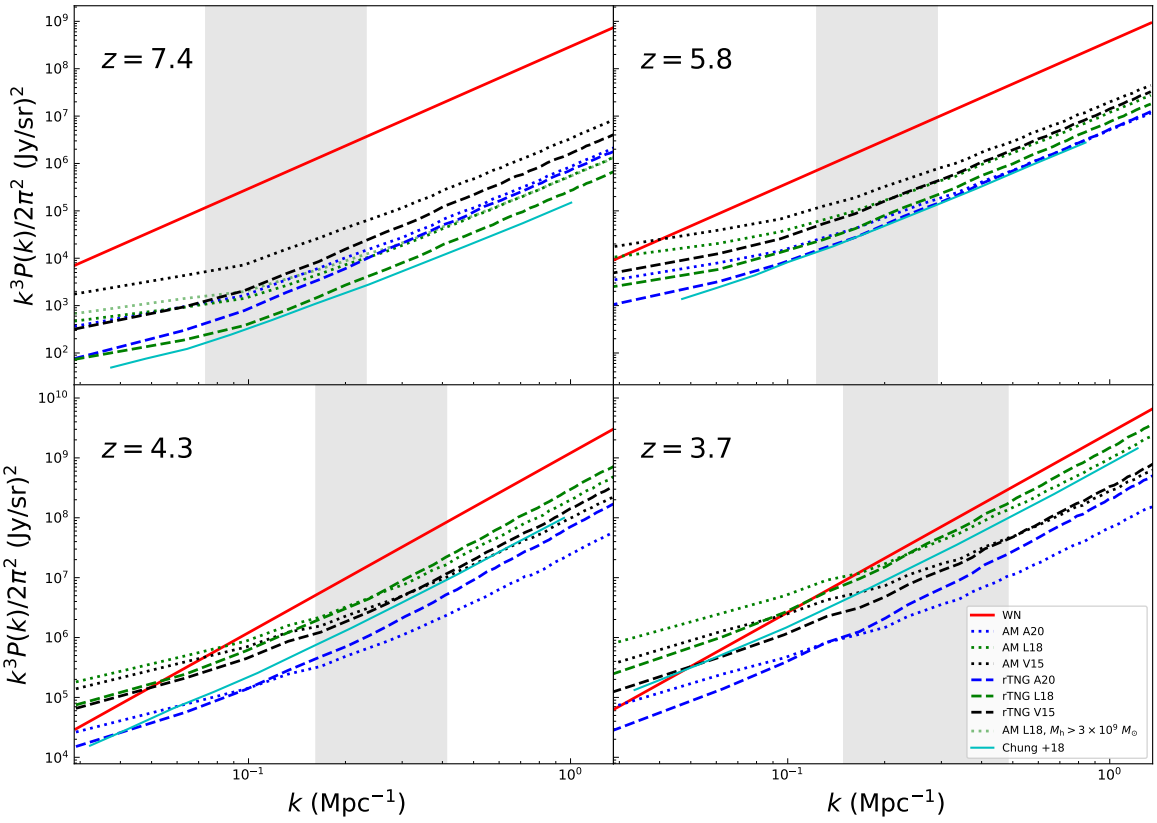

Fig. 7. Spherically averaged PS for a $4° \times 4°$ [CII] mock survey subdivided in four tomographic scans of 40 GHz bandwidth each centered at $z = 3.7$, 4.3, 5.8, and 7.4. The averaging takes place in the Fourier space in k-bins of $\Delta k = 0.034\,\mathrm{Mpc}^{-1}$. Predictions from our rTNG and AM models are shown by dashed and dotted lines, respectively. Lines are color-coded according to the used SFR-to-$L_{[\mathrm{CII}]}$ relation, blue lines for A20, green lines for L18, and black lines for V15. L18 is also plotted at $z = 7.4$ including the contribution of 3×10^9–$10^{10}\,M_\odot$ halos for our AM model (faint green dotted line). The red lines are the power spectrum of the instrumental single-k-mode white noise (labeled as WN), P_{WN}, of the scheduled FYST LIM survey. Gray areas cover the scales at which $P^{\mathrm{clust}}_{[\mathrm{CII}]} \sim P^{\mathrm{shot}}_{[\mathrm{CII}]}$ for our various models. This illustrates the transition from clustering-dominated to shot noise-dominated scales. Predictions from Chung et al. (2020, turquoise line) are also shown for comparison.

Figure 7 presents the PS of all the versions of mock [CII] tomographic scans as $k^3P_{[\mathrm{CII}]}/(2\pi^2)$, in units of $(\mathrm{Jy/sr})^2$. All models exhibit the same $\propto k^3$ linear trend at $k > 0.3\,\mathrm{Mpc}^{-1}$ but gradually deviate upward at $k \sim 0.1$–$0.3\,\mathrm{Mpc}^{-1}$, with this deviation taking place at progressively smaller k as we move to higher redshifts. Despite these similarities, at a given redshift, there is up to two orders of magnitude offset between predictions from different models. Forecasts based on the same SFR-to-$L_{[\mathrm{CII}]}$ relation but different halo-to-galaxy SFR relation differ by a factor 1–3 at $k > 0.2\,\mathrm{Mpc}^{-1}$ and 2–6 at $k < 0.2\,\mathrm{Mpc}^{-1}$, without any systematic evolution of these offsets with redshift. For example, the rTNG models yield more optimistic values for $k > 0.2\,\mathrm{Mpc}^{-1}$ at $z = 3.7$ and 4.3, while for the remaining redshifts and scales, the AM models produce systematically higher values. An important difference between the rTNG and AM models is that the deviation from the $\propto k^3$ linear trend is always more significant in the case of the AM models.

Models that are based on the same halo-to-galaxy SFR but different SFR-to-$L_{[\mathrm{CII}]}$ relations also exhibit differences: across all redshifts, V15 combined with rTNG (AM) yields a factor of two (four) higher PS than A20 at $k > 0.2\,\mathrm{Mpc}^{-1}$ and four (five) at $k < 0.2\,\mathrm{Mpc}^{-1}$; L18, the only relation with a significant redshift evolution goes from being four and two times higher than V15 at $k > 0.2\,\mathrm{Mpc}^{-1}$ and $k < 0.2\,\mathrm{Mpc}^{-1}$) at $z = 3.7$, respectively, to four and six times lower than V15 at $k > 0.2\,\mathrm{Mpc}^{-1}$ and $k < 0.2\,\mathrm{Mpc}^{-1}$ at $z = 7.4$ (for both rTNG and AM).

As for the mean [CII] intensity, we repeated our AM calculation using a lower DM halo mass limit of $3 \times 10^9\,M_\odot$. We found that the contribution of low mass halos to the [CII] PS is only significant for the L18 relation at $z = 7.4$, with an increase of the PS by a factor 1.6 at $k_{\mathrm{min}} \approx 10^{-2}\,\mathrm{Mpc}^{-1}$ (Fig. 7). As described in the next paragraph, this value agrees with the square of the $\times 1.3$ amplification of the mean [CII] intensity due to these low mass DM halos and inferred in Sect. 3.1. Unfortunately, we cannot simply calculate the contribution of 3×10^9–$10^{10}\,M_\odot$ halos to the [CII] PS predicted from our rTNG models because the high-resolution TNG100-1 simulation does not probe the necessary large volumes. Nevertheless, we can infer from our mean [CII] intensity analysis that their contribution should be significant for L18 at $z = 5.8$ and $z = 7.4$, with an increase of the PS signal at low k by a factor $1.3^2 = 1.69$ and $2.5^2 = 6.25$, respectively. These increases would put our rTNG predictions at roughly the same levels as those from our AM approach.

To better understand the dependencies of the PS on the halo-to-galaxy SFR relation and SFR-to-$L_{[\mathrm{CII}]}$ relation, we study the analytical form of its components. One of these component is the so-called Poissonian shot noise ($P^{\mathrm{shot}}_{[\mathrm{CII}]}$) arising from the discrete nature of galaxies. Following Uzgil et al. (2014), the analytical form of $P^{\mathrm{shot}}_{[\mathrm{CII}]}$ can be written as

$$P^{\mathrm{shot}}_{[\mathrm{CII}]} = \int \frac{\mathrm{d}n}{\mathrm{d}\log L_{[\mathrm{CII}]}} \left(\frac{L_{[\mathrm{CII}]}}{4\pi D_L^2} y_{[\mathrm{CII}]} D_A^2 \right)^2 \mathrm{d}\log L_{[\mathrm{CII}]}, \tag{32}$$

which, assuming a simple form for the SFR-to-$L_{[CII]}$ relation (Eq. (22)), yields

$$P^{\rm shot}_{[CII]} = 10^{2B} \int \frac{{\rm d}n}{{\rm d}\log({\rm SFR})} \left(\frac{{\rm SFR}^A 10^{\sigma_{\rm L}^2/2}}{4\pi D_L^2} y_{[CII]} D_A^2 \right)^2 {\rm d}\log({\rm SFR}). \quad (33)$$

Shot noise is by definition a scale-independent effect and as a result $P^{\rm shot}_{[CII]}$ is not a function of k. In units of $({\rm Jy/sr})^2$, this corresponds to the $\propto k^3$ linear trend observed at $k > 0.2\,{\rm Mpc}^{-1}$ for all models and all redshifts in Fig. 7. In addition, the fact that $P^{\rm shot}_{[CII]}$ is proportional to ${\rm SFR}^2$ rather than SFR (assuming $A \approx 1$) explains why the rTNG models yield higher PS than AM models at $k > 0.2\,{\rm Mpc}^{-1}$ at $z = 3.7$ and 4.3, despite having significantly lower SFRD (Fig. 3). Indeed, this ${\rm SFR}^2$ dependency renders the shot noise very sensitive to galaxies with high SFRs (i.e., galaxies with ${\rm SFR} > 1\,M_\odot\,{\rm yr}^{-1}$) and which are more abundant in the rTNG models than in our AM models.

The second component of the PS is the so-called clustering signal component arising from the fact that galaxies follow the dark matter density field. Following again Uzgil et al. (2014), this component is analytically given by,

$$\begin{aligned} P^{\rm clust}_{[CII]}(k) &= \bar{I}^2_{[CII]} \bar{b}^2_{[CII]} P_{\delta\delta}(k) \\ &= \left(\int \frac{{\rm d}n}{{\rm d}\log L_{[CII]}} \frac{L_{[CII]}}{4\pi D_L^2} y_{[CII]} D_A^2 {\rm d}\log L_{[CII]} \right)^2 \bar{b}^2_{[CII]} P_{\delta\delta}(k), \quad (34) \end{aligned}$$

which, using Eq. (22), yields

$$\begin{aligned} P^{\rm clust}_{[CII]}(k) &= \bar{b}^2_{[CII]} P_{\delta\delta}(k) \\ &\times 10^{2B} \left(\int \frac{{\rm d}n}{{\rm d}\log({\rm SFR})} \frac{10^{\sigma_{\rm L}^2/2} {\rm SFR}^A}{4\pi D_L^2} y_{[CII]} D_A^2 {\rm d}\log({\rm SFR}) \right)^2 \quad (35) \end{aligned}$$

where $P_{\delta\delta}(k)$ is the PS of the nonlinear matter and $\bar{b}_{[CII]}$ is the average galaxy bias weighted by [CII] luminosity of galaxies. $P_{\delta\delta}(k)$ peaks at a scale that is well constrained by observational cosmology, that is, $k_{\rm eq} = 0.01034 \pm 0.00006\,{\rm Mpc}^{-1}$, and that is set by the Hubble scale at the matter-radiation equality which occurs at $z_{\rm eq} = 3387 \pm 21$ (Planck Collaboration I 2020). As a result, $P^{\rm clust}_{[CII]}$, contrary to $P^{\rm shot}_{[CII]}$, is a function of k and peaks at $k \sim 10^{-2}\,{\rm Mpc}^{-1}$.

Given that $A \sim 1$, $\bar{b}_{[CII]} \sim 1$ and $P_{\delta\delta}(k) \sim 1$ at $k \sim 10^{-2}\,{\rm Mpc}^{-1}$, one understands by comparing Eqs. (35) and (33) that the halo-to-galaxy SFR relation controls how much the $k^3 P(k)/(2\pi^2)$ signal deviates at $k < 0.2\,{\rm Mpc}^{-1}$ from the $\propto k^3$ linear trend. Consequently, the fact that the rTNG models have at all redshifts a large fraction of their SFRD produced by ${\rm SFR} > 1\,M_\odot\,{\rm yr}^{-1}$ galaxies naturally implies lower $P^{\rm clust}_{[CII]}$-to-$P^{\rm shot}_{[CII]}$ ratios than in the case of AM models.

In short, the different influence of the two steps on the large scales comes from the fact that while the halo-to-galaxy SFR models deviate more significantly at low SFRs (Fig. 1), the SFR-to-$L_{[CII]}$ relations are close to parallel in logarithmic scale (Fig. 4). Consequently, these differences at low SFRs affect more the amplitude of the clustering signal component ($P^{\rm clust}_{[CII]} \sim {\rm SFR}$) than the shot noise component ($P^{\rm shot}_{[CII]} \sim {\rm SFR}^2$). The $P^{\rm clust}_{[CII]}$-to-$P^{\rm shot}_{[CII]}$ ratio is in that respect an important observational tool to constrain the halo-to-galaxy SFR relation without being too sensitive to the exact form of the SFR-to-$L_{[CII]}$ relation.

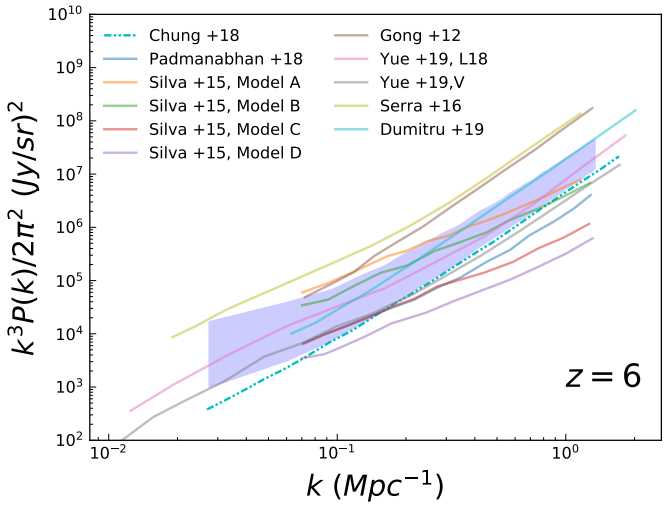

Fig. 8. A compilation of $z = 6$ [CII] power spectrum predictions from the literature, compared to the range forecasted by our models (shaded area).

3.2.2. Comparison to previous work

Despite the large diversity of models tested here, we could not reproduce the more than two orders of magnitude difference between the most optimistic and pessimistic $P_{[CII]}$ forecasts found in the literature (e.g., see Fig. 8 for $z = 5.8$). To investigate the origin of these discrepancies, we examine each case closely, focusing on how their different assumptions influence their forecast.

Gong et al. (2012) do not model the SFR of high-redshift galaxies to predict their $L_{[CII]}$, but instead base their $P_{[CII]}$ predictions on the average number density of [CII] ions and temperature of the dense high-redshift ISM. This approach is independent of any high-redshift SFRD assumption, but it is highly dependent on the very uncertain fraction of the ISM gas residing in dense clumps. This very different approach yields one order of magnitude higher $P_{[CII]}$ values than our most optimistic model.

Silva et al. (2015) combine a $M_{\rm h}$-to-SFR relation from semi-analytic models with four different empirically calibrated SFR-to-$L_{[CII]}$ relations with no scatter (label model A, B, C, and D in Fig. 8). Changes in the zero points of these four SFR-to-$L_{[CII]}$ relations drive most of the offset observed between their models. Two of their models are well in the range of our predictions, but two of them predict much lower PS than ours. A significant difference between Silva et al. (2015) and all models presented in Fig. 8 is their very shallow slope at $k > 0.1\,{\rm Mpc}^{-1}$. This is due to a combination of a strong clustering signal and a weak shot noise signal, explained respectively, by a slight overestimation of the SFRD at $z \sim 6$ (see Fig. 3) and by a flat $M_{\rm h}$-SFR relation at $M_{\rm h} > 10^{11.5}\,M_\odot$.

Serra et al. (2016) base their predictions on an analytic halo model combined with measurements of the cosmic infrared background (CIB). They convert $L_{\rm IR}$ into $L_{[CII]}$ using empirical relation from $z < 4$ galaxies. They initially produced two sets of results: one from the *Planck* and one from the *Herschel* CIB measurements, their final result being the average of the two sets. The fact that the high-redshift SFRD inferred by Planck Collaboration XXX (2014) is one order of magnitude higher than that of Madau & Dickinson (2014, see Fig. 3), results in a strong clustering signal prediction. Combined with a strong shot noise signal due to the high SFR of galaxies hosted

in DM halos of $M_h > 10^{11}\,M_\odot$, their result is the most optimistic in our compilation, 0.5 dex higher than our most optimistic model at $k > 0.1\,\mathrm{Mpc}^{-1}$. Using only the *Herschel* CIB measurements, which are compatible with the Madau & Dickinson (2014) SFRD, would result in one order of magnitude lower forecast well within the range of our predictions.

Chung et al. (2020) use the UNIVERSE Machine (Behroozi et al. 2019) to create a $2° \times 2°$ cone populated with SF galaxies which they translate into mock tomographic scans by adopting the SFR-to-$L_{[CII]}$ relation of L18 with a scatter of 0.5 dex. The UNIVERSE Machine prediction for the SFRD at $z > 4$ is half of the Madau & Dickinson (2014, see Fig. 3), whereas the SFR hosted in DM halos of $M_h > 10^{11}\,M_\odot$ is close to our rTNG models (Behroozi et al. 2019). The result is a strong shot noise component combined with a weak clustering signal ($k_{tr} \approx 0.1$–$0.2\,\mathrm{Mpc}^{-1}$, close to the k_{tr} of our rTNG L18 model).

Dumitru et al. (2019) assume that $\mathrm{SFR} \propto M_h$ and calibrate their model with the cosmic SFRD of Madau & Dickinson (2014). They use the SFR-to-$L_{[CII]}$ relation of L18 without considering any scatter. The fact that they adopt a linear SFR-M_h relation results in a $P_{[CII]}$ dominated by its shot noise component, which is well within our prediction range. Yue & Ferrara (2019) use an analytical halo model calibrated with the SFRD of Bouwens et al. (2015) combined with several SFR-to-$L_{[CII]}$ relations. Here we present their forecast based on V15 with a 0.4 dex scatter and L18 with a 0.6 dex scatter. Their $P_{[CII]}$ predictions are in good agreement with ours. They adopt the M_h-SFR relation derived from Yue et al. (2015) using AM, resulting in a PS shape similar to our AM models.

Padmanabhan (2019) combine empirical constraints on the local [CII] line luminosity function with the redshift evolution of the SFRD of Madau & Dickinson (2014), as well as with the [CII] intensity mapping measurement of Pullen et al. (2018). Their SFR-to-$L_{[CII]}$ relation is quite different from the rest of the models presented in Fig. 8, forecasting weak [CII] emission from the low SFR galaxies ($\mathrm{SFR} < 1\,M_\odot\,\mathrm{yr}^{-1}$) and making their prediction the most conservative for $z = 6$, with the exception of two models of Silva et al. (2015).

The above comparisons reinforce the conclusion of the previous section. The magnitude of the shot noise component is mostly sensitive to the choice of the SFR-to-$L_{[CII]}$ relation and at a lower level to the shape of the M_h-SFR relation for $M_h > 10^{11}\,M_\odot$. On the contrary, the magnitude of the clustering component is mostly sensitive to the cosmic SFRD and at a lower level to the choice of the SFR-to-$L_{[CII]}$ relation. The differences between all these forecasts can thus be always traced back to different assumptions on the cosmic SFRD (Serra et al. 2016), the massive end of the M_h-SFR relation (Silva et al. 2015; Dumitru et al. 2019), or the SFR-to-$L_{[CII]}$ relation (Padmanabhan 2019). In the light of the latest observations and simulations, some of these assumptions are outdated or unrealistic. Excluding the Gong et al. (2012) and Serra et al. (2016) models because they significantly overestimate the observed SFRD of Madau & Dickinson (2014) and the Silva et al. (2015) models because they significantly underestimate the SFR hosted in $M_h > 10^{11.5}\,M_\odot$ halos (compared to the latest work on halo-galaxy relation, e.g., Behroozi et al. 2019), we end up with PS predictions from the literature consistent with the range observed in our models. This one order of magnitude differences emphasizes the need for more detailed modeling of the star formation and ISM condition of high-redshift galaxies, which should come hand-in-hand with the upcoming LIM observations.

3.2.3. Sensitivity estimation

The signal-to-noise (S/N) achieved when measuring the PS from LIM observations is a combination of three effects: (i) the instrumental white noise, (ii) the sample variance within each k-bin, and (iii) the attenuation of the PS signal due to smoothing by the instrumental beam. Based on our $P_{[CII]}$ forecasts, we calculate the S/N for the case of Prime-Cam (Vavagiakis et al. 2018), that is, we assume a telescope diameter of 6 m, a number of detectors of $N_{beams} = 1004$, a total bandwidth per spectrometer of $\Delta\nu = 40\,\mathrm{GHz}$, a survey covering a $4° \times 4°$ sky region consisting of $t_{surv} = 4000$ hours. Here, we do not consider the atmospheric and astronomical foregrounds–methods for the mitigation of which will be investigated in Karoumpis et al. (in prep.)

Using on-sky noise equivalent intensities, σ_{vox}, of 0.7, 0.86, 1.7, and $2.8\,\mathrm{MJy\,sr^{-1}\,s^{1/2}}$ at 225, 280, 350, and 410 GHz (CCAT-Prime Collaboration 2021) and assuming a homogeneously covered survey, the instrumental white noise can be expressed as,

$$P_{WN} = \frac{\sigma_{vox}^2}{t_{vox}} V_{vox}, \tag{36}$$

where V_{vox} is the comoving volume covered by a voxel and t_{vox} is the on-sky integration time of this voxel, which is related to the total observing time of our survey (i.e., t_{surv}) by,

$$t_{surv} = \frac{\text{Number of voxels of the tomography}}{\text{Number of pixels of the detector}} \times t_{vox}, \tag{37}$$

as the four spectral windows of Prime-Cam are observed simultaneously but only one channel at a time (with the spectral coverage being achieved by adjusting one step at a time the Fabry-Perot spacing). Each tomography has a different number of voxels, which depends on the angular and spectral resolution of the individual spectral window (see Sect. 3.1).

The instrumental white noise is then combined with the predicted PS in order to estimate the statistical uncertainty induced by the finite number of Fourier modes averaged in every k-bin,

$$\sigma_{P(k)} = \frac{P_{[CII]}(k) + P_{WN}}{\sqrt{N_m(k)}}, \tag{38}$$

where $N_m(k)$ is the number of measured modes within a k-bin centered at k. As discussed in Chung et al. (2020), $N_m(k)$ is given by,

$$N_m(k) = \frac{\min(k, k_{\parallel,max})\; k\; \Delta k\; V_{surv}}{4\pi^2}, \tag{39}$$

where the term $\min(k, k_{\parallel,max})$ accounts for the fact that $k_{\parallel,max}$ is an order of magnitude smaller than $k_{\perp,max}$, which implies that k-bins greater than $k_{\parallel,max}$ have their three-dimensional sphere truncated at $k_\parallel > k_{\parallel,max}$. We note that neglecting the effect of this three to two dimensions transition would result in an overestimation of the S/N at large k.

Finally, following Li et al. (2016), we account in the calculation of the S/N for the attenuation of the PS signal caused by the smoothing of the intensity map by the instrumental beam. This is done using a modification of the attenuation factor $W = P(k)/P_{SM}(k)$ (Li et al. 2016), $P_{SM}(k)$ being the PS of the smoothed map. For the case of asymmetrical voxels, it comes that,

$$W(k) = e^{-k^2\sigma_\perp^2} \int_0^1 e^{-\min(\mu k, k_{\parallel,max})^2 \left(\sigma_\parallel^2 - \sigma_\perp^2\right)} \mathrm{d}\mu, \tag{40}$$

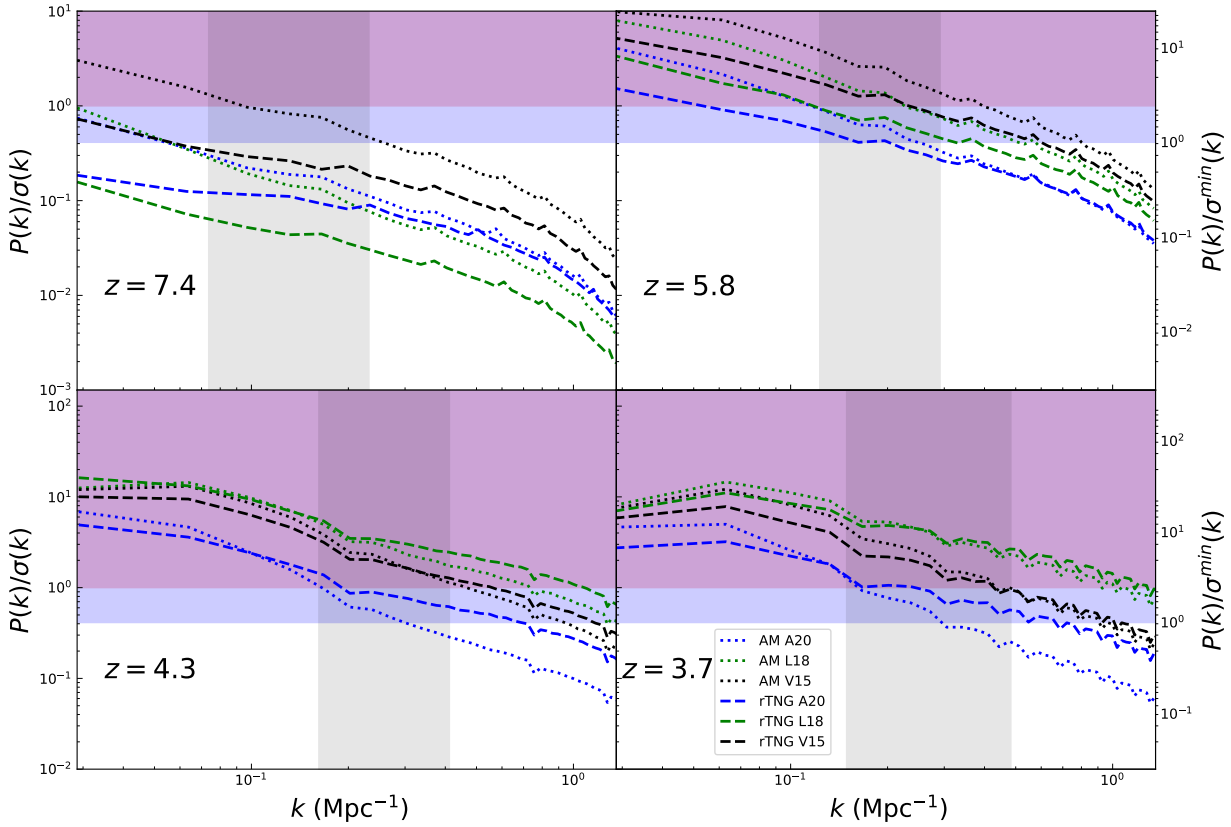

Fig. 9. S/N for a 4° × 4° FYST [CII] LIM mock survey of $t_{\rm surv}$ = 4000 hours. It consists of four tomographic scans of 40 GHz bandwidth each centered at z = 3.7, 4.3, 5.8, and 7.4. The S/N combines three effects: the instrumental white noise, the sample variance within each k-bin, and the attenuation due to smoothing by the instrumental beam. Lines are color-coded according to the used SFR-to-$L_{\rm [CII]}$ relation, blue lines for A20, green lines for L18, and black lines for V15. The magenta painted area represents the $S/N > 1$ values for the minimum Δk considered ($\Delta k = 0.034\,{\rm Mpc}^{-1}$, main y-axis), whereas the purple painted area denotes the $S/N > 1$ values for the maximum Δk considered ($\Delta k = 0.34\,{\rm Mpc}^{-1}$, secondary y-axis). Gray areas cover all k values for which $P^{\rm clust}_{\rm [CII]} = P^{\rm shot}_{\rm [CII]}$ as indicators for the transition scale between the clustering dominated to the shot noise dominated scales.

with,

$$\sigma_{\parallel} = \frac{c}{H(z)} \frac{\Delta\nu_{\rm b}\,(1+z)}{2.355\,\nu_{\rm obs}} \tag{41}$$

and,

$$\sigma_{\perp} = \frac{D_{\rm A}(z)\,\Delta\theta_{\rm b}}{2.355} \tag{42}$$

where $\Delta\nu_{\rm b}$ and $\Delta\theta_{\rm b}$ are the FWHM of the angular and spectral beams, respectively.

Bringing together the three effects driving the noise, the instrumental white noise, sample variance, and resolution limits, the S/N can be written as,

$$S/N = W(k)\,\sqrt{N_{\rm m}(k)}\,\frac{P_{\rm [CII]}(k,z)}{P_{\rm [CII]}(k,z) + P_{\rm N}}. \tag{43}$$

The S/N achieved by the FYST LIM survey using a k-bin of $\Delta k = 0.034\,{\rm Mpc}^{-1}$ (i.e., the finest k-space resolution of the survey) are shown in Fig. 9. For all models, the achieved S/N decreases significantly with increasing k. The offsets in S/N between these models are to first order the same than those observed between their predicted PS (Fig. 7). The only exception is at $k < 0.06\,{\rm Mpc}^{-1}$ for z = 3.7 and 4.3, where most models predict $P_{\rm [CII]} > P_{\rm WN}$ and thus have S/N which converge toward $\sqrt{N_{\rm m}(k)}$.

At $k < 0.2\,{\rm Mpc}^{-1}$, the fall in S/N is caused by the increase of the $P_{\rm WN}$-to-$P_{\rm [CII]}$ ratio with increasing k (see Eq. (43) and Fig. 7). Then, at $k > 0.2\,{\rm Mpc}^{-1}$, the $P_{\rm WN}$-to-$P_{\rm [CII]}$ ratio remains constant but the attenuation factor $W(k)$–accounting for the influence of the beam–becomes significant, steepening further the fall of the S/N. We note also that the restricted spectral resolution of the Prime-Cam influences the growth of $N(k)$. At $k > k_{\parallel,\rm max}$, the line-of-sight modes become indeed unavailable, which causes a discontinuity in the slope of the S/N at $k \sim 0.2\,{\rm Mpc}^{-1}$.

Finally, we observe periodic jumps in S/N (or in the case of z = 3.7 and 4.3 periodic dips) with a different period at different redshift. Those are explained by periodic jumps in the number of Fourier modes averaged in a given k-bin. Indeed, because our voxels have a cuboid shape, a shell of pixels whose distances are $k \pm \Delta k/2$ from the center of the tomography, is only an approximation of a spherical shell. For example, when averaging over k-bins of $\Delta k = 0.034\,{\rm Mpc}^{-1}$, the width of the shells oscillates between three and four pixels at 225 and 280 GHz and between two and three pixels at 350 and 410 GHz, respectively.

The FYST LIM survey will be optimal for constraining at high k-resolution the clustering component of the [CII] PS. Indeed, at the scales where this component dominates (i.e., $k < 0.2\,{\rm Mpc}^{-1}$), even our most pessimistic models yields clear $S/N > 1$ detection at all redshifts but z = 7.4. The detection at such high k-resolution of the [CII] PS at scales where the shot noise component dominates (i.e., $k \gg 0.2\,{\rm Mpc}^{-1}$) will be most challenging for the FYST LIM survey, with only two models

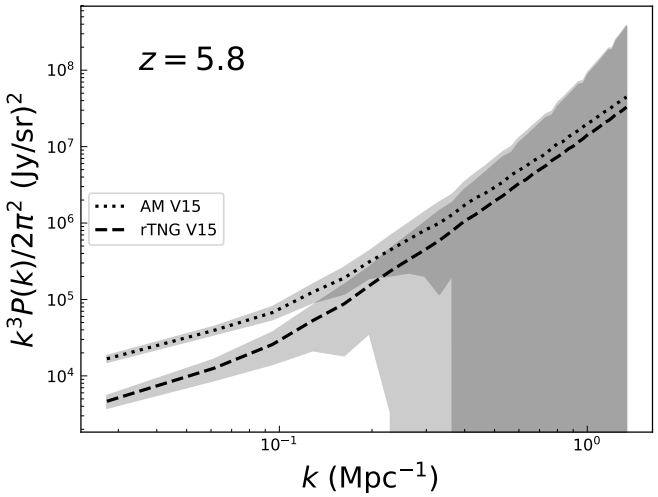

Fig. 10. [CII] PS at $z = 5.8$ for our AM and rTNG models combined with the SFR-to-$L_{[CII]}$ relation of V15. Results are the same as in Fig. 7 but this time is plotted with the uncertainties coming from the S/N of Fig. 9 for $\Delta k = 0.034\,\mathrm{Mpc}^{-1}$. The plot serves as an example of the potential of FYST to trace the [CII] PS from the EoR on large scales constraining the halo-to-galaxy SFR relation.

detected at $z = 3.7$, four at $z = 4.3$, one at $z = 5.8$, and none at $z = 7.4$. This component, which is invariant with k, can, however, be fully constrained using only two measurements made at sufficient k leverage. Finally, at $z = 7.4$, the FYST LIM survey will only detect the clustering component of the [CII] PS in the case of our most optimistic model.

In order to increase the probability of detecting the [CII] PS at high redshifts and large k, it is conceivable to increase the value of Δk by up to an order of magnitude, amplifying the S/N by a factor of $\sqrt{10}$ (see right-hand y-axis of Fig. 9). This re-binning would result in three data points for each measured PS: one at scales where the clustering component dominates (all models detected at $z = 3.7$, 4.3 and 5.8; four models at $z = 7$), one at intermediate scales (all models detected at $z = 3.7$, 4.3 and 5.8; one model at $z = 7.4$), and one at scales where the shot-noise component dominates (five models detected at $z = 3.7$ and 4.3; three at $z = 5.8$; none at $z = 7$).

4. Discussion

Our study unambiguously demonstrates that the latest physically- or empirically-motivated models describing the halo-to-galaxy SFR relation and the SFR-to-$L_{[CII]}$ relation at the (post-)EoR yield [CII] LIM predictions spanning a range of one order of magnitude. Such large uncertainties pose, naturally, a challenge for designing [CII] LIM experiments, as those must be tailored to allow for the detection of even the most pessimistic yet realistic model. On the other hand, these variations also demonstrate the power of future [CII] LIM measurements to restrict the range of possible early galaxy evolution models. In particular, by detecting the [CII] PS at low- and high-spatial scales LIM experiments can put stringent constraints on the yet very uncertain redshift evolution of the SFRD, the SFR-to-$L_{[CII]}$ relation during the (post-)EoR as well as shed light on the halo-to-galaxy SFR relation (Fig. 10).

In this context, FYST will certainly unravel unknown aspects of early galaxy evolution. The observations of FYST will constrain the cosmic SFRD up to $z \sim 7$, a key parameter for modeling the evolution of galaxies over the critical first gigayears of the Universe, the current knowledge of which is hampered by observational limitations. Even though galaxy surveys performed by ALMA and JWST will also attempt to measure the redshift evolution of the SFRD at the (post-)EoR, their optical design is optimal for deep, "pencil-beam" galaxy surveys (e.g., the field of view is ∼20 arcsec for ALMA and ∼180 arcsec for JWST compared to ∼4680 arcsec of the Prime-Cam spectro-imager of the FYST). These surveys are excellent for studying the properties of individual galaxies but they will provide highly cosmic variance-limited statistical measurements compared to those from the LIM surveys of FYST. In addition, the much wider surveys of FYST will render possible the measurement of the clustering properties of SF galaxies at the (post-)EoR and thus shed light on the formation of the first large scale structure of the Universe.

Naturally, FYST is not the sole experiment that aims at performing [CII] LIM maps of the (post-)EoR. Nevertheless, while the TIME and CONCERTO experiments will rely as FYST on state-of-the-art spectro-imager instruments, they will operate on classic single-dish antennas as opposed to the novel "crossed Dragoned" configuration of FYST. The optical design of their instruments (e.g., field of view ∼840 arcsec for TIME and ∼1200 arcsec for CONCERTO) and their higher spatial- and spectroscopic-resolution motivates them to focus on smaller scales than FYST: the [CII] LIM planned surveys of TIME and CONCERTO are $0.1° \times 0.1°$ and $1.3° \times 1.3°$ wide, respectively, compared to the envisioned $4° \times 4°$ LIM survey of FYST. The higher resolution of CONCERTO and TIME will allow them to put stringent constraints on the [CII] PS shot-noise signal, which is mostly out of reach to FYST low-resolution observations. On the other hand, the wider survey will allow FYST to be the only [CII] LIM experiment to detect the [CII] PS clustering signal at the EoR and post-EoR[6]. Combining the [CII] PS measurements of the different experiments will therefore result in even more powerful constraints.

A common challenge for all LIM experiments is foreground contamination. The most critical contaminants of [CII] LIM are the cosmic infrared background (CIB) and the CO rotational lines emitted by foreground galaxies. The CIB is spectrally smooth, confined to the large Fourier scales, and can thus be easily rejected during the [CII] LIM statistical analysis. On the contrary, the CO line foreground contamination is not spectrally smooth and requires the development of complex mitigation methods. Those focus either on retrieving the PS or attempting to reconstruct the individual line maps (see CCAT-Prime Collaboration 2021 for a list of the available methods). In the second part of this paper series, we will test and evaluate several foreground mitigation methods using realistic astrophysical contaminants generated from our rTNG cone catalog.

5. Conclusions

In this paper, we forecast the [CII] mean intensity and PS at $z = 3.7$, 4.3, 5.8, and 7.4 and investigate the prospect of measuring it with the Prime-Cam spectro-imager of the FYST. We generate various versions of [CII] tomographic scans basing them on a common DM halo cone created using the DM halo catalogs of Illustris TNG300-1 simulation. We approximate the halo-to-galaxy SFR relation either by adopting the integrated SFR of Illustris TNG300-1 galaxies or the SFR coming from

[6] We note that CONCERTO could also detect the post-EoR [CII] PS clustering signal at $z \approx 4.5$ (see Chung et al. 2020).

abundance matching the DM halos of Illustris TNG300-1 with dust-corrected UV luminosity function of high-redshift galaxies. We couple these two alternatives with three SFR-to-$L_{[CII]}$ relations. We then estimate the [CII] mean intensity and PS of these various tomographic scans and study its detectability, assuming the technical characteristics of FYST and the planned LIM FYST survey of 4000 hours and $4^\circ \times 4^\circ$ sky coverage. Our main findings can be summarized as follows.

1. The forecasted mean [CII] line intensities emitted by (post-) EoR galaxies significantly decrease as we proceed to lower observing frequencies, corresponding to higher redshifts. Although all of our models follow this general redshift trend, there is up a factor of 10 difference among their predictions.
2. The amplitude of the forecasted [CII] intensity power spectrum ranges up to a factor of 30, depending on the selection of the halo-to-galaxy SFR and the SFR-to-$L_{[CII]}$ relations. The magnitude of the shot noise component of the PS is primarily sensitive to the selection of the SFR-to-$L_{[CII]}$ relation and at a more moderate level to the form of the M_h-SFR relation. The magnitude of the clustering component of the PS is mainly dependent on the cosmic SFRD of the model and at a lower level to the choice of the SFR-to-$L_{[CII]}$ relation.
3. The mass resolution of the TNG300-1 simulation affects the formation and evolution of galaxies residing in low-mass halos ($M_h < 10^{10}\,M_\odot$), which were therefore excluded from our rTNG cone catalog. Relying on the alternative method of abundance matching, we estimate that the contribution of $3 \times 10^9 < M_h/M_\odot < 10^{10}$ halos to the [CII] PS signal is only significant at $z = 6$, with a maximum amplification factor of $\times 1.69$, and $z = 7$, with a maximum amplification factor of $\times 6.25$.
4. FYST will be optimal to measure the [CII] PS signal at large, clustering-dominated scales ($k \lesssim 5 \times 10^{-2}\,\mathrm{Mpc}^{-1}$), where even our most pessimistic model is detected at $z = 3.7$, 4.3, and 5.8 and four out of six models give tentative detections at z = 7.4.
5. Detecting the [CII] PS at small, shot noise-dominated scales ($k \gtrsim 0.5\,\mathrm{Mpc}^{-1}$), where five out of six models are detected at $z = 3.7$ and 4.3, three out of six at $z = 5.8$, and none at $z = 7$, will be more challenging for the relatively low-resolution observations of FYST.
6. The detection of the [CII] PS at low- and high-spatial scales will constrain the halo-to-galaxy SFR relation, disentangling it from the precise form of the SFR-to-$L_{[CII]}$ relation.

Due to the exceptional location and the novel optical design of the telescope, FYST observations present an unparalleled opportunity for performing a [CII] PS measurement. As a result, its results will unravel key evolutionary properties of galaxies during the (post-)EoR.

Acknowledgements. We thank Dongwoo Chung, Dominik Riechers, Gordon Stacey,and other members of the CCAT-prime science working group for detailed discussions about EoR-Spec. We are grateful to Toma Badescu, Kevin Harrington, Ana Paola Mikler, Jens Erler, Eric F. Jimenez Andrade, Basilio Solis, Maude Charmetant, Ankur Dev, Enrico Garaldi, Victoria Yankelevich, Joseph Kuruvilla, Cristiano Porciani, Kaustuv moni Basu, Lydia Moser-Fischer, Stefanie Mühle, Reinhold Schaaf, and Eleni Vardoulaki for the helpful discussions. This research was carried out within the Collaborative Research Center 956, sub-projects A1 and C4, funded by the Deutsche Forschungsgemeinschaft (DFG) – project ID 184018867. This research made use of NASA's Astrophysics Data System Bibliographic Services; Matplotlib (Hunter 2007); Astropy, a community-developed core Python package for astronomy (Astropy Collaboration 2013); PlotDigitizer (http://plotdigitizer.sourceforge.net/).

References

Álvarez-Márquez, J., Colina, L., Marques-Chaves, R., et al. 2019, A&A, 629, A9
Appleton, P. N., Guillard, P., Boulanger, F., et al. 2013, ApJ, 777, 66
Astropy Collaboration (Robitaille, T. P., et al.) 2013, A&A, 558, A33
Basu, K., Hernández-Monteagudo, C., & Sunyaev, R. A. 2004, A&A, 416, 447
Bayet, E., Gerin, M., Phillips, T. G., & Contursi, A. 2009, MNRAS, 399, 264
Behroozi, P. S., Conroy, C., & Wechsler, R. H. 2010, ApJ, 717, 379
Behroozi, P., Wechsler, R. H., Hearin, A. P., & Conroy, C. 2019, MNRAS, 488, 3143
Bell, T. A., Viti, S., Williams, D. A., Crawford, I. A., & Price, R. J. 2005, MNRAS, 357, 961
Bell, T. A., Viti, S., & Williams, D. A. 2007, MNRAS, 378, 983
Béthermin, M., Wu, H.-Y., Lagache, G., et al. 2017, A&A, 607, A89
Bouwens, R. J., Illingworth, G. D., Oesch, P. A., et al. 2012a, ApJ, 754, 83
Bouwens, R. J., Illingworth, G. D., Oesch, P. A., et al. 2012b, ApJ, 752, L5
Bouwens, R. J., Illingworth, G. D., Oesch, P. A., et al. 2015, ApJ, 803, 34
Breysse, P. C., Kovetz, E. D., & Kamionkowski, M. 2014, MNRAS, 443, 3506
Breysse, P. C., Kovetz, E. D., Behroozi, P. S., Dai, L., & Kamionkowski, M. 2017, MNRAS, 467, 2996
Breysse, P. C., Yang, S., Somerville, R. S., et al. 2021, ApJ, submitted, [arXiv:2106.14904]
Carilli, C. L., & Walter, F. 2013, ARA&A, 51, 105
Carniani, S., Maiolino, R., Amorin, R., et al. 2018, MNRAS, 478, 1170
CCAT-Prime Collaboration (Aravena, M., et al.) 2021, ApJ, submitted, [arXiv:2107.10364]
Chardin, J., Puchwein, E., & Haehnelt, M. G. 2017, MNRAS, 465, 3429
Cheng, Y.-T., Chang, T.-C., Bock, J., Bradford, C. M., & Cooray, A. 2016, ApJ, 832, 165
Chung, D. T., Viero, M. P., Church, S. E., & Wechsler, R. H. 2020, ApJ, 892, 51
Comaschi, P., & Ferrara, A. 2016, MNRAS, 463, 3078
Corasaniti, P. S., Agarwal, S., Marsh, D. J. E., & Das, S. 2017, Phys. Rev. D, 95, 083512
Cormier, D., Lebouteiller, V., Madden, S. C., et al. 2012, A&A, 548, A20
Crawford, M. K., Genzel, R., Townes, C. H., & Watson, D. M. 1985, ApJ, 291, 755
Crites, A. T., Bock, J. J., Bradford, C. M., et al. 2014, in Millimeter, Submillimeter, and Far-Infrared Detectors and Instrumentation for Astronomy VII, eds. W. S. Holland, J. Zmuidzinas, et al., Int. Soc. Opt. Photonics (SPIE), 9153, 613
Croton, D. J., Springel, V., White, S. D. M., et al. 2006, MNRAS, 365, 11
Croxall, K. V., Smith, J. D., Pellegrini, E., et al. 2017, ApJ, 845, 96
De Looze, I., Cormier, D., Lebouteiller, V., et al. 2014, A&A, 568, A62
Donnari, M., Pillepich, A., Nelson, D., et al. 2019, MNRAS, 485, 4817
Dumitru, S., Kulkarni, G., Lagache, G., & Haehnelt, M. G. 2019, MNRAS, 485, 3486
Duncan, K., Conselice, C. J., Mortlock, A., et al. 2014, MNRAS, 444, 2960
Ferland, G. J., Porter, R. L., van Hoof, P. A. M., et al. 2013, Rev. Mex. Astron. Astrofis., 49, 137
Ferland, G. J., Chatzikos, M., Guzmán, F., et al. 2017, Rev. Mex. Astron. Astrofis., 53, 385
Finlator, K., Davé, R., & Özel, F. 2011, ApJ, 743, 169
Fujimoto, S., Ouchi, M., Ferrara, A., et al. 2019, ApJ, 887, 107
Fujimoto, S., Silverman, J. D., Bethermin, M., et al. 2020, ApJ, 900, 1
Garaldi, E., Compostella, M., & Porciani, C. 2019, MNRAS, 483, 5301
Gnedin, N. Y. 2000, ApJ, 542, 535
Gong, Y., Cooray, A., Silva, M. B., Santos, M. G., & Lubin, P. 2011, ApJ, 728, L46
Gong, Y., Cooray, A., Silva, M., et al. 2012, ApJ, 745, 49
Gong, Y., Cooray, A., Silva, M. B., et al. 2017, ApJ, 835, 273
Graciá-Carpio, J., Sturm, E., Hailey-Dunsheath, S., et al. 2011, ApJ, 728, L7
Hassan, S., Davé, R., Mitra, S., et al. 2018, MNRAS, 473, 227
Herrera-Camus, R., Bolatto, A. D., Wolfire, M. G., et al. 2015, ApJ, 800, 1
Huchra, J. P., & Geller, M. J. 1982, ApJ, 257, 423
Hunter, J. D. 2007, Comput. Sci. Eng., 9, 90
Jeong, D. 2010, PhD Thesis, The University of Texas at Austin, USA
Katz, H., Kimm, T., Sijacki, D., & Haehnelt, M. G. 2017, MNRAS, 468, 4831
Kaufman, M. J., Wolfire, M. G., Hollenbach, D. J., & Luhman, M. L. 1999, ApJ, 527, 795
Kennicutt, R. C. Jr. 1998, ARA&A, 36, 189
Koprowski, M., Coppin, K., Geach, J., et al. 2018, MNRAS, 479, 4355
Kravtsov, A. V., Berlind, A. A., Wechsler, R. H., et al. 2004, ApJ, 609, 35
Kovetz, E. D., Viero, M. P., Lidz, A., et al. 2017, ArXiv e-prints [arXiv:1709.09066]
Kuhlen, M., & Faucher-Giguère, C.-A. 2012, MNRAS, 423, 862

Kulkarni, G., Choudhury, T. R., Puchwein, E., & Haehnelt, M. G. 2017, MNRAS, 469, 4283
Lagache, G., Cousin, M., & Chatzikos, M. 2018, A&A, 609, A130
Le Fèvre, O., Béthermin, M., Faisst, A., et al. 2020, A&A, 643, A1
Li, T. Y., Wechsler, R. H., Devaraj, K., & Church, S. E. 2016, ApJ, 817, 169
Lidz, A., & Taylor, J. 2016, ApJ, 825, 143
Lidz, A., Furlanetto, S. R., Oh, S. P., et al. 2011, ApJ, 741, 70
Lord, S. D., Malhotra, S., Lim, T., et al. 1996, A&A, 315, L117
Madau, P., & Dickinson, M. 2014, ARA&A, 52, 415
Madau, P., & Haardt, F. 2015, ApJ, 813, L8
Madden, S., Geis, N., Genzel, R., et al. 1997, in The Far Infrared and Submillimetre Universe, ed. A. Wilson, et al., ESA Spec. Publ., 401, 111
Mannucci, F., Cresci, G., Maiolino, R., Marconi, A., & Gnerucci, A. 2010, MNRAS, 408, 2115
Mashian, N., Sternberg, A., & Loeb, A. 2015, JCAP, 2015, 028
McQuinn, M. 2016, ARA&A, 54, 313
Mitra, S., Choudhury, T. R., & Ferrara, A. 2018, MNRAS, 473, 1416
Murray, S. G., Power, C., & Robotham, A. S. G. 2013, Astron. Comput., 3, 23
Nelson, D., Pillepich, A., Genel, S., et al. 2015, Astron. Comput., 13, 12
Noh, Y., & McQuinn, M. 2014, MNRAS, 444, 503
Olsen, K. P., Greve, T. R., Narayanan, D., et al. 2015, ApJ, 814, 76
Olsen, K., Greve, T. R., Narayanan, D., et al. 2017, ApJ, 846, 105
Padmanabhan, H. 2019, MNRAS, 488, 3014
Pallottini, A., Gallerani, S., Ferrara, A., et al. 2015, MNRAS, 453, 1898
Pallottini, A., Ferrara, A., Bovino, S., et al. 2017a, MNRAS, 471, 4128
Pallottini, A., Ferrara, A., Gallerani, S., et al. 2017b, MNRAS, 465, 2540
Pillepich, A., Springel, V., Nelson, D., et al. 2018a, MNRAS, 473, 4077
Pillepich, A., Nelson, D., Hernquist, L., et al. 2018b, MNRAS, 475, 648
Pineda, J. L., Langer, W. D., & Goldsmith, P. F. 2014, A&A, 570, A121
Planck Collaboration I. 2020, A&A, 641, A1
Planck Collaboration XIII. 2016, A&A, 594, A13
Planck Collaboration XXX. 2014, A&A, 571, A30
Pullen, A. R., Serra, P., Chang, T.-C., Doré, O., & Ho, S. 2018, MNRAS, 478, 1911
Righi, M., Hernández-Monteagudo, C., & Sunyaev, R. A. 2008, A&A, 489, 489
Robertson, B. E., Furlanetto, S. R., Schneider, E., et al. 2013, ApJ, 768, 71
Rodriguez-Gomez, V., Genel, S., Vogelsberger, M., et al. 2015, MNRAS, 449, 49
Schaerer, D., Ginolfi, M., Béthermin, M., et al. 2020, A&A, 643, A3
Schechter, P. 1976, ApJ, 203, 297
Serra, P., Doré, O., & Lagache, G. 2016, ApJ, 833, 153
Sheth, R. K., & Tormen, G. 1999, MNRAS, 308, 119
Silva, M., Santos, M. G., Cooray, A., & Gong, Y. 2015, ApJ, 806, 209
Speagle, J. S., Steinhardt, C. L., Capak, P. L., & Silverman, J. D. 2014, ApJS, 214, 15
Spinoglio, L., Dasyra, K. M., Franceschini, A., et al. 2012, ApJ, 745, 171
Stacey, G. J., Geis, N., Genzel, R., et al. 1991, ApJ, 373, 423
Stacey, G. J., Aravena, M., Basu, K., et al. 2018, SPIE Conf. Ser., 10700, 107001M
Sun, G., Moncelsi, L., Viero, M. P., et al. 2018, ApJ, 856, 107
Thoul, A. A., & Weinberg, D. H. 1996, ApJ, 465, 608
Uzgil, B. D., Aguirre, J. E., Bradford, C. M., & Lidz, A. 2014, ApJ, 793, 116
Vallini, L., Gallerani, S., Ferrara, A., Pallottini, A., & Yue, B. 2015, ApJ, 813, 36
Vavagiakis, E. M., Ahmed, Z., Ali, A., et al. 2018, in Millimeter, Submillimeter, and Far-Infrared Detectors and Instrumentation for Astronomy IX, SPIE Conf. Ser., 10708, 107081U
Velusamy, T., & Langer, W. D. 2014, A&A, 572, A45
Wechsler, R. H., & Tinker, J. L. 2018, ARA&A, 56, 435
Wright, E. L., Mather, J. C., Bennett, C. L., et al. 1991, ApJ, 381, 200
Yang, S., Pullen, A. R., & Switzer, E. R. 2019, MNRAS, 489, L53
Yue, B., & Ferrara, A. 2019, MNRAS, 490, 1928
Yue, B., Ferrara, A., Pallottini, A., Gallerani, S., & Vallini, L. 2015, MNRAS, 450, 3829
Zaroubi, S. 2013, in The Epoch of Reionization, eds. T. Wiklind, B. Mobasher, & V. Bromm, Astrophys. Space Sci. Lib., 396, 45

APPENDIX B

[CII] line intensity mapping the epoch of reionization with the Prime-Cam on FYST. II. CO foreground masking based on an external catalog

The paper is reproduced below in its revised form following the first round of revisions.

Astronomy & Astrophysics manuscript no. output
September 18, 2024

[CII] line intensity mapping the epoch of reionization with the Prime-Cam on FYST

II. CO foreground masking based on an external catalog

C. Karoumpis ⋆[1], B. Magnelli[2], E. Romano-Díaz[1], K. Garcia[3], A. Dev[1], J. Clarke[4], T.-M. Wang[1], T. Bădescu[1], D. Riechers[4], and F. Bertoldi[1]

[1] Argelander Institut für Astronomie, Universität Bonn, Auf dem Hügel 71, D-53121 Bonn, Germany
[2] Université Paris-Saclay, Université Paris Cité, CEA, CNRS, AIM, 91191, Gif-sur-Yvette, France
[3] Department of Astronomy, University of Florida, 211 Bryant Space Science Center, Gainesville, FL 32611, USA
[4] I. Physikalisches Institut, Universität zu Köln, Zülpicher Straße 77, D-50937 Köln, Germany

September 18, 2024

ABSTRACT

Context. The Fred Young Submillimeter Telescope (FYST) line intensity mapping (LIM) survey will measure the power spectrum (PS) of the singly ionized carbon 158 μm fine-structure line, [CII], to trace the appearance of the first galaxies that emerged during and right after the epoch of reionization (EoR, $6 < z < 9$).
Aims. We aim to quantify the contamination of the (post-)EoR [CII] LIM signal by foreground carbon monoxide (CO) line emission ($3 < J_{\rm up} < 12$) and assess the efficiency to retrieve this [CII] LIM signal by the targeted masking of bright CO emitters.
Methods. Using the IllustrisTNG300 simulation, we produced mock CO intensity tomographies based on empirical star formation rate-to-CO luminosity relations. Combining these predictions with the [CII] PS predictions of the first paper of this series, we evaluated a masking technique where the interlopers are identified and masked using an external catalog whose properties are equivalent to those of a deep Euclid survey.
Results. Prior to masking, our [CII] PS forecast is an order of magnitude lower than the predicted CO contamination in the 225 GHz ([CII] emitted at $z = 6.8 - 8.3$) band of the FYST LIM survey, at the same level in its 280 GHz ([CII] emitted at $z = 5.3 - 6.3$) and 350 GHz ([CII] emitted at $z = 4.1 - 4.8$) bands, and an order of magnitude higher in its 410 GHz ([CII] emitted at $z = 3.4 - 3.9$) band. For our fiducial model, the optimal masking depth is reached when less than 10% of the survey volume is masked at 350 and 410 GHz but around 40% at 280 GHz and 60 % at 225 GHz. At these masking depths we anticipate a detection of the [CII] PS at 350 and 410 GHz, a tentative detection at 280 GHz, whereas at 225 GHz the CO signal still dominates our model. In the last case, alternative decontamination techniques will be needed.

Key words. Galaxies: evolution – Galaxies: statistics– Galaxies: star formation– Galaxies: high-redshift

1. Introduction

In its first billion years, the Universe underwent numerous changes. Following the Big Bang, the hot and ionized plasma cooled down, leading to the formation of neutral hydrogen atoms (e.g., Peebles 1968; Zel'dovich et al. 1969; Seager et al. 2000). This resulted in the Universe being in a state of darkness, known as the "Dark Ages". The advent of the first stars and galaxies, roughly 300 million years after the Big Bang, re-illuminated the Universe (e.g., Harikane et al. 2022). What makes this period in the history of the Universe even more special is that the appearance of the first light sources concurs with a phase transition in the intergalactic medium, from neutral to ionized (e.g., Becker et al. 2001; Barkana & Loeb 2001; Becker et al. 2015; Fan et al. 2006; Venemans et al. 2013), a period known as the Epoch of Reionization (EoR).

The connection between the reionization of the Universe and the emergence of the first light sources is well established in current theoretical models (e.g., Zaroubi 2013). Early massive stars located in the first incipient galaxies were the primary drivers of reionization, powering it through their ultraviolet (UV) emission. Despite this understanding, the intricacies of the interaction between early galaxy formation, evolution, and the reionization process remain elusive. Key uncertainties include the energy emitted by the early stars, the fraction of this energy that escaped the early galaxies (e.g., Bouwens et al. 2016), as well as the distribution of those ionizing sources in space and time. Unfortunately, these galaxies are too faint to be detected in large samples with current telescopes, including the state-of-the-art *James Webb Space Telescope* (JWST, Boylan-Kolchin et al. 2015), which creates challenges for accurately estimating the properties of their population and does not allow for tracing the large-scale structure in which they reside.

A more effective approach than traditional galaxy surveys for tracing both star formation in early galaxies and the large-scale structure in which they reside is line intensity mapping (LIM; see, e.g., Kovetz et al. 2019; Bernal & Kovetz 2022). This method measures the integrated emission of spectral lines from galaxies within a given spatial-spectral resolution element (voxel) using a spectro-imager. By focusing on the singly ionized carbon 158 μm fine-structure line, [CII], which is the brightest line in typical star-forming galaxies (e.g., Stacey et al. 1991) and

⋆ e-mail: karoumpis@astro.uni-bonn.de

an indicator of star formation rate (SFR; e.g, De Looze et al. 2014; Le Fèvre et al. 2020; Béthermin et al. 2020; Schaerer et al. 2020a; Bouwens et al. 2022), a 3-dimensional (3D) tomography of galaxies during the early universe can be obtained (e.g., Karoumpis et al. 2022). Several LIM experiments, such as the EXperiment for Cryogenic Large-Aperture Intensity Mapping (EXCLAIM, Pullen et al. 2023), the Terahertz Intensity Mapper (TIM, Vieira et al. 2020), the CarbON CII line in post-rEionization and ReionizaTiOn (CONCERTO) project (CONCERTO Collaboration et al. 2020), the Tomographic Ionized-carbon Mapping Experiment (TIME, Sun et al. 2021), and the Fred Young Submillimeter Telescope (FYST, CCAT-Prime Collaboration et al. 2023), are underway to target [CII] emission coming from EoR ($6 < z < 9$) and post-EoR ($3 < z < 6$) redshifts.

Many of these observatories will prioritize measuring the variance in the Fourier mode of these 3D tomographies through their spherically averaged power spectrum (PS). This statistical metric, although relatively simple, offers powerful limits on the underlying line luminosity function, given that the PS correlates with both the first moment (for scales > 10 Mpc) and the second moment (at scales < 10 Mpc) of the line luminosity function (Karoumpis et al. 2022). Such robust constrains of the luminosity functions of [CII] will provide rigorous statistical constraints on the SFR of (post-)EoR galaxies—a pivotal, yet elusive parameter in reionization models (e.g., CCAT-Prime Collaboration et al. 2023; Karoumpis et al. 2022).

In this context, where precise measurements of the [CII] PS at different scales during and after the EoR will be possible, it is crucial to study how various cosmic galaxy evolution models influence this PS and can thus be tested by comparison with future LIM measurements. To contribute to this effort, in the first article of this series (Karoumpis et al. 2022), we generated a span of predictions by post-processing the dark matter halo catalog from the IllustrisTNG300 hydrodynamical simulation (TNG300; Pillepich et al. 2018). We then used our predictions to assess the feasibility of detecting the PS of the [CII] line from galaxies at redshifts between 3 and 8 using the spectro-imager of FYST. Our results, which are consistent with empirically motivated predictions (Clarke et al. 2024), demonstrated promising potential for detecting the [CII] PS at the critical comoving length scale of 10 Mpc in four selected FYST bands centered at redshifts 3.7, 4.3, 5.8, and tentatively at redshift 7 (i.e., 410, 350, 280, and 225 GHz). However, those predictions did not account for a significant challenge faced by the LIM technique: the difficulty in distinguishing the contribution of (post-)EoR [CII] galaxies from the infrared (IR) continuum and carbon monoxide (CO) rotational line emission ($2 < J_{\rm up} < 12$) of galaxies located at the same solid angle but at lower redshifts ($z = 0 - 5.7$; see Fig. 1 and Table 1). While the IR continuum emission is not a major concern for the PS measurement as it is spectrally smooth and its frequency-coherent spectrum can be fitted and removed (Van Cuyck et al. 2023), the contribution of CO emitters presents a real challenge since the variance of their emission is of the same order or even exceeds that of the [CII] galaxies (e.g., Béthermin et al. 2022; Roy et al. 2023).

In this paper, we utilized the halo catalog from our previous work (Karoumpis et al. 2022), and by implementing empirical relations between SFRs and CO line luminosities of galaxies, we modeled the foreground line emission corresponding to the same frequencies as the (post-)EoR [CII] emission. Drawing from these predictions, we evaluated a foreground removal method where voxels containing luminous CO emitters are identified and masked using mock external catalogs with realistic characteristics. To this end, we assumed that the FYST LIM survey will cover a region of the sky benefiting from an external catalog with similar stellar mass completeness limits as the Euclid deep fields (Euclid Collaboration et al. 2022). This external catalog provides the angular position, redshift, stellar mass and SFR of the galaxies and it is used to pinpoint and mask voxels with a high likelihood of containing bright CO emitters. By carefully simulating this technique, we not only assess its effectiveness in mitigating CO contamination, but also examine its influence on the recovered [CII] PS. This includes an analysis of heightened measurement uncertainty resulting from diminished survey volume and the effects of a convolved PS attributable to the window function of the mask.

The paper is organized as follows. Section 2 introduces the formalism adopted for the modeling of the [CII] and CO emission. Section 3 describes the construction of the mock external catalog, and provides an overview of the masking technique. Section 4 examines the statistical properties of the individual CO lines, the impact of masking on the CO PS, the targeted [CII] PS, and the total line CO+[CII] PS. Finally, in Section 5, we critically assess the limitations of our work and suggest potential improvements and additions to our models. Throughout the paper, we adopt a ΛCDM cosmology with the same parameters used in the TNG300 simulation (Pillepich et al. 2018): $h = 0.71$, $\Omega_{\rm b} = 0.046$, $\Omega_{\rm m} = 0.281$, $\sigma_8 = 0.8$, $\Omega_\Lambda = 0.719$, and $n_{\rm s} = 0.963$.

2. Generating the mock FYST LIM survey

The Fred Young Submillimeter Telescope (FYST, CCAT-Prime Collaboration et al. 2023) is set to be a state-of-the-art, 6-meter diameter telescope designed for submillimeter to millimeter observations. Placed at 5600 meters on Cerro Chajnantor, FYST will utilize a novel crossed-Dragone optical design (Dragone 1978; Parshley et al. 2018) for fast and efficient wide-field-of-view sky mapping. One of its key instruments, the Prime-Cam receiver, will offer impressive spectroscopic and broadband measurement capabilities, enabling a mapping speed over ten times faster than existing facilities (Vavagiakis et al. 2018). Prime-Cam features seven instrument modules tailored to specific scientific programs. Two of the modules, named Epoch of Reionization Spectrometer (EoR-Spec, Huber et al. 2022), integrate a Fabry-Perot interferometer (Perot & Fabry 1899; Zou et al. 2022) to observe the [CII] line emission at $z = 3.5 - 8.05$ (210 to 420 GHz) with a resolving power of approximately $\Delta\lambda/\lambda = 100$. EoR-Spec will target two 5 deg^2 regions in a survey dedicated to measuring the [CII] PS from (post-)EoR galaxies (CCAT-Prime Collaboration et al. 2023). The chosen survey fields require sensitive auxiliary observations with extensive wavelength coverage to help remove foreground sources (see Sect. 3). Consequently, the Extended-COSMOS (E-COSMOS, Aihara et al. 2018), and Extended-Chandra Deep Field South (E-CDFS, Lehmer et al. 2005) contained in the Euclid Deep Field Fornax (EDF-F, Euclid Collaboration et al. 2022) are the selected fields for the FYST LIM survey. Existing deep coverage in various bands for these fields will soon be augmented by forthcoming imaging and spectroscopy data from present and future state-of-the-art observatories like JWST, Roman, Euclid, and the Large Millimeter Telescope (LMT). For a comprehensive overview of both current and upcoming datasets, see CCAT-Prime Collaboration et al. (2023).

In this context, realistic simulations of the FYST LIM survey are crucial. They allow for the optimization of the survey strategy, the examination of its ability to detect the [CII] LIM signal during the (post-)EoR, and the testing of various foreground mitigation strategies. To this end, we utilize the TNG300 simulation

to create a $4^\circ \times 4^\circ$ cone of mock galaxies spanning from $z \approx 0-9$ (see Sect. 2.1). The [CII] line emission from these galaxies is then incorporated, focusing on the $z \approx 3.4-8.3$ range to which the FYST observed frequencies are sensitive (Karoumpis et al. 2022, hereafter Paper I; see Sect. 2.2 for a summary). Subsequently, we introduce the CO ($J_{\rm up} = 3-12$) foregrounds which, in the context of FYST, are emitted by galaxies in the $z \approx 0-5.7$ range (see Sect. 2.3). The constructed observable cone is then transformed into mock FYST LIM tomographies (see Sect. 2.4), containing both the foreground CO and background [CII] emission, that serves as the basis for evaluating our masking technique.

2.1. The cone of mock galaxies

In this study, we utilized the dark matter (DM) halo catalog presented in Paper I, which contains all the essential results of the TNG300 simulation needed to estimate the line luminosity of the mock galaxies (i.e., angular position, redshift, M_*, SFR) which are defined as the gravitationally bound substructures hosted in the DM halos. This catalog corresponds to an observational cone encompassing a sky area of $4^\circ \times 4^\circ$ and a redshift range of $z = 0-9$, and it was constructed using the TNG300 halo catalogs as building blocks and corrected for resolution effects with the TNG100 DM halo catalogs as a reference (Pillepich et al. 2018). However, for the redshifts of the cone where galaxies emit the brightest CO lines in the frequency range of FYST (i.e., $z = 0-5.7$), we recalculated the resolution corrections, this time using the newly available TNG50 simulation (Pillepich et al. 2019). The reason for this update was that the CO emission originates from redshifts where the TNG100 simulation does not accurately reproduce the observed evolution of the cosmic SFR density (Madau & Dickinson 2014), with the peak epoch appearing at earlier cosmic times in the simulation ($z \approx 3$) than the observations ($z \approx 2$). Owing to its 17 times better mass resolution, TNG50 closely follows the cosmic SFR density evolution of Madau & Dickinson (2014). The same applies for our cone after the new mass resolution corrections.

Our predictions of line intensities are based on a single realization of this $4^\circ \times 4^\circ$ field and therefore may be subject to sample variance, due to the small number of galaxies traced. This is particularly true at low redshift (near $z = 0$) where the comoving volume covered by our cone is small, and at high redshift (near $z = 7$) where star formation occurs predominantly in overdense regions. To quantify the expected sample variance, we calculated the coefficient of variation of the PS ($\rm CV_{PS}$), defined as $\rm CV_{PS} = \sigma_{PS}/\mu_{PS}$, where $\mu_{\rm PS}$ represents the mean PS value across the sample tomographies and $\sigma_{\rm PS}$ denotes the standard deviation of the PS. This calculation was performed for a tomography with a frequency coverage of 40 GHz and a $4^\circ \times 4^\circ$ field, using an analytical relationship from Gkogkou et al. (2023) that accounts for both the clustering component, which describes the correlation of sources at large scales, and the shot noise component, caused by the randomly distributed sources at all scales, for the [CII] and CO PS. We find that the coefficient of variation ($\rm CV_{PS}$) for the CO PS of the clustering (shot noise) component is highest at 410 GHz, with a value of $\approx 7\%$ ($\approx 4\%$), whereas for the [CII] PS, the $\rm CV_{PS}$ peaks at 225 GHz with a value of $\approx 8\%$ ($\approx 7\%$). Nevertheless, in Sects. 2.2 and 2.3 we demonstrate that uncertainties on the modeling of the CO and [CII] emission of galaxies introduced much larger uncertainties on the CO and [CII] PS. For example, in the cases of the CO PS at 350 GHz and the [CII] PS at 225 GHz, the relative variability of the models in relation to their mean, $(P_{\rm max} - P_{\rm min})/(P_{\rm max} + P_{\rm min})$, is $\approx 85\%$ and $\approx 90\%$ respectively. Therefore, while sample variance affects LIM survey covering only $4^\circ \times 4^\circ$ field, it does not significantly affect the evaluation of the masking technique performed in this paper.

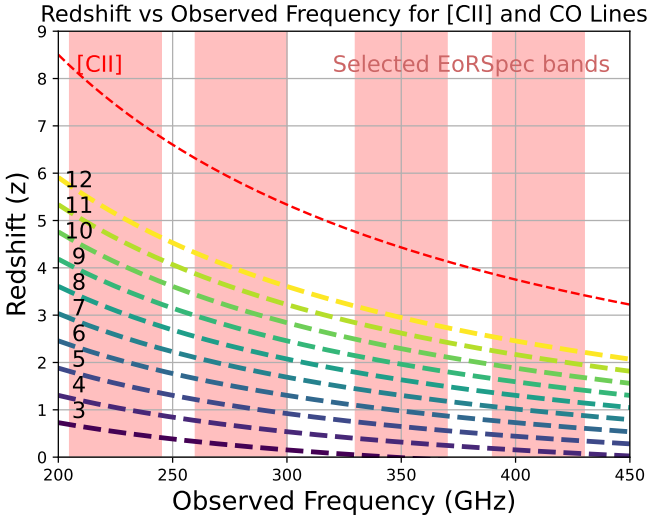

Fig. 1: Spectral lines observable within four selected EoR-Spec bands (illustrated by red-shaded regions), and originated from galaxies situated at different redshifts. The dashed numbered lines represent transitions within the CO rotational ladder, with the corresponding numbers indicating the $J_{\rm up}$ for each specific transition. These CO lines act as the foreground contaminant for the [CII] (red thin dashed line) LIM survey.

2.2. The [CII] emission

The mock galaxy catalog detailed in Sect. 2.1 underwent various post-processing methods to associate [CII] emission to its galaxies. We restricted these calculations to the redshift range of $z \approx 3.4-8.3$, where the [CII] emission of galaxies is redshifted into the observing bands of EoR-Spec. All the related methods and calculations are described in detail in Paper I and here we only summarize the most important steps. Firstly, SFRs were attributed to mock galaxies in two ways. One approach used their intrinsic TNG300 SFR, corrected to account for the mass resolution limitation of TNG300 (see Sect. 2.1). The other approach matched the mock galaxy abundance with the observed, dust-corrected ultraviolet luminosity function of high-redshift galaxies (Bouwens et al. 2015), assigning luminosities to the mock galaxies which are subsequently converted into SFRs following Kennicutt (1998). Secondly, the [CII] luminosities of the mock galaxies were estimated from the SFRs using three different SFR-to-$L_{\rm [CII]}$ relations: from a semi-analytic model of galaxy formation (Lagache et al. 2018), from a hydrodynamical simulation of a high-redshift galaxy (Vallini et al. 2015), and from a high-redshift [CII] galaxy survey (Schaerer et al. 2020b).

The various galaxy-to-SFR and SFR-to-$L_{\rm [CII]}$ relations translate into large variations of the amplitude of the expected [CII] PS (Paper I). Such variations render the assessment of the detectability of the [CII] PS more problematic but at the same time demonstrate the utility of this signal in discriminating between all these models. In the following, our fiducial [CII] model refers to the combination of the recalibrated TNG300 SFR with the SFR-to-$L_{\rm [CII]}$ relation from Vallini et al. (2015). It was chosen

as it produces results that closely align with the median value of our predictions (Paper I).

2.3. The CO emission

The CO molecule is the second most abundant molecule in the Universe, surpassed only by molecular hydrogen (H_2). In the typical conditions of giant molecular clouds, the rotational transitions of the CO that emit line emission are easily excited, making it the most widely used tracer of molecular gas in both the local (e.g., Wang & Hwang 2020; den Brok et al. 2021) and high-redshift universe (e.g., Solomon & Vanden Bout 2005; Daddi et al. 2015; Aravena et al. 2016; Riechers et al. 2019). Its luminosity is proportional to its mass, assuming the number of clouds is small enough for them not to overshadow each other and that they are close to virial equilibrium (e.g., Carilli & Walter 2013). The strong correlation between the CO line luminosities of galaxies and their molecular gas content enables us to forecast these foregrounds using our cone of mock galaxies.

2.3.1. The CO (1-0) luminosity

We estimated the molecular gas content of a galaxy, relying on the well-established relationship between molecular gas and star formation rate. Several studies have shown that the depletion time ($t_{\rm dep} = M_{\rm gas}/{\rm SFR}$) does not depend significantly on the stellar mass of galaxies and only slightly increases from $z \approx 4$ to $z \approx 0$ (e.g., Scoville et al. 2017; Tacconi et al. 2018; Kaasinen et al. 2019; Magnelli et al. 2020; Wang et al. 2022). Therefore, changes in the SFR of galaxies with stellar mass and redshift are primarily driven by changes in their gas reservoir. This allowed us to make the simplifying assumption that all galaxies convert their molecular gas into stars at a constant universal rate. To estimate the molecular gas masses of our mock galaxies, we multiplied their SFRs (the corrected intrinsic TNG300 SFRs presented in Sect. 2.1) by $t_{\rm dep} = 570$ Myr, corresponding to the depletion time of $z \approx 2$ galaxies with a stellar mass of $M_* \approx 10^{10} M_\odot$ (Tacconi et al. 2018). We verified that even with this simple approach, the cosmic molecular gas mass density inferred from our cone of mock galaxies was compatible with the observations of Riechers et al. (2019), Magnelli et al. (2020), Decarli et al. (2020), and Boogaard et al. (2023) (Fig. 2). This agreement is particularly true around the peak of the molecular gas mass density at $z \approx 2$, from where the bulk of the CO foregrounds originate. A more complex model that accounts for changes in the depletion time with redshift and distance from the main sequence (MS; for a definition, see Sect. 2.3.2) produces a similar gas mass density evolution, but to avoid introducing additional parameters, we adopted the simpler model of a constant depletion time.

The calculated molecular gas masses were then used to predict the CO line emission of each mock galaxy. We adopted a constant light-to-mass ratio between the specific luminosity of the CO (1-0) line and the molecular gas mass,

$$\alpha_{\rm CO} = \frac{M_{\rm gas}}{L'_{\rm CO(1-0)}} = 3.6\ M_\odot/{\rm K\ km\ s^{-1}\ pc^2}, \quad (1)$$

as its value for the MS galaxies does not seem to change significantly up to $z \approx 3$ (Decarli et al. 2016), and is adopted by the majority of the molecular gas measurements (Daddi et al. 2015; Riechers et al. 2019; Decarli et al. 2020; Lenkić et al. 2020; Chung et al. 2022).

There is observational evidence that starburst galaxies might require adjustments to their $\alpha_{\rm CO}$ and $t_{\rm dep}$. Specifically, a lower $t_{\rm dep}$ ($\approx$ 150 Myr as suggested in Tacconi et al. 2018) and a reduced $\alpha_{\rm CO}$ value of 0.8 (as suggested in Downes & Solomon 1998). Interestingly, the ratio of the proposed depletion times (570/150) is roughly equivalent to the ratio of the $\alpha_{\rm CO}$ values (3.6/0.8), meaning these changes may roughly offset each other. Therefore, while incorporating these adjustments would not significantly alter the $L_{\rm CO(1-0)}$ of our starbursts, it complicates the model further. For this reason, we have chosen to use the simpler model of a constant depletion time and $\alpha_{\rm CO}$. Nevertheless, the effect of starburst galaxies is further examined in Sect. 2.3.2.

More generally, although we may underestimate the stochasticity in our scaling relations for the CO(1-0) luminosities due to the simple assumptions of constant $t_{\rm dep}$ and αCO, the significant uncertainties introduced in Sect. 2.3.2 make any additional scatter in the CO(1-0) luminosities unnecessary for the scope of this study. There, by making some assumptions on the spectral line energy distribution (SLED) of our mock galaxies, we use these CO(1-0) line luminosities to predict the CO line luminosities in transitions that pose the most significant foreground challenges for our LIM survey (from Jup = 3 to $J_{\rm up} = 12$).

2.3.2. The CO SLED

The CO SLED of each galaxy is largely defined by the physical conditions (gas density and temperature) of its interstellar medium (ISM; e.g., Narayanan & Krumholz 2014). It is established that due to the diverse range of conditions in the ISM, the CO SLED of a galaxy often requires more than one temperature component to accurately describe it (Valentino et al. 2020). However, simulating the complex interactions of gas physics is beyond the scope of this paper.

Here we employed a model with a small number of free parameters, yet sufficiently advanced to replicate the CO luminosity function in various transitions observed by the Atacama Large Millimeter/submillimeter Array (ALMA) Spectroscopic Survey (ASPECS, Decarli et al. 2020; Boogaard et al. 2020; Riechers et al. 2020) at frequencies akin to our 225 GHz band (see Fig. 4 and Table 1). To achieve this, we adopted an empirical approach based on the galaxy position in the M_* – SFR diagram, which is a valuable tool for evaluating the properties of a galaxy. The majority of the galaxies on this diagram follows a so-called MS (Elbaz et al. 2007), wherein more massive galaxies tend to have higher SFRs. However, there are distinct exceptions: starburst galaxies, for instance, exhibit exceptionally high SFRs for their stellar masses; or passive galaxies, that have low SFR for their stellar masses. Here, we defined our MSs by fitting a log-linear relation to the M_* – SFR sequence followed by our mock galaxies at different redshifts. Then, we parameterized the position of a galaxy in this diagram using their distance from the MS, $\Delta{\rm MS} = \log({\rm SFR}/{\rm SFR_{MS}})$, where $\rm SFR_{MS}$ is the MS SFR at the redshift and stellar mass of the galaxy. Galaxies close to and below the MS have relatively cold ISM (e.g., Carilli & Walter 2013; Magdis et al. 2021), while those above the MS, such as starburst galaxies, have a warmer, denser ISM (e.g., Silich et al. 2009; Carilli & Walter 2013; Kamenetzky et al. 2017). Based on this assumption, we modeled the CO SLEDs of our mock galaxies by linearly combining the observed and well sampled CO SLEDs of a MS-like galaxy and a starburst-like galaxy. We used the CO SLED of the Milky Way (MW), as a characteristic star-forming galaxy with cold ISM conditions, slightly below the MS. On the other hand, we used the CO SLED of NGC253, a characteristic starburst galaxy with warm and dense ISM condi-

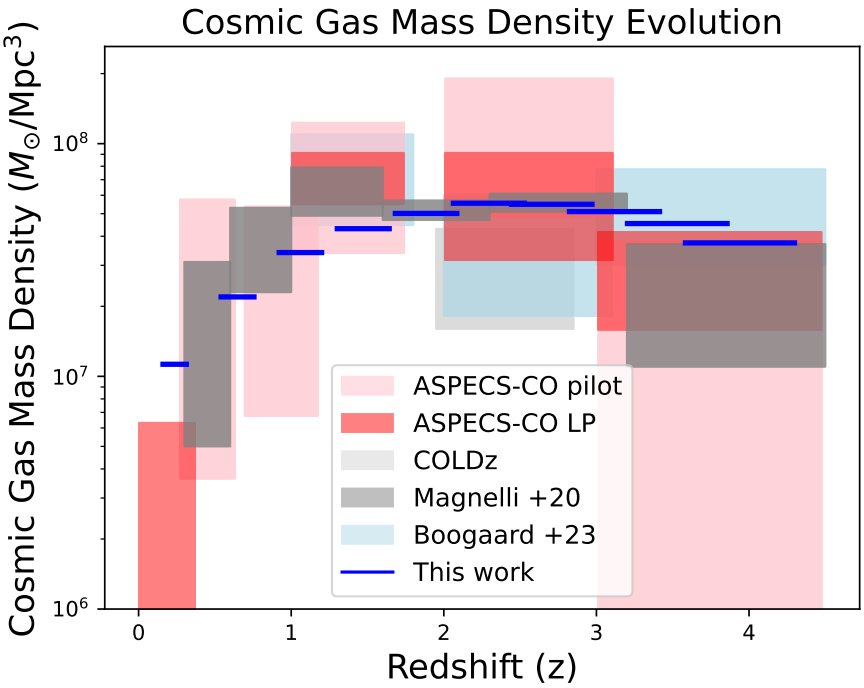

Fig. 2: Redshift evolution of the cosmic molecular gas mass density of galaxies. The blue horizontal line represents predictions from our cone of mock galaxies, while observational constraints are presented by rectangles. The gray rectangles are for the dust-based estimates of Magnelli et al. (2020), the light gray rectangles are for the COLDz CO survey (Riechers et al. 2019), the light blue rectangle for the CO-based estimates of Boogaard et al. (2023), the red-shaded rectangles are for the ASPECS CO pilot survey (Decarli et al. 2020), while the pink rectangles are for the ASPECS CO LP survey (Decarli et al. 2020). The width of the rectangles indicates the redshift bin size and the height the 1-σ confidence region.

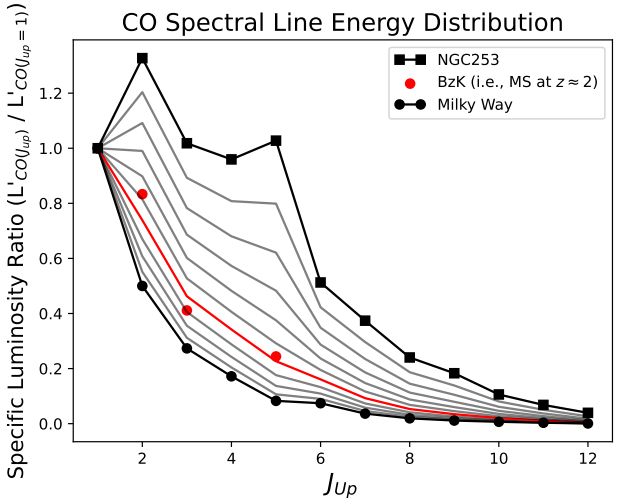

Fig. 3: CO SLED of the Milky Way (black circles) and NGC253 (black squares). The SLEDs resulting from the linear combination of the two, following Eq. 3, are shown by solid lines, with μ varying from 0 to 1 in steps of 0.1. The red line represents the combination (with $\mu = 0.4$) that best fit the BzK galaxies (red points) and is used here as reference for high-redshift MS galaxies.

tion. This linear combination allowed us to create a continuum of conditions that encompassed a broad range of galaxies from MS to starburst. This approach is supported by observations, which report a correlation between the CO SLED shape of a galaxy and its distance from the MS (e.g., Valentino et al. 2020; Cassata et al. 2020).

The CO SLED of the MW and NGC253 used in our study are displayed in Fig. 3. The MW observations up to $J_{\rm up} = 5$ were taken from Carilli & Walter (2013), and the SLED was extended to $J_{\rm up} = 6 - 10$ using the CO$\left(J_{\rm up} - J_{\rm low}\right)$/CO$(5-4)$ measurement from Wilson et al. (2017). The CO SLED of NGC253 was taken from Mashian et al. (2015). The difference between the MW and NGC253 CO SLEDs, which is greater at $J_{\rm up} = 5$, is due to the contrasting star formation environments in these galaxies. The MW features a cold, more diffuse molecular gas component, while the intense star formation of NGC253 creates a warm and dense gas environment, leading to higher excitation of CO molecules and an enhancement mid- to high-J ($J_{\rm up} = 4 - 8$) transition emission.

We assigned each mock galaxy a SLED resulting from its distance from the MS and the linear combination of these two extreme CO SLEDs. The mixing parameter (μ) was calibrated so that ΔMS $= 0$ yields a SLED consistent with typical MS galaxies at $z = 1.5$ (BzK galaxies; Daddi et al. 2015), and ΔMS $= 1.5$ produces the SLED of NGC253. In turn, this yields,

$$\mu = \frac{\Delta \mathrm{MS} + 1}{2.5}. \quad (2)$$

The CO SLED resulting from the linear mixing is given by the equation,

$$\log L'^{\rm galaxy}_{\rm CO(J_{up}-J_{low})} = (1-\mu) \log L'^{\rm MW}_{\rm CO(J_{up}-J_{low})} + \mu \log L'^{\rm NGC253}_{\rm CO(J_{up}-J_{low})}, \quad (3)$$

where $L'^{\rm galaxy}_{\rm CO(J_{up}-J_{low})}$, $L'^{\rm MW}_{\rm CO(J_{up}-J_{low})}$ and $L'^{\rm NGC253}_{\rm CO(J_{up}-J_{low})}$ are the CO($J_{\rm up} - J_{\rm low}$) specific line luminosities of our mock galaxy, the MW, and NGC253, respectively. Figure 3 displays an example of the individual CO SLEDs resulting from Eq. 3 (for $\mu = 0 - 1$ with steps of $\delta\mu = 0.1$). The linear combination highlighted in red corresponds to ΔMS = 0 (i.e. $\mu = 0.4$), and aligns by design closely with the observed CO SLEDs from BzK galaxies.

This approach where each galaxy has its individual CO SLED constitutes our fiducial model. However, we also considered two extreme models in addition to our fiducial, creating a larger range of possible values for the CO intensity tomographies. In the "low-contamination" model, all galaxies have the SLED of a typical MS galaxy (i.e., $\mu = 0.4$; BzK galaxies; Daddi et al. 2015), while in the "high-contamination" model, all galaxies have the SLED of a typical starburst (i.e., $\mu = 1$; NGC253).

To verify the accuracy of this approximation, we compared the CO luminosity function inferred from our fiducial, "low-" and "high-contamination" models to that observed by ASPECS (Fig. 4). Our model predictions cover a good range of the 1-σ interval compatible with the ASPECS measurements, with, however, a slight over-prediction of the faint end and under-prediction of the bright end. This former discrepancy could be due to the fact that ASPECS is a line-flux-limited CO survey, which naturally becomes less sensitive and more incomplete at the faint end of the CO luminosity function. The difference at the bright end between our models and the survey has been reported previously in the semi-analytical approach of Popping et al. (2019); Béthermin et al. (2022); Gkogkou et al. (2023). As suggested by Davé et al. (2020), this could be due to the assumption of a constant $\alpha_{\rm CO}$ for all of our galaxies. In any case, the galaxies of the brightest bin are few in number and therefore constitute a small percentage of the overall number of interlopers that should be masked. This slight underestimation should not therefore significantly impact our results.

2.4. The [CII] and CO mock intensity tomographies

In order to translate the line luminosities of our mock galaxies into mock line intensity tomographies, we assumed that the intensity of a line (either CO $J_{\rm up} = 3-12$ or [CII]) in a given voxel, positioned at a specific R.A., Dec, and ν, is expressed as:

$$I_{\rm line} = \frac{1}{\Delta\nu_0(\Delta\theta_{\rm b})^2}\left(\sum_{j\in{\rm voxel}}\frac{L^j_{\rm line}}{4\pi\, r_j^2(1+z_j)^2}\right) * G(R.A., Dec, \nu), \quad (4)$$

where r_j is the comoving distance of the j-th galaxy, which resides at a redshift z_j and has a line luminosity $L^j_{\rm line}$; $*$ is the symbol of the convolution; and $G(R.A., Dec, \nu)$ is the 3D Gaussian function representing the angular and spectral resolution element of the EoR-Spec. To adhere to the Nyquist-Shannon sampling theorem (Shannon 1949), we selected the grid spacing of the mock tomographies to be three times smaller than the full width at half maximum (FWHM) of this 3D Gaussian function. Since the summation of all galaxy luminosities within a voxel essentially represents the integration of the intensity field over the volume of the voxel, we divide twice by $\Delta\theta_{\rm b} = {\rm FWHM_{R.A.}}/3 = {\rm FWHM_{Dec}}/3 = {\rm FWHM_{ang}}/3$ and once by $\Delta\nu_0 = {\rm FWHM}_\nu/3$ to account for the spatial and frequency dimensions of the voxel. This ensures that the calculated intensity is properly normalized by the volume of the voxel.

We assumed that the FYST LIM survey will be divided into four tomographies for each of the four selected frequency bands of the EoR-Spec. These bands are centered at 225 ± 20, 280 ± 20, 350 ± 20, and 410 ± 20 GHz. The average FWHM of the spectral channels for these bands are 2.1, 2.7, 3.6, and 4.4 GHz, respectively. Additionally, the angular beam FWHM for these bands are 0.88, 0.77, 0.65, and 0.62 arcmin, respectively. The intended survey will cover an area of 5 deg^2. However, for our analysis, we focused on a 16 deg^2 field, as it offers a testbed with reduced sample variance. It is important to note that when calculating uncertainties (Sect. 4), we considered the sample variance and the white noise of the expected (i.e. two fields of 5 deg^2) size and observational time (2000 hours for each field) of the FYST LIM survey. This way we ensure that while the statistical parameters of the foregrounds and the targeted signal approximate the global values, the impact of any low number statistics is effectively captured within the uncertainty estimates.

3. The masking technique

While various alternative methods for addressing submillimeter line foreground contamination have been proposed in the literature, including spectral template fitting (Kogut et al. 2015; Cheng et al. 2020), blind masking (Breysse et al. 2015), and machine learning techniques (Moriwaki et al. 2020; Moriwaki & Yoshida 2021; Zhou et al. 2023), we focus on what appears to be the most effective approach—targeted masking (e.g., Yue et al. 2015; Silva et al. 2015; Sun et al. 2018). This technique employs external catalogs to identify the locations of the brightest foreground sources and mitigates their influence on the targeted PS by excluding the implicated voxels from further analysis.

In our study, the masks were created based on a mock external stellar mass-selected catalog (Sect. 3.1). In order to explore several depths of masking, for each CO line transition in each FYST frequency band, we created two masks of different depth: the "bright" and the "complete" masking arrays. To generate the "complete" masking arrays, we masked every galaxy in our stellar mass-complete external catalog with redshift $z_{\rm J_{up}} = (\nu_{\rm J_{up}}/\nu_{\rm obs} \pm 20\, GHz) - 1$, where $J_{\rm up}$ refers to the upper level of the CO transition, and $\nu_{\rm obs}$ is the central observed frequency of one of the four selected EoR-Spec bands.

For the "bright" masking arrays, we employed the same method but limited it to galaxies above the MS, (i.e., ΔMS > 0). This way to identify bright CO contaminants solely based on ΔMS stemmed from the observation that the cumulative CO line contamination from galaxies correlates with the MS boundary (see e.g., Fig. 5). By exclusively masking galaxies above the MS, we effectively limited our masks to those galaxies that significantly contaminate the targeted [CII] signal. This approach optimizes the survey volume available for our PS analysis. The masking arrays, constructed using these two subsamples, are presented in Sect. 3.2, and the methodology behind this masking strategy is discussed in further detail in Sect. 4.2.

3.1. The mock external catalog

The fields that will be targeted by the FYST LIM survey (CCAT-Prime Collaboration et al. 2023) are the E-COSMOS (Aihara et al. 2018) and the E-CDFS (Lehmer et al. 2005), with the latter potentially being extended to cover the whole EDF-F. To mimic the way these surveys would observe our cone of mock galaxies, we simply applied to our mock galaxy catalog redshift-dependent stellar mass limits akin to those affecting an Euclid-deep-like survey (Euclid Collaboration et al. 2020). According to the latest forecasts, such a survey will have multi-wavelength photometric sensitivities that will be equivalent to those obtained

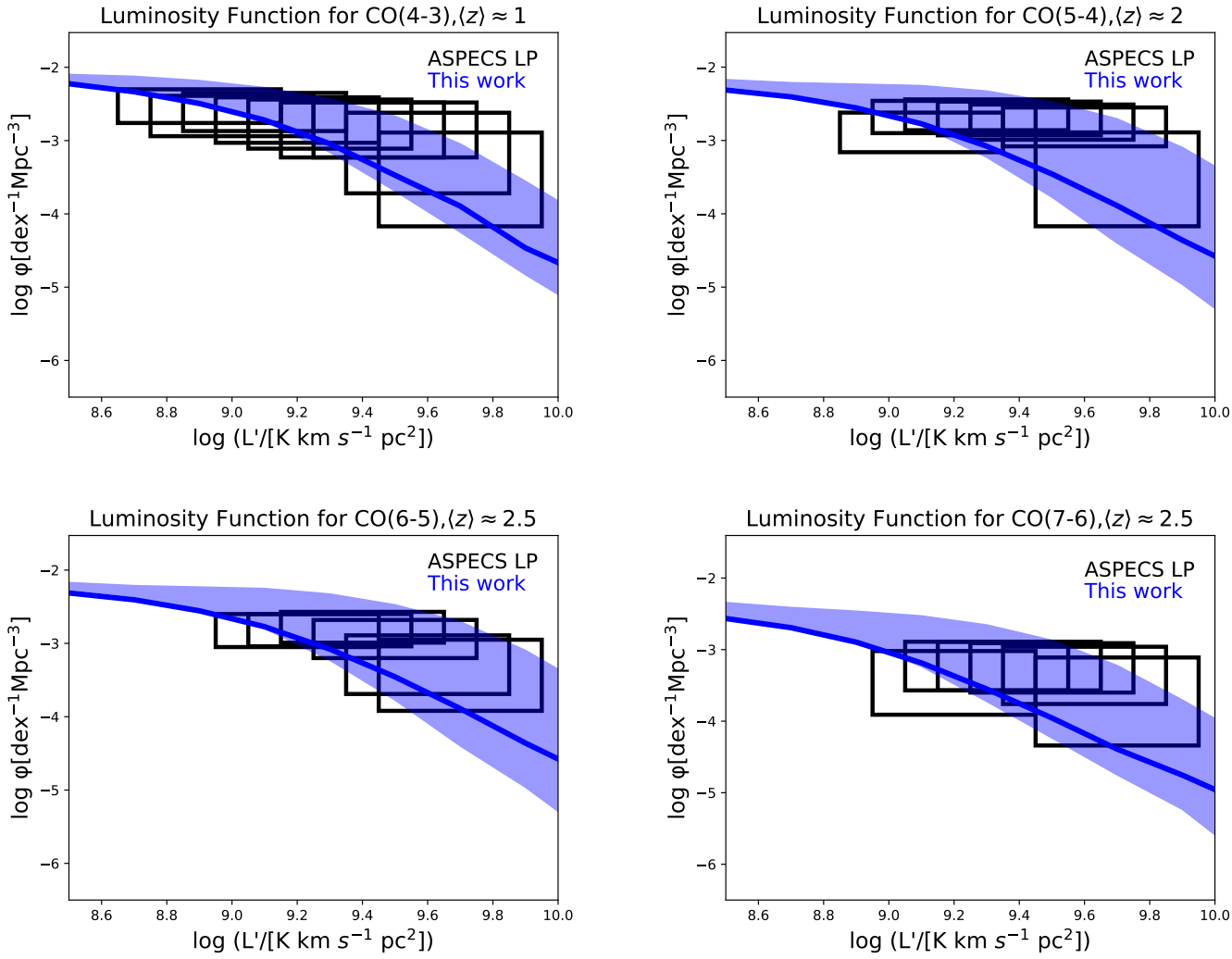

Fig. 4: The CO luminosity function for various transitions and redshifts. The blue line corresponds to our fiducial model, while the shaded region indicates the range resulting from our optimistic and pessimistic models. Rectangles represent observational data from the ASPECS LP survey (Decarli et al. 2020), with the width indicating the bin size and the height indicating the 1-σ confidence region.

today in the COSMOS field. By taking the stellar mass completeness limits from the COSMOS2015 (Laigle et al. 2016) and COSMOS2020 (Weaver et al. 2022) catalogs, we should thus obtain realistic redshift-dependent stellar mass limits to apply to our mock galaxy catalog. These redshift-dependent limits are shown in Fig. 6, starting at $\approx 0.5 \times 10^9 M_\odot$ at low redshifts ($z \approx 0-2$) and rising to $\approx 10^9 M_\odot$ at high-redshifts ($z \approx 2-4$).

In addition to the angular position, redshift information, and stellar mass, we also included in our mock external catalog the SFR for each galaxy. Indeed, we anticipated that the Euclid Deep Fields will provide SFR estimates for the majority of detected galaxies through the spectral energy distribution (SED) fit of all the available optical to near-infrared bands.

We note that the limited angular resolution of the EoR-Spec renders insignificant any potential offset between the CO position and the optically-based position of galaxies in this external catalog, or any potential astrometry inaccuracies in the external catalog. Uncertainties on the angular position of our mock galaxies were thus not included in our mock external catalog. Moreover, given that the Δz associated with our frequency channels largely exceeds the anticipated photometric redshift accuracy of $0.002 \times (1+z)$ from Euclid (Euclid Collaboration et al. 2021), uncertainties on the line-of-sight distance were also not included in our mock external catalog.

3.2. The masking array

The process of masking voxels containing bright CO contaminant is represented by a 3D array of zeros and ones, with zeros indicating voxels likely containing a bright CO emitter and thus requiring masking. This array is referred to as the binary masking array, B. Here, through empirical testing, we found that the most effective voxel size for masking is that of $(\mathrm{FWHM}_\nu/3) \times (\mathrm{FWHM}_{\mathrm{ang}}/3)^2$. It is important to note that observed LIM tomographies undergo convolution with the beam of the telescope. This results in intensity from galaxies within a voxel spilling over to neighboring voxels. Additionally, sharp masks, like our binary masking arrays, produce high-frequency components in their Fourier transform that are not well captured when sampling this space discretely. This causes high-frequency

Line	ν_r[GHz]	Δz(225 ± 20 GHz)	Δz(280 ± 20 GHz)	Δz(350 ± 20 GHz)	Δz(410 ± 20 GHz)
C II	1901.0	6.8 – 8.3	5.3 – 6.3	4.1 – 4.8	3.4 – 3.9
CO $J = 3 - 2$	345.8	0.4 – 0.7	0.2 – 0.3	0.0 – 0.05	···
CO $J = 4 - 3$	461.0	0.9 – 1.2	0.5 – 0.8	0.2 – 0.4	0.1 – 0.2
CO $J = 5 - 4$	576.3	1.4 – 1.8	0.9 – 1.2	0.6 – 0.7	0.3 – 0.5
CO $J = 6 - 5$	691.5	1.8 – 2.4	1.3 – 1.7	0.9 – 1.1	0.6 – 0.8
CO $J = 7 - 6$	806.7	2.3 – 2.9	1.7 – 2.1	1.2 – 1.4	0.9 – 1.1
CO $J = 8 - 7$	921.8	2.8 – 3.5	2.1 – 2.5	1.5 – 1.8	1.1 – 1.4
CO $J = 9 - 8$	1036.9	3.2 – 4	2.5 – 3.0	1.8 – 2.1	1.4 – 1.7
CO $J = 10 - 9$	1152.0	3.7 – 4.6	2.8 – 3.4	2.1 – 2.5	1.7 – 2.0
CO $J = 11 - 10$	1267.0	4.2 – 5.2	3.2 – 3.9	2.4 – 2.8	1.9 – 2.2
CO $J = 12 - 11$	1382.0	4.6 – 5.7	3.6 – 4.3	2.7 – 3.2	2.2 – 2.5

Table 1: The rest-frame frequencies (ν_r) of the [CII] line and of the brightest CO lines present in the selected EoR-Spec frequency bands and [CII], together with the redshift range from which their emission originate.

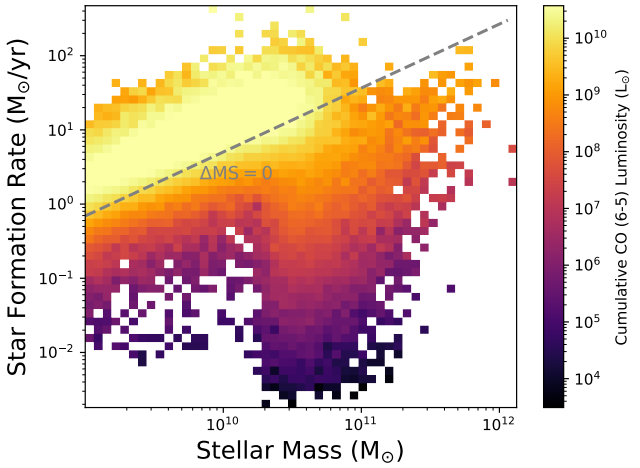

Fig. 5: SFR as a function of stellar mass with the bins color-coded to reflect the cumulative CO (6-5) luminosity of the 2D bin. The dashed line indicates the thresholds that define our "bright" subsample with $\Delta MS > 0$ (i.e., galaxies on and above the MS)

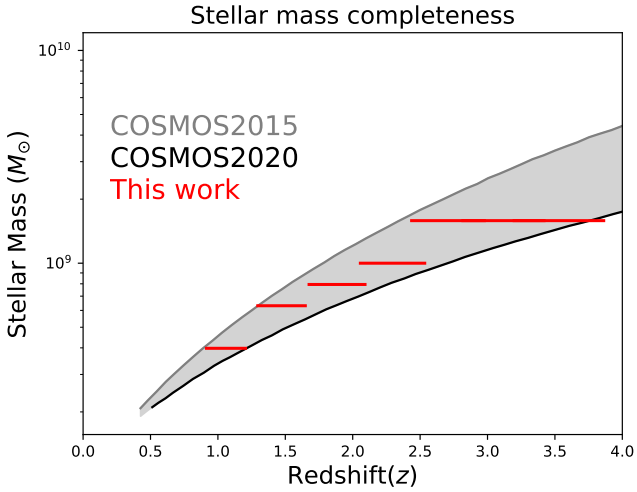

Fig. 6: Comparison of the stellar mass completeness limits applied to our mock external catalog (red line) with those of the COSMOS2015 (light gray line Laigle et al. 2016) and COSMOS2020 (dark gray line Weaver et al. 2022) catalogs. The stellar mass completeness limits of the deep Euclid catalogs is expected to lie between these two lines.

details to alias into lower frequencies, distorting the Fourier-transformed data.

A remedy for both issues is to smooth the binary mask using a 3D Gaussian normalized such that its volume integral is equal to 1, a 3D equivalent of the 2D method used in CMB studies (Ponthieu et al. 2011; Kim 2011). While Ponthieu et al. (2011) recommends a Gaussian size double the map resolution, we have opted for a size consistent with the 3D beam of the EoR-Spec. Indeed, due to our broader binning in Fourier space, we do not face the same level of aliasing as CMB studies. This choice aligns with the inherent resolution of the instrument and addresses potential aliasing without significantly reducing the survey volume. However, as highlighted by Kim (2011), Gaussian smoothing can risk foreground contamination, that is, pixels initially zero in the binary mask might become non-zero after smoothing. To counteract this, we multiplied the smoothed mask with the original binary mask.

With the above considerations, we generated our mask as follows: we subtracted B from a unit array, then convolved the outcome with the normalized 3D beam of the EoR-Spec, $G(R.A., Dec, \nu)$. By subtracting the convolution result from another unit array and multiplying it by the original binary array, we obtained the "applied masking array", M. Mathematically, this is expressed as:

$$M = B \times [\mathbf{1} - (\mathbf{1} - B) * G(R.A., Dec, \nu)], \quad (5)$$

where $\mathbf{1}$ is an array of ones of identical dimensions to B. Through this approach, the impact M has on the PS of a tomography mirrors the impact B has on the PS of a perfectly deconvolved map. This method bypasses deconvolution, a procedure that is not only computationally intensive but that can also amplify the noise of the observed data.

4. Results

4.1. Line intensities

To inform our masking strategy, we begin by analyzing the predicted intensities of the CO lines at the frequencies of the selected EoR-Spec bands (225 ± 20 GHz, 280 ± 20 GHz, 350 ± 20 GHz, and 410 ± 20 GHz), that is, comparing the mean values

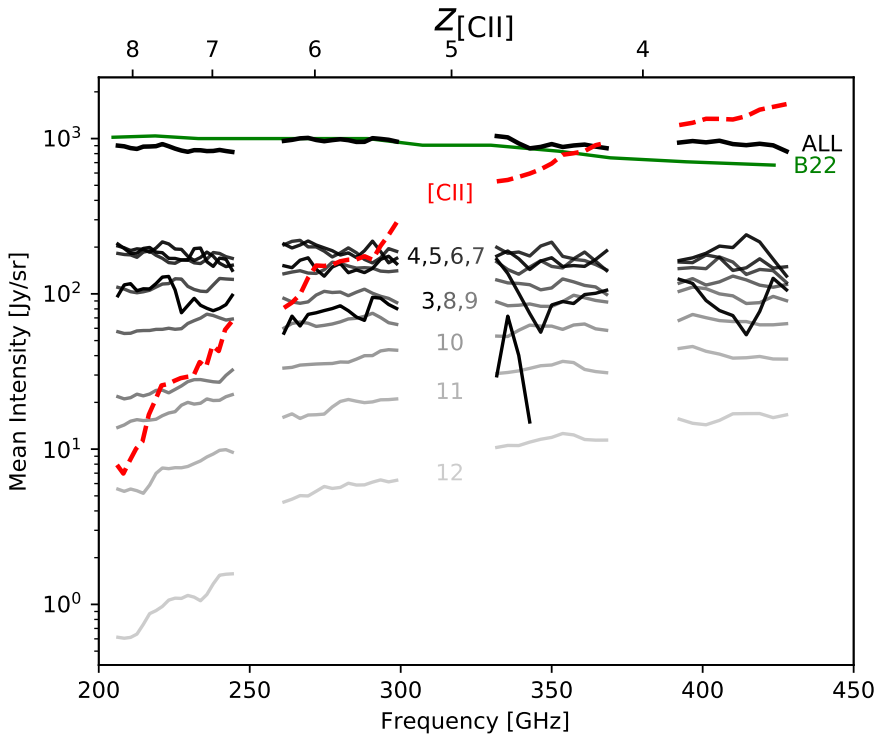

Fig. 7: Mean [CII] and CO line intensities as a function of the observed frequency (or emitted redshift for [CII]). The red dashed line depicts the [CII] fiducial model from Karoumpis et al. (2022). Continuous gray lines represent the prediction for the CO emission, with line shade decreasing as J_{up} (gray numbers) increases. The thicker black line indicates the mean total CO emission, while the Béthermin et al. (2022) prediction for total CO mean intensity (green line) is included for comparison.

(Fig. 7) and CV (i.e., σ_I/μ_I; Fig. 8) of their intensities to those of the targeted line, [CII].

Variations in the mean intensities of spectral lines at specific observed frequencies are primarily due to two factors: the different line luminosities of the galaxy populations emitting each line, and the different distances to each of these populations. In Fig. 7, we see a clear trend in the evolution of line mean intensity with observed frequency. As we shift towards lines with higher rest-frame frequency which therefore originate from higher redshifts, the gradient of their mean intensity as a function of frequency becomes markedly steeper. This steepening is a consequence of more substantial changes between the luminosity distances of galaxies of subsequent frequency channels when dealing with higher redshifts.

Notably the mean intensities of CO(3-2) and CO(4-3) exhibit significant fluctuations at frequencies above 300 GHz. This variability can be attributed to their origin from redshifts $z < 0.4$, where the volume encompassed by the observational cone is relatively small. Consequently, there is a limited number of emitting galaxies within this volume, leading to intensity fluctuations that are strongly driven by small number statistics. Furthermore, CO(3-2) cannot be observed at frequencies above 345.8 GHz, its rest frequency.

While the mean of the total CO intensity remains relatively constant at all frequencies ($\approx 10^3$ Jy/sr) and is always dominated by the low-J CO transition from low redshift galaxies, the [CII] intensity shows a notable increase from about ≈ 10 Jy/sr at 225 GHz to ≈ 2000 Jy/sr at 410 GHz. We estimate that [CII] becomes the dominant line at > 364 GHz, a prediction that matches well with the results of Béthermin et al. (2022) which quotes a crossover at 358 GHz.

The variability in intensity distribution, as indicated by the CV, is also critical for the efficiency of our masking method. A high CV implies that the line intensity is concentrated in fewer voxels, while a lower CV indicates a more uniform voxel-to-voxel distribution. This aspect becomes increasingly relevant as [CII] signal recovery becomes more challenging at lower frequencies (i.e. higher redshifts).

The differences in CV arise from variations in the size of the galaxy populations contributing to the intensity of each line. This size is contingent on the survey volume, which expands with increasing redshift, and the number density of star-forming galaxies, which peaks around $z \approx 3$ in the case of our mock observational cone (in agreement with observations like Conselice et al. 2016). Consequently, the CV typically decreases from $z \approx 0$ to $z \approx 4$ and then increases for higher redshifts, as shown in Fig. 8 in the case of the [CII] line. For the bright CO lines (i.e., $J_{up} = 4 - 9$, see Fig. 7), which are emitted by galaxies at $z < 4$, only the decreasing trend appears. On the other hand, for the CO lines with $J_{up} > 10$, CV is constant with redshift at > 280 GHz since they originate from $z \approx 2 - 3$, where the survey volume expands slowly. Additionally, for these J_{up}, an increasing trend appears at lower frequencies (< 280 GHz) where these lines are emitted by galaxies at $z > 4$ where the number density of galaxies decreases rapidly.

Just by comparing the mean and the CV of the line intensities and before even applying any mask, we observe a clear dichotomy. On the one hand, for the recovery of the [CII] emission originating from $z < 5$ galaxies, the situation is encouraging as the foregrounds have comparable intensity with the targeted signal and the dominating low-J line emission is scarcely distributed in the surveyed volume (i.e., their CV is high). On the

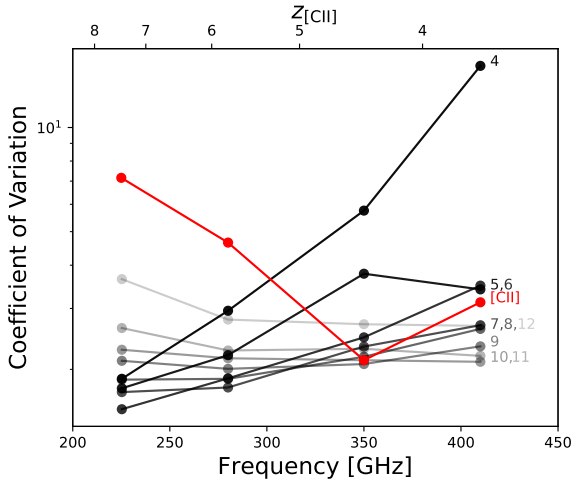

Fig. 8: Coefficient of variation of the [CII] (red) and CO lines (gray) intensities for the four FYST frequency bands. The gray numbers of decreasing opacity denote the J_{up} of the CO transition. The secondary x-axis indicating redshift applies solely to [CII] emitters.

other hand, for the recovery of the [CII] emission from $z > 5$ galaxies, the situation appears less favorable as the foregrounds are on average more than an order of magnitude brighter than the targeted signal and the dominating low-J line emission is homogeneously distributed in the surveyed volume (i.e., CV is low). In the following section, we explore and quantify how these differences impact the effectiveness of the masking technique in removing the CO signal. There, it becomes clear that the differences in the CV of the CO intensity result in high masking efficiency (significant CO reduction with a small fraction of the survey volume masked) for our low-redshift (high-frequency) tomographies, but low masking efficiency (poor CO reduction with a large fraction of the survey volume masked) for our high-redshift (low-frequency) tomographies.

4.2. Evaluating the masking technique efficiency

The effectiveness of a foreground removal technique can only be evaluated by its impact on the statistic of interest. Our study utilizes the spherically averaged PS, computed within the comoving volume of the [CII] reference frame, thus standardizing the analysis frame to avoid constant conversions between different lines. Contrasting with the approach in Paper I, here we compute the PS for tomographies convolved with the 3D beam of the EoR-Spec, rather than incorporating the beam attenuation into the uncertainty of the PS. This adjustment allows us to simulate the effect that the interplay between the transfer functions of the beam and the mask has on the measured PS. We are focusing on the PS at $k = 0.02 - 0.32$ Mpc^{-1}, a scale that is less affected by sample variance and masking bias. However, our findings hold true at higher k-bins ($k = 0.32 - 0.62$ Mpc^{-1} and $k = 0.62 - 0.92$ Mpc^{-1}), suggesting that the effectiveness of the masking strategy is relatively constant across a broad range of scales.

Mitigating CO contamination while preserving maximal survey volume is far from straightforward due to the variety of possible CO masks and their nuanced effects on both CO and [CII] PS. To unravel these complex behaviors, we have adopted a three-step approach: initially focusing on CO alone to deduce the optimal masking sequence and strategy (Sect. 4.2.1), then examining the impact of masking on the [CII] signal in isolation (Sect. 4.2.2), and finally analyzing the combined effects to fully understand the interplay between masking, CO contamination, and the [CII] signal (Sect. 4.2.3). This comprehensive approach will not only enable us to identify the optimal masking depth, but also to assess the level of contamination at this depth.

4.2.1. Impact of masking on the CO PS

As already discussed in Sect. 3, for each frequency band and for each CO line we generated two distinct masking arrays: a "complete" masking array that masks all the galaxies in our external catalog with $z_{J_{up}} = (\nu_{J_{up}}/\nu_{obs} \pm 20\text{GHz}) - 1$ and a "bright" masking array that among the galaxies of the "complete" subsample masks only those with $\Delta\text{MS} > 0$.

Given the multitude of available masks, each with a unique impact on the observed data, identifying the optimal masking sequence becomes a critical challenge in our analysis. Therefore, it is important to establish a reliable criterion for determining the most effective sequence of masks. The effectiveness, $E(J_{up}$, bright or complete) of masking arrays, $M(J_{up}$, bright or complete), is quantified as,

$$E = \frac{\text{Standard deviation}_{\text{unmasked}} - \text{Standard deviation}_{\text{masked}}}{\text{Number of masked voxels}}. \quad (6)$$

The reason for this definition of E is that we need a scale independent value that correlates with the amplitude of the PS per number of masked voxels, like the standard deviation of the intensity normalized by the number of voxels does.

The masking array with the highest E is applied iteratively to the CO-only tomography, continuing until all arrays have been utilized. With each iteration, we recalculate the effectiveness of subsequent masks on the updated data. This iterative process, performed on our CO-only simulations, identifies a sequence of masking arrays for each LIM tomography. It is important to note that this optimal sequence of CO masks remains unchanged at 350 ± 20 GHz and 410 ± 20 GHz if evaluated on a tomography including CO, [CII], and realistic white noise for the FYST LIM survey. In such tomographies, the masking efficiency (E) for each CO line is indeed still dominated by the CO signal. However, at 225 ± 20 GHz and 280 ± 20 GHz, where the [CII] signal and white noise become increasingly important, it is not practical to evaluate the optimal CO masking sequence directly from a realistic tomography including CO, [CII] and instrumental white noise. However, for all our tomographies, we observed that the optimal CO masking sequence does not vary much across the range of CO foreground models implemented in our work. This implies that the optimal CO masking sequences inferred here on our CO-only tomographies are applicable to first order to real observations. Any deviation from the "real" optimal sequence is unlikely to affect the result significantly.

The optimal CO masking sequence as well as their impact on the CO PS as a function of masking depth is depicted in Fig. 9 at $k = 0.02 - 0.32$ Mpc^{-1}. By construction of our optimal CO masking sequence, the slopes of the lines connecting the CO PS as a function of masking depth starts by having negative values that get progressively less negative as the masking depth increase and so does the masking effectiveness, E. This trend of progressively less negative slope is, however, not always observed in this initial phase due to fact that the definition of E is scale independent and thus not tailored to the specific $k \approx 0.02 - 0.32$ Mpc^{-1} explored in Fig. 9. Overall, this figure demonstrates that in this

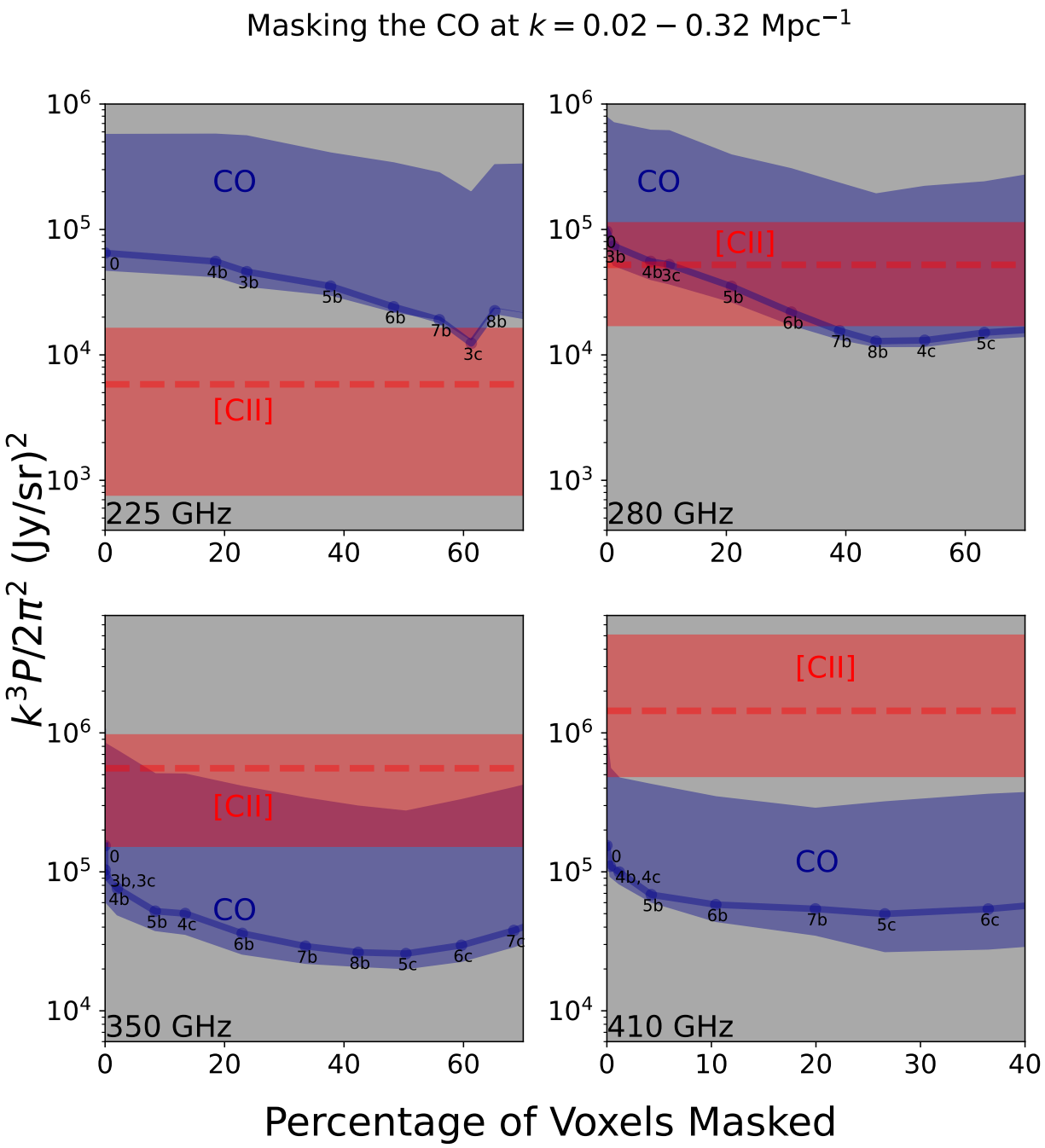

Fig. 9: Effect of masking on the CO-only PS. The range of PS between the "low-contamination" and "high-contamination" models (Sect. 2.3.2) at $k = 0.02 - 0.32$ Mpc^{-1} for CO lines (blue) is shown in relation to the percentage of voxels masked within the LIM tomographies for the frequency ranges of 225 ± 40 GHz (associated with $z_{[CII]} = 7.4$), 280 ± 40 GHz ($z_{[CII]} = 5.8$), 350 ± 40 GHz ($z_{[CII]} = 4.3$), and 410 ± 40 GHz ($z_{[CII]} = 3.7$). The lines represent the optimal CO masking sequence for our fiducial model, while each point and label indicate the J_{up} and subsample ("b" for "bright" and "c" for "complete") associated with the masking array applied. The same masking sequence is applied to the "low-contamination" and "high-contamination" models (Sect. 4.2.1). As an illustration and assuming at this stage that the mask does not affect the [CII] PS (but see Sect. 4.2.2), we show the fiducial and range of [CII] PS predictions in red.

initial phase, the decrease of the CO PS with masking depth is mostly driven at the high frequency bands by the masking of the CO $J_{up} = 3$ (for 350 ± 20 GHz) and $J_{up} = 4$ line (for 350 ± 20 GHz and 410 ± 20 GHz) which results in a 50% reduction of the CO PS. At the low frequency bands (225 ± 20 GHz and 280 ± 20 GHz) the decrease is more gradual, yielding to a reduction of one order of magnitude by masking all $J_{up} < 8$ lines.

As the masking process intensifies, a critical threshold is reached where the amplitude of the CO PS reaches a minimum value (hereafter called the optimal masking depth) and after which it rises despite the increasing masking depth. This oc-

curs when the CO line being masked contributes less to the total intensity of the tomography than the residual emissions from the brighter CO lines that have been masked previously. At this point, the mask begins to function akin to a random mask on the LIM tomography, as it is no longer targeting the brightest voxels. Moreover, since the intensity of the voxels follow a sparse, log-normal distribution (Sect. 4.2.3), this random masking results in the removal of more lower-intensity than high-intensity voxels. However, the correction we apply to the PS for the survey volume lost due to masking assumes that the intensity is uniformly distributed throughout the survey volume. This assumption of uniformity, although simplistic, is necessary because the non-homogeneity of the maps is model-dependent and cannot be accurately predicted without specific models. Nevertheless, it results in an increase in the amplitude of the PS when the mask does not follow the dominant galaxy population.

From Fig. 9, we note that the optimal masking depth as we move to higher frequency tomographies is reached at progressively lower masking depths (60%, 40%, 40% and 30% for the 225 GHz, 280 GHz, 350 GHz and 410 GHz accordingly). Comparing the amplitude of the CO PS at these optimal masking depths with that of the CII PS–assuming, at this stage, that it remains unaffected by the mask (but see Sect. 4.2.2 for further discussion)–allows us to preliminarily evaluate the feasibility of using this targeted masking approach to extract the CII PS signal. We find that in all frequency bands except for the 225 ± 40 GHz, the minimum fiducial CO PS is lower than the corresponding [CII] PS.

4.2.2. Impact of masking on the [CII] PS

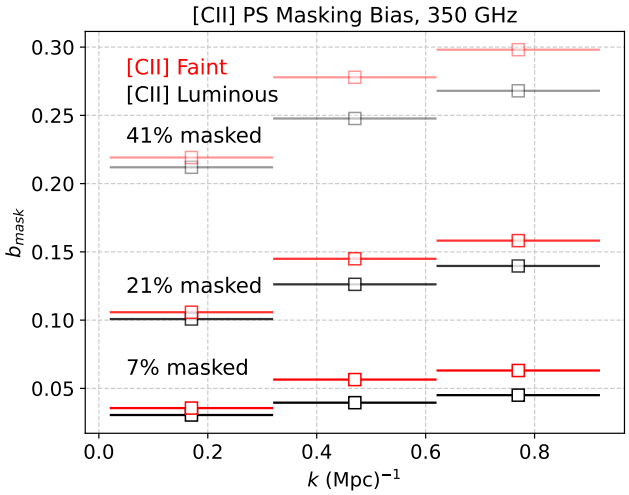

Fig. 10: Masking bias representing the relative difference in the PS between masked and unmasked [CII] tomographies for the 350 ± 20 GHz frequency band. Comparisons are made for the most pessimistic ("Faint", red lines) and optimistic ("Luminous", black lines) [CII] PS predictions for the masking depths of 7%, 21%, and 41% .

In the analysis carried out so far, we have assumed that masking does not affect the PS of the [CII] signal. In this section, we assess the validity of this assumption across different scales.

By examining the influence of the masking on the [CII] PS we deal with an issue already discussed in the context of the CO residuals (Sect. 4.2.1). Due to the sparsity of the signal, the masking is artificially boosting the [CII] PS. Unlike the case of the CO emission, where this effect becomes prominent only after a certain threshold, boosting of the [CII] PS commences from the onset of the masking procedure as the [CII] emission is invariably not correlated with the mask. This boosting of the [CII] PS can henceforth be seen as a bias introduced by the masking process, that contributes additional uncertainty to our analysis. We defined this masking bias, $b_{\rm mask}$, as the relative difference at a given scale between the PS amplitudes of the masked and unmasked [CII] tomographies, i.e.,

$$b_{\rm mask} = \left| \frac{P_{\rm masked} - P_{\rm unmasked}}{P_{\rm unmasked}} \right|. \quad (7)$$

We evaluated this scale-dependent bias using two extreme models for the [CII] tomography, that is, our model with the highest (hereafter "Luminous") and our model with the lowest [CII] PS signal ("Faint"; Fig 10). Then, we evaluated these biases for three masking scenarios, the "light" (7%), "moderate" (21%), and "deep" (41%). In Fig. 10, we present these results for the 350 ± 20 GHz tomography.

For the "light", "moderate", and "deep" scenarios, we find biases of ≈ 3%, ≈ 10%, and ≈ 22% at $k = 0.02 - 0.32$ Mpc^{-1} which increase to ≈ 6%, ≈ 15%, and ≈ 28% at $k = 0.62 - 0.92$, respectively. The scale dependence of the masking bias depends thus on the level of masking, and it intensifies as the masking becomes more aggressive. At the limiting case of of a masking depth of 41%, $b_{\rm mask}$ remains below 25% at large scales, but it can escalate to 30% at small scales. A similar scale-dependent bias is observed by Van Cuyck et al. (2023) in their angular [CII] PS predictions. This scale-dependent bias stems from the disparate impact of bright sources on the [CII] PS amplitude at different scales. On larger scales, the PS is predominantly influenced by the clustering signal of numerous star forming galaxies, which itself is proportional to the first moment of the luminosity function (Paper I). However, as we move to smaller scales, the PS is dominated by shot noise, which arises from the discrete nature of the luminous sources and is proportional to the second moment of the [CII] luminosity function (Paper I). At this scale the PS is thus strongly affected by the few, more luminous sources. The low probability of masking these rare bright sources leads to a significant masking bias due to volume corrections calculated assuming an homogeneous source distribution.

Inverting the masking process to correct for masking bias, i.e., de-convolving the masking array with the masked intensity maps, would require uncertain modeling of clustering components and could introduce artifacts when applied to a map with white noise, complicating the PS analysis. However, it should be noted that this scale-dependent, and sometimes significant, masking bias does not vary greatly (<5%) depending on the exact [CII] model used. This suggests that reliable scale-dependent corrections for this masking bias can be efficiently calculated using the specific masking strategies employed and [CII] models that are correct to first order. Of course, forward model fits to the observed [CII] PS will be able to account for this bias by construction.

4.2.3. Impact of Masking on the CO-Contaminated [CII] PS

We now turn our attention to assessing the impact of masking on the CO-contaminated [CII] PS, $P_{\rm (CO+[CII])}$, specifically within the $k = 0.02 - 0.32$ Mpc^{-1} range (Fig. 11). The masks are applied with the optimal sequence inferred using the CO-only tomographies shown in Fig. 9 (Sect. 4.2.1). Building upon the analysis

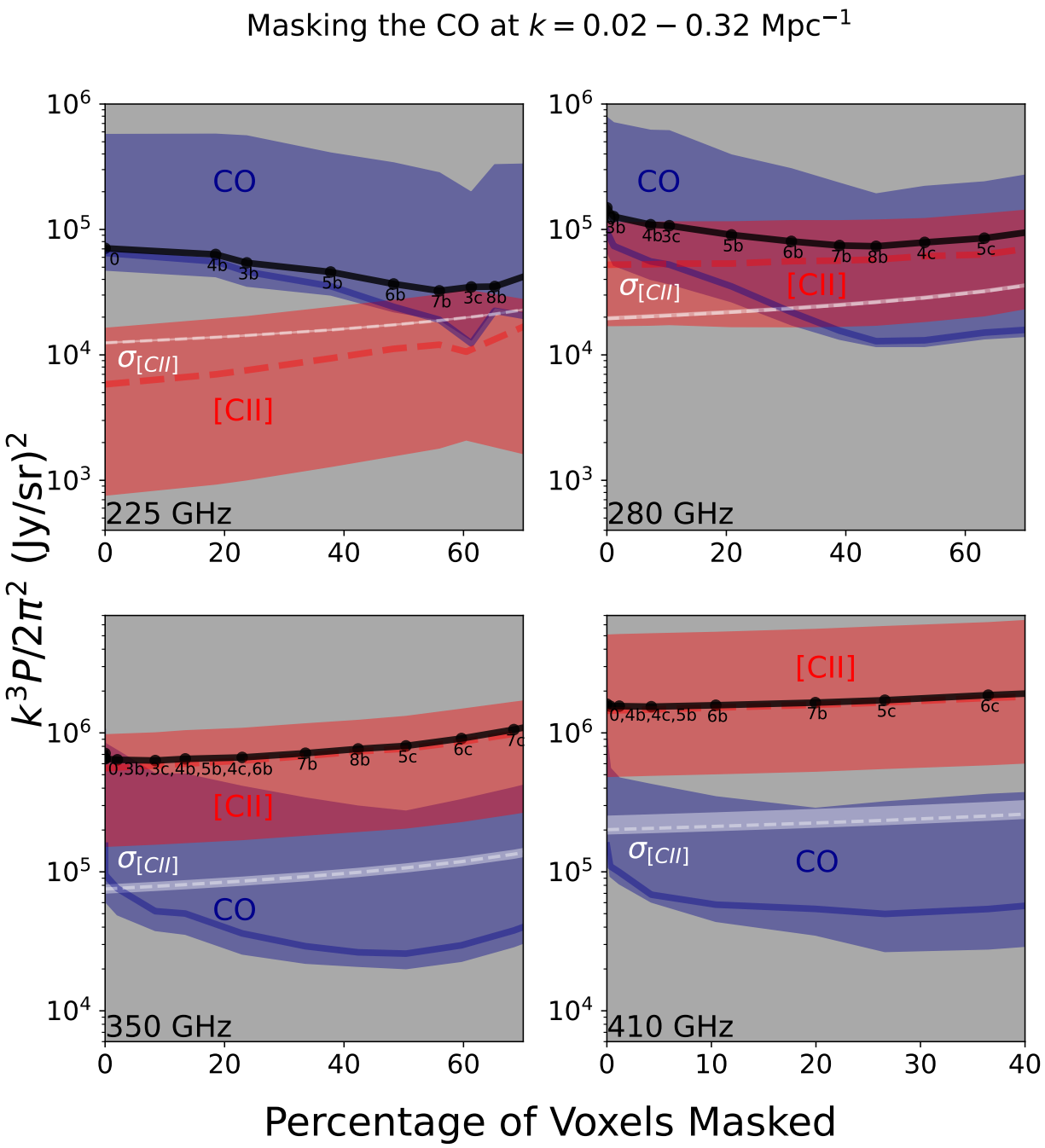

Fig. 11: Same plot as Fig. 9 but with the masking bias of [CII] taken into account. We also show the [CII] uncertainty ($\sigma_{[CII]}$, white line) and the total line (CO+[CII]) PS for the fiducial models (black line)

presented in Sect. 4.2.2, we include the bias introduced by masking on the [CII] signal, which translates into a gradual increase in the [CII] PS as masking depth increases. Finally, as a last piece of information, the uncertainty associated with the [CII] PS for a 2000-hour FYST survey, denoted as $\sigma_{[CII]}$, is plotted in Fig. 11 as well. This uncertainty, encompassing both instrumental white noise and sample variance, is defined in Paper I by the equation:

$$\sigma_{[CII]} = \frac{P_{[CII]}(k,z) + P_N}{\sqrt{N_m(k)}}. \quad (8)$$

Assuming that the distribution of masked voxels is uniform, this uncertainty increases with the masking depth proportionally to the decrease in the number of k-modes across all k-bins. A Monte Carlo algorithm validated this uniformity assumption, establishing a consistent relationship across all scales we examined:

$$\frac{\sigma[\mathrm{CII}]}{\sigma[\mathrm{CII}],\,\mathrm{masked}} = \sqrt{\frac{N_{k,\,\mathrm{not\ masked}}}{N_k}} = \sqrt{\frac{N_{\mathrm{voxels,\ not\ masked}}}{N_{\mathrm{voxels}}}}. \quad (9)$$

By integrating all the elements presented in Fig. 11, we can assess whether the objective of masking has been achieved, that is, to reduce the amplitude of the CO PS below the measurement uncertainty of the [CII] PS ($\sigma_{[CII]}$), while ensuring that this uncertainty remains below the amplitude of the [CII] PS. Two distinct cases are evident in Fig. 11. Firstly, in the higher frequency bands (350 ± 20 and 410 ± 20 GHz), $P_{(CO+[CII])}$ initially undergoes a slight decrease at masking depths of < 10%, attributed to the masking of the rare but bright $J_{up} = 3$ and $J_{up} = 4$ sources, immediately followed by a gradual increase, mainly due to the [CII] PS masking bias (the CO PS masking bias only playing a role at masking depths > 20%). As already mentioned, since the [CII] emission is invariably uncorrelated with the mask, such an increase in PS from the onset of the masking procedure is characteristic of the dominance of the [CII] signal in the unmasked tomography. At these high-frequency and at the optimal masking depth of < 10%, the [CII] signal dominates and, more importantly, it is well above σ_{CII}. This guarantees accurate detection of the [CII] PS by the FYST LIM survey in these bands. Secondly, in the lower frequency bands (225 ± 20 and 280 ± 20 GHz), $P_{(CO+CII)}$ decreases progressively with masking depth, reaches a minimum at the optimal masking depth of $\approx 40 - 60\%$ and finally increases due to a combination of CO and [CII] masking biases. At 280 ± 20 GHz, the decrease in $P_{(CO+CII)}$ is less pronounced than at 225 ± 20 GHz, and in the former case, the masked tomography effectively switches from CO-dominant to [CII]-dominant, whereas in the latter case, the masked tomography remains CO-dominant. At 280 ± 20 GHz, and at the optimal masking depth of 40%, the [CII] signal dominates and lies above σ_{CII}. FYST LIM will thus detect, albeit marginally, the [CII] PS in this band (signal-to-noise ratio of two and CO contamination of around 15%). In contrast, at 225 ± 20 GHz and at optimal masking depth of 60%, the CO signal still dominates. In this band, an alternative masking approach will be required.

From the observational point of view, the results of Fig. 11 make clear that for a real dataset, the evolution of the PS as function of the masking depth and the location of the optimal masking depth provide key insights into the initial contamination levels of the tomography. A very low value for the optimal masking depth ($\lesssim 10\%$), associated with an amplified PS as we surpass this threshold, unambiguously indicates the predominance of [CII] in the initial tomography. In contrast, a value of the optimal masking depth greater than $\gtrsim 10\%$ indicates the dominance by CO foregrounds in the initial tomography. In this case, accurately assessing the extent of CO contamination at the optimal masking depth is challenging in a real dataset as no clear signatures are visible in the PS and as the [CII] and CO emitters share similar spatial frequency characteristics, complicating their differentiation in Fourier space.

Separation between the [CII] and CO emitters becomes clearer when analyzing how these populations contribute to the average total power of the signal. Specifically, this can be achieved by examining their contributions to the zero displacement of the PS from constructing a histogram that represents the distribution of squared voxel intensities, each weighted by its own squared intensity (Fig. 12). It is crucial to note, however, that in order to create this histogram, knowledge of the absolute intensity of the tomography is needed, while this information is partially lost by our atmospheric and astrophysical continuum foregrounds removal. To estimate a posteriori the magnitude of the mean intensity, we used the PS value at large scales, since we demonstrated in Paper I that $\boldsymbol{k^3 P_{clustering}(k \approx 10^{-2}\ Mpc^{-1}) \approx I^2_{mean}}$.

Equipped with this proxy for the mean intensity, we can generate a weighted histogram of the tomography, masked to the optimal depth. When this histogram displays two peaks instead of one, it signifies a transition from a CO-dominated to a [CII]-dominated tomography, achieved by eliminating the brighter CO sources. Conversely, the presence of a single peak signifies that the tomography remains CO-dominated, primarily by the less intense CO sources that were not masked in earlier iterations. Fig. 12 illustrates these two cases for the 280 ± 20 GHz tomography. For the first case we considered our fiducial [CII] and CO PS whereas for the second we combined our fiducial [CII] with our most pessimistic CO PS predictions. For the first case of the fiducial CO PS, as we increase the masking depth, a secondary peak emerges at the brighter end of the histogram, corresponding to the population of [CII] emitters. Notably, at the optimal masking depth, these two peaks have similar heights, marking the transition from CO dominance to [CII] dominance in the PS of this masked tomography. This emergence and predominance of this secondary peak thus signifies the success of the masking process at the optimal masking depth. On the contrary, in the second case, even at the optimal masking depth, the [CII] peak remains hidden in the bright tail of the CO peak. This single-peak histogram, which moves only towards lower voxel intensities as the masking depth increases, signifies the failure of the masking process at the optimal masking depth.

Unfortunately, this rather simple method to distinguish CO-dominated from CII-dominated tomography at the optimal masking depth is strongly affected by the presence of white noise. For example, considering the white noise of the plane 2000 hours of the FYST LIM survey, the peak(s) of the weighted histogram is entirely hidden by it (Fig. 12). Nevertheless, with five times deeper observations, the white noise distribution moves enough towards fainter voxels ($I^2_{vox} < 10^4 (Jy/sr)^2$) allowing us to identify the emergence of the [CII]-related secondary peak at $I^2_{vox} > 10^4 (Jy/sr)^2$. This white noise distribution effectively acts as a threshold on the x-axis, below which observations become indiscernible.

In essence, our technique unfolds in two steps. We begin by incrementally masking the LIM tomography until we identify the point where the PS at $k = 0.02 - 0.32$ Mpc^1 is minimized, revealing the optimal depth for masking. Following this, we examine the weighted voxel histogram of the tomography masked to this depth. In this histogram –which is calibrated using the PS measurement and weighted by the square of the voxel intensities– we look for a bimodal distribution as confirmation of successful [CII] signal isolation.

5. Discussion

This study aimed to quantify the contamination of the (post-)EoR [CII] LIM signal by foreground CO emissions for the upcoming FYST LIM survey, utilizing post-processing of the TNG300 hydrodynamical simulation. The strength of our approach lies in its capacity to generate a range of predictions that account for the inherent uncertainties in CO luminosity functions (Riechers et al. 2019; Decarli et al. 2020), and for variations in the CO SLED of galaxies. Based on these predictions, we assessed the effectiveness of a masking technique that leverages an external catalog to identify and subsequently mask bright CO emitters. This led to the identification of a method to determine the optimal masking depth and a novel indicator for successful CO foreground removal.

Our analysis revealed significant variations in CO contamination across different frequency bands of the EoR-Spec, with

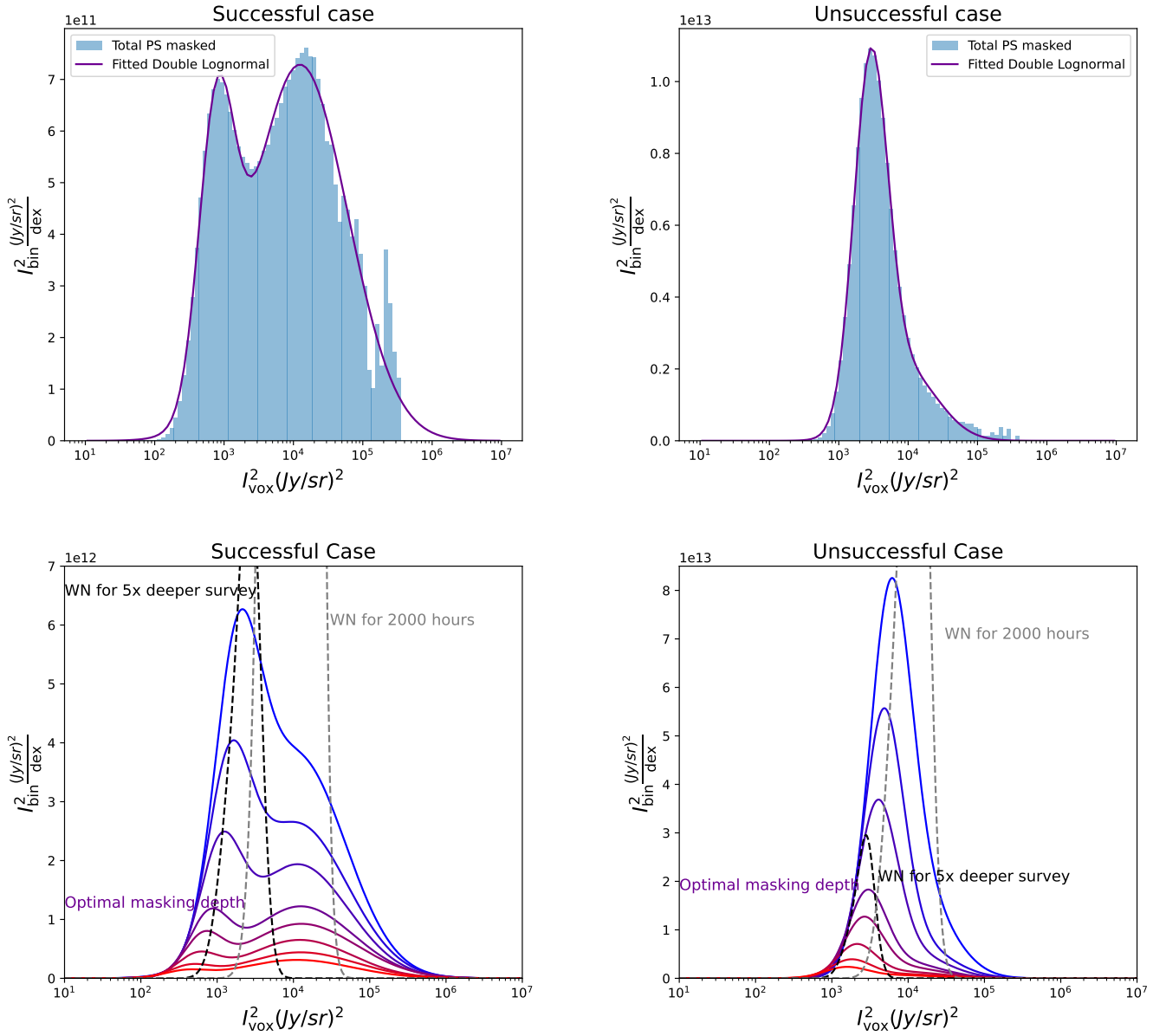

Fig. 12: Pixel distribution histograms weighted with the voxel intensity squared, illustrating the distinction between successful (left; fiducial CO) and unsuccessful (right; pessimistic CO) cases of CO masking of the FYST 280 ± 20 GHz tomography. The top panels show the weighted voxel histograms of these 280 ± 20 GHz tomography masked to the optimal depth and fitted double lognormal distributions. The lower panels detail the progressive masking depth, each curve representing the lognormal fits of the weighted histogram at increasing depth. This highlights the emergence of a bimodal distribution in the successful case versus a single peak distribution in the unsuccessful case. The lognormal fit to the weighted histogram of a white noise tomography equivalent to the upcoming 2000 hours FYST LIM (black dashed line) and a fit to the white noise tomography of a survey 5 times deeper (gray dashed line) are superimposed.

notably lower contamination at higher frequencies. This variation significantly impacts the efficiency of our masking technique, which shows greater effectiveness at frequencies where initial contamination is lower. Specifically, we found that the targeted [CII] signal could be detected with minimal masking and thus minimal masking bias at 410 GHz and 350 GHz (Fig. 13). In contrast, at 280 GHz and particularly at 225 GHz, our simple CO masking technique faced challenges due to the high level of foreground CO emissions, underscoring the need for alternative strategies at these frequencies.

Our work aligns with the efforts of Van Cuyck et al. (2023) performed in the framework of the CONCERTO experiment, which similarly aimed to test via simulation the extraction of the [CII] signal from the (post-)EoR universe using a comparable masking strategy. Despite the challenges in making direct comparisons due to differences in angular and spectral resolution, both studies highlight the limitations of masking strategies at high redshifts, especially beyond $z \geq 6.5$. This consensus emphasizes the complexities of masking strategies and their variable effectiveness across redshift. Diverging from Van Cuyck et al. (2023), we chose to exclude the [CI] line from our simu-

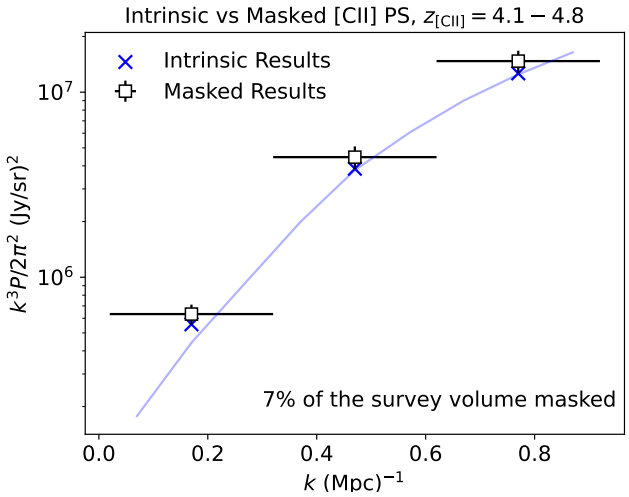

Fig. 13: Comparison of the [CII] PS for [CII] observations in the redshift range $z_{[CII]} = 4.1 - 4.8$. The squares denote the combined CO+[CII] PS after masking CO bright voxels, resulting in a 7% reduction in survey volume. The associated error bars on the squares capture the uncertainty in [CII] measurements due to white instrumental noise and sample variance. The blue crosses depict the intrinsic [CII] PS results, binned at the same Δk. The continuous line represents the intrinsic [CII] PS results but with a finer binning.

lations due to its highly uncertain intensity values, aligning with methodologies like those suggested by Yue & Ferrara (2019). The absence of [CI] contamination in our simulations is probably largely compensated by the very wide range of CO models, including very pessimistic ones, taken into account in our study. The precise impact of [CI] lines, along with other foregrounds, is expected to be clarified with the advent of first light science observations.

A notable limitation of our study, also highlighted by Gkogkou et al. (2023) and Van Cuyck et al. (2023), concerns the impact of sample variance, of both the CO and [CII] emitters. Our reliance on the single realization of the TNG300 simulation introduces a potential limitation in terms of the accuracy of our results. Nonetheless, given the wide range of models considered in our simulation, we assume that the influence of sample variance on the effectiveness of our masking technique is relatively minor. Nevertheless, recognizing that sample variance could pose a significant challenge in the context of future forward modeling of the [CII] LIM observations, we will explore the development of multiple realizations of wide observational cones by employing machine learning techniques (Garcia et al. 2023).

Our decontamination method itself comes with its limitations. Despite its reliability, informed masking is not the most efficient technique, particularly in terms of survey volume loss, at low frequencies. The challenge remains to develop more refined techniques, that de-confuse the line PS without the cost of losing survey volume. There are several mathematically elegant techniques that could achieve this goal. One such approach would be utilizing the wide frequency coverage of the EoR-Spec to measure the CO PS indirectly from the measurements of the cross-correlation of three lines coming from the same galaxies, leveraging the statistical independence of the rest of the line-components. Another approach involves exploiting the anisotropic nature of the 2D PS of interloper lines (Cheng et al. 2016). Upon projection on the frame of reference of the targeted line, the PS of these interloper lines exhibits distinct anisotropies that can be used to differentiate between the target signal and the foreground contamination. Both approaches are promising, yet they share the limitation of failing to recover the valuable Fourier phase information, which is essential for analyzing histograms related to voxel intensity distribution. A third approach that recaptures the Fourier phase information is using conditional generative adversarial networks to de-confuse the signals at the map level rather than at the PS level. Moriwaki et al. (2020) focused on de-confusing two lines (Hα and OIII), using a large set of simulated data for training their models. Although this approach is expected to be very effective, it is challenging to estimate the uncertainties involved in the de-confusion method of the measurements. Finally, it is worth noting the existence of a fourth approach that is more robust against the model uncertainty and still recaptures the phase information and that relies on the identification and extraction of foreground sources that are characterized by multiple interloping emission lines. This can be done by fitting multiple SLED templates to each line-of-sight of the tomography using the sparse approximation (Cheng et al. 2020). Given the wide frequency range of the EoR-Spec, we consider this method to be the most promising alternative approach beyond targeted masking. This approach will be tested and evaluated in the context of the FYST LIM survey on the third part of our paper series.

While line foregrounds present significant challenges, the importance of atmospheric and astrophysical continuum foregrounds should not be overlooked. Although Van Cuyck et al. (2023) successfully applied the asymmetric re-weighted penalized least-squares technique to remove contamination from the cosmic infrared background, reinforcing our focus on line interlopers as the primary challenge at low frequencies (225 ± 20 GHz, 280 ± 20 GHz), the issue of atmospheric foregrounds remains unresolved and may only be addressed through the use of mock detector data streams. Unfortunately, it is at the high frequencies (350±20 GHz, 410±20 GHz), where CO contamination is not problematic that we expect atmospheric contamination to play a critical role. This juxtaposition makes atmospheric interference potentially the primary barrier to detection at the two higher frequency bands of FYST LIM survey.

6. Conclusion

Our study evaluated the level of contamination from CO rotational line emission when observing the (post-)EoR [CII] PS using the upcoming FYST LIM survey and presented a method for mitigating it. We created mock tomographies of the CO line emitters by post-processing the TNG300 simulation, accounting for the inherent uncertainties in the observed CO luminosity functions and the observed CO SLEDs. The resulting range of CO predictions is in good agreement with the ASPECS observations.

Our analysis revealed that the total mean intensity of CO emissions remains relatively constant, at approximately 1000 Jy/sr, across the observed frequency spectrum. This emission predominantly originates from low-J CO transitions ($J_{up} < 8$) in galaxies at lower redshifts ($z < 2$). In contrast, the [CII] mean intensity exhibits a significant upward trend, increasing from about 10 Jy/sr at 225 GHz to 2000 Jy/sr at 410 GHz, making the [CII] the dominant emission line at frequencies above 364 GHz.

Based on these predictions, we assessed a foreground removal strategy that involves identifying and masking voxels containing bright CO emitters, utilizing mock external catalogs that exhibit realistic features. A key aspect of our analysis was the determination of mask effectiveness, which we defined as the ability of a mask to reduce the standard deviation of the intensity of the signal, normalized by the number of voxels masked. Through iterative application and reassessment of these masks on CO-only tomography, we were able to refine our masking sequence to achieve optimal foreground removal. The optimal sequence for CO masks found here is broadly applicable to real observations, as we see very little variation into this sequence across the broad range of CO model considered here.

Our analysis also highlighted the frequency dependency of the optimal masking depth, which aligns with the point where the PS of the masked tomography reaches its minimum. While less than 10% masking depth is required at higher frequencies (350 ± 20 GHz and 410 ± 20 GHz), a deeper masking of more than 40% is necessary at lower frequencies (280 ± 20 GHz and 225 ± 20 GHz).

At these masking depths, according to our fiducial models, [CII] emission dominates and significantly exceeds the typical instrumental white noise levels at higher frequencies, ensuring a robust detection of the [CII] PS at 350 ± 20 GHz and 410 ± 20 GHz. A tentative detection is also expected at 280 ± 20 GHz, where [CII] marginally prevails over CO contamination. However, at 225 ± 20 GHz, despite deep masking, CO contamination continues to overshadow [CII] emission, highlighting the urgent need for advanced decontamination techniques.

While estimating the optimal masking depth for decontaminating a real LIM tomography is relatively straightforward, discerning the levels of decontamination achieved at this depth presents a more complex challenge. This complexity arises because CO and [CII] emitters share similar spatial frequency characteristics, making it difficult to distinguish between the two solely based on their distribution in Fourier space. A practical solution involves creating a weighted voxel histogram, where each voxel is weighted by the square of its intensity and the histogram is calibrated using the PS measurement of the tomography masked at the optimal depth. Detailed examination of this histogram for signs of bimodality can reveal a successful transition from a CO-dominated to a [CII]-dominated state. This method will, however, only be applicable to data with very low instrumental white noise, about five times lower than that anticipated for 2000 hours of observation with the EoR-Spec.

Our study lays the groundwork for future LIM studies into the high-redshift universe. The development of decontamination techniques capable of extracting the [CII] high-redshift signal as well as the detailed modeling of the astrophysical and atmospheric foregrounds suitable for forward modeling are the necessary next steps.

Acknowledgements. We thank Dongwoo Chung, Patrick Breysse, Yoko Okada, Anirban Roy, Steve Choi, Eiichiro Komatsu, Thoma Nikola, Reinhold Schaaf, Ralf Antonius Timmermann, Kaustuv moni Basu, Vyoma Muralidhara, Maude Charmetant, Nicholas Battaglia, Gordon Stacey and other members of the CCAT science working group for detailed discussions about EoR-Spec; We are grateful to Matthieu Bethermin, Athanasia Gkogkou, Mathilde Van Cuyck, Desika Narayanan, Anthony Pullen, Sylvia Adscheid, Elena Marcuzzo, Prachi Khatri, Benedetta Spina, and Cristiano Porciani for the helpful discussions. This research was carried out within the Collaborative Research Center 956 (project ID 184018867), sub-projects A1 and C4 and within the Collaborative Research Center 1601 (project ID 500700252), sub-projects C3 and C6, funded by the Deutsche Forschungsgemeinschaft (DFG). This research made use of NASA's Astrophysics Data System Bibliographic Services; Matplotlib (Hunter 2007); Astropy, a community-developed core Python package for astronomy (Astropy Collaboration et al. 2013); PlotDigitizer (http://plotdigitizer.sourceforge.net/).

References

Aihara, H., Armstrong, R., Bickerton, S., et al. 2018, PASJ, 70, S8
Aravena, M., Spilker, J. S., Bethermin, M., et al. 2016, MNRAS, 457, 4406
Astropy Collaboration, Robitaille, T. P., Tollerud, E. J., et al. 2013, A&A, 558, A33
Barkana, R. & Loeb, A. 2001, Phys. Rep., 349, 125
Becker, G. D., Bolton, J. S., & Lidz, A. 2015, PASA, 32, e045
Becker, R. H., Fan, X., White, R. L., et al. 2001, AJ, 122, 2850
Bernal, J. L. & Kovetz, E. D. 2022, A&A Rev., 30, 5
Béthermin, M., Fudamoto, Y., Ginolfi, M., et al. 2020, A&A, 643, A2
Béthermin, M., Gkogkou, A., Van Cuyck, M., et al. 2022, A&A, 667, A156
Boogaard, L. A., Decarli, R., Walter, F., et al. 2023, ApJ, 945, 111
Boogaard, L. A., van der Werf, P., Weiss, A., et al. 2020, ApJ, 902, 109
Bouwens, R. J., Illingworth, G. D., Oesch, P. A., et al. 2015, ApJ, 803, 34
Bouwens, R. J., Smit, R., Labbé, I., et al. 2016, ApJ, 831, 176
Bouwens, R. J., Smit, R., Schouws, S., et al. 2022, ApJ, 931, 160
Boylan-Kolchin, M., Weisz, D. R., Johnson, B. D., et al. 2015, MNRAS, 453, 1503
Breysse, P. C., Kovetz, E. D., & Kamionkowski, M. 2015, MNRAS, 452, 3408
Carilli, C. L. & Walter, F. 2013, ARA&A, 51, 105
Cassata, P., Liu, D., Groves, B., et al. 2020, ApJ, 891, 83
CCAT-Prime Collaboration, Aravena, M., Austermann, J. E., et al. 2023, ApJS, 264, 7
Cheng, Y.-T., Chang, T.-C., Bock, J., Bradford, C. M., & Cooray, A. 2016, ApJ, 832, 165
Cheng, Y.-T., Chang, T.-C., & Bock, J. J. 2020, ApJ, 901, 142
Chung, D. T., Breysse, P. C., Cleary, K. A., et al. 2022, ApJ, 933, 186
Clarke, J., Karoumpis, C., Riechers, D., et al. 2024, arXiv e-prints, arXiv:2404.05352
CONCERTO Collaboration, Ade, P., Aravena, M., et al. 2020, A&A, 642, A60
Conselice, C. J., Wilkinson, A., Duncan, K., & Mortlock, A. 2016, ApJ, 830, 83
Daddi, E., Dannerbauer, H., Liu, D., et al. 2015, A&A, 577, A46
Davé, R., Crain, R. A., Stevens, A. R. H., et al. 2020, MNRAS, 497, 146
De Looze, I., Cormier, D., Lebouteiller, V., et al. 2014, A&A, 568, A62
Decarli, R., Aravena, M., Boogaard, L., et al. 2020, ApJ, 902, 110
Decarli, R., Walter, F., Aravena, M., et al. 2016, ApJ, 833, 70
den Brok, J. S., Chatzigiannakis, D., Bigiel, F., et al. 2021, MNRAS, 504, 3221
Downes, D. & Solomon, P. M. 1998, ApJ, 507, 615
Dragone, C. 1978, AT T Technical Journal, 57, 2663
Elbaz, D., Daddi, E., Le Borgne, D., et al. 2007, A&A, 468, 33
Euclid Collaboration, Desprez, G., Paltani, S., et al. 2020, A&A, 644, A31
Euclid Collaboration, Ilbert, O., de la Torre, S., et al. 2021, A&A, 647, A117
Euclid Collaboration, Moneti, A., McCracken, H. J., et al. 2022, A&A, 658, A126
Fan, X., Strauss, M. A., Richards, G. T., et al. 2006, AJ, 131, 1203
Garcia, K., Narayanan, D., Popping, G., et al. 2023, arXiv e-prints, arXiv:2311.01508
Gkogkou, A., Béthermin, M., Lagache, G., et al. 2023, A&A, 670, A16
Harikane, Y., Inoue, A. K., Mawatari, K., et al. 2022, ApJ, 929, 1
Huber, Z. B., Choi, S. K., Duell, C. J., et al. 2022, in Society of Photo-Optical Instrumentation Engineers (SPIE) Conference Series, Vol. 12190, Millimeter, Submillimeter, and Far-Infrared Detectors and Instrumentation for Astronomy XI, ed. J. Zmuidzinas & J.-R. Gao, 121902H
Hunter, J. D. 2007, Computing in Science & Engineering, 9, 90
Kaasinen, M., Scoville, N., Walter, F., et al. 2019, ApJ, 880, 15
Kamenetzky, J., Rangwala, N., & Glenn, J. 2017, MNRAS, 471, 2917
Karoumpis, C., Magnelli, B., Romano-Díaz, E., Haslbauer, M., & Bertoldi, F. 2022, A&A, 659, A12
Kennicutt, Robert C., J. 1998, ARA&A, 36, 189
Kim, J. 2011, A&A, 531, A32
Kogut, A., Dwek, E., & Moseley, S. H. 2015, ApJ, 806, 234
Kovetz, E., Breysse, P. C., Lidz, A., et al. 2019, BAAS, 51, 101
Lagache, G., Cousin, M., & Chatzikos, M. 2018, A&A, 609, A130
Laigle, C., McCracken, H. J., Ilbert, O., et al. 2016, ApJS, 224, 24
Le Fèvre, O., Béthermin, M., Faisst, A., et al. 2020, A&A, 643, A1
Lehmer, B. D., Brandt, W. N., Alexander, D. M., et al. 2005, ApJS, 161, 21
Lenkić, L., Bolatto, A. D., Förster Schreiber, N. M., et al. 2020, AJ, 159, 190
Madau, P. & Dickinson, M. 2014, ARA&A, 52, 415
Magdis, G. E., Gobat, R., Valentino, F., et al. 2021, A&A, 647, A33
Magnelli, B., Boogaard, L., Decarli, R., et al. 2020, ApJ, 892, 66
Mashian, N., Sturm, E., Sternberg, A., et al. 2015, ApJ, 802, 81
Moriwaki, K., Filippova, N., Shirasaki, M., & Yoshida, N. 2020, MNRAS[arXiv:2002.07991]
Moriwaki, K. & Yoshida, N. 2021, ApJ, 923, L7
Narayanan, D. & Krumholz, M. R. 2014, MNRAS, 442, 1411
Parshley, S. C., Niemack, M., Hills, R., et al. 2018, in Society of Photo-Optical Instrumentation Engineers (SPIE) Conference Series, Vol. 10700, Ground-based and Airborne Telescopes VII, ed. H. K. Marshall & J. Spyromilio, 1070041

Peebles, P. J. E. 1968, ApJ, 153, 1
Perot, A. & Fabry, C. 1899, ApJ, 9, 87
Pillepich, A., Nelson, D., Springel, V., et al. 2019, MNRAS, 490, 3196
Pillepich, A., Springel, V., Nelson, D., et al. 2018, MNRAS, 473, 4077
Ponthieu, N., Grain, J., & Lagache, G. 2011, A&A, 535, A90
Popping, G., Pillepich, A., Somerville, R. S., et al. 2019, ApJ, 882, 137
Pullen, A. R., Breysse, P. C., Oxholm, T., et al. 2023, MNRAS, 521, 6124
Riechers, D. A., Boogaard, L. A., Decarli, R., et al. 2020, ApJ, 896, L21
Riechers, D. A., Pavesi, R., Sharon, C. E., et al. 2019, ApJ, 872, 7
Roy, A., Valentín-Martínez, D., Wang, K., Battaglia, N., & van Engelen, A. 2023, ApJ, 957, 87
Schaerer, D., Ginolfi, M., Béthermin, M., et al. 2020a, A&A, 643, A3
Schaerer, D., Ginolfi, M., Béthermin, M., et al. 2020b, A&A, 643, A3
Scoville, N., Lee, N., Vanden Bout, P., et al. 2017, ApJ, 837, 150
Seager, S., Sasselov, D. D., & Scott, D. 2000, ApJS, 128, 407
Shannon, C. 1949, Proceedings of the IRE, 37, 10
Silich, S., Tenorio-Tagle, G., Torres-Campos, A., et al. 2009, ApJ, 700, 931
Silva, M., Santos, M. G., Cooray, A., & Gong, Y. 2015, ApJ, 806, 209
Solomon, P. M. & Vanden Bout, P. A. 2005, ARA&A, 43, 677
Stacey, G. J., Geis, N., Genzel, R., et al. 1991, ApJ, 373, 423
Sun, G., Chang, T. C., Uzgil, B. D., et al. 2021, ApJ, 915, 33
Sun, G., Moncelsi, L., Viero, M. P., et al. 2018, ApJ, 856, 107
Tacconi, L. J., Genzel, R., Saintonge, A., et al. 2018, ApJ, 853, 179
Valentino, F., Daddi, E., Puglisi, A., et al. 2020, A&A, 641, A155
Vallini, L., Gallerani, S., Ferrara, A., Pallottini, A., & Yue, B. 2015, ApJ, 813, 36
Van Cuyck, M., Ponthieu, N., Lagache, G., et al. 2023, arXiv e-prints, arXiv:2306.01568
Vavagiakis, E. M., Ahmed, Z., Ali, A., et al. 2018, in Society of Photo-Optical Instrumentation Engineers (SPIE) Conference Series, Vol. 10708, Millimeter, Submillimeter, and Far-Infrared Detectors and Instrumentation for Astronomy IX, ed. J. Zmuidzinas & J.-R. Gao, 107081U
Venemans, B. P., Findlay, J. R., Sutherland, W. J., et al. 2013, ApJ, 779, 24
Vieira, J., Aguirre, J., Bradford, C. M., et al. 2020, arXiv e-prints, arXiv:2009.14340
Wang, T.-M. & Hwang, C.-Y. 2020, A&A, 641, A24
Wang, T.-M., Magnelli, B., Schinnerer, E., et al. 2022, A&A, 660, A142
Weaver, J. R., Kauffmann, O. B., Ilbert, O., et al. 2022, ApJS, 258, 11
Wilson, D., Cooray, A., Nayyeri, H., et al. 2017, ApJ, 848, 30
Yue, B. & Ferrara, A. 2019, MNRAS, 490, 1928
Yue, B., Ferrara, A., Pallottini, A., Gallerani, S., & Vallini, L. 2015, MNRAS, 450, 3829
Zaroubi, S. 2013, Astrophysics and Space Science Library, Vol. 396, The Epoch of Reionization, ed. T. Wiklind, B. Mobasher, & V. Bromm, 45
Zel'dovich, Y. B., Kurt, V. G., & Syunyaev, R. A. 1969, Soviet Journal of Experimental and Theoretical Physics, 28, 146
Zhou, X., Gong, Y., Deng, F., et al. 2023, MNRAS, 521, 278
Zou, B., Choi, S. K., Cothard, N. F., et al. 2022, in Society of Photo-Optical Instrumentation Engineers (SPIE) Conference Series, Vol. 12190, Millimeter, Submillimeter, and Far-Infrared Detectors and Instrumentation for Astronomy XI, ed. J. Zmuidzinas & J.-R. Gao, 121902B

A. Impact of masking on the PS of individual CO lines

This appendix presents the PS of individual CO ($J_{\rm up} = 3 - 8$) spectral lines in the frame of reference of the [CII] line at scales of $k = 0.02 - 0.32$ Mpc^{-1} as a function of the percentage of the survey volume masked (Fig. A1) following the optimal masking sequence described in Sect. 4.2. For each CO line PS, two distinct behaviors are observed during the masking process. When the masking step specifically targets the spectral line in question, there is a sharp decrease in the PS. Conversely, when the masking step targets a different spectral line, a slow increase in the PS is observed due to the masking bias (see Sect. 4.2.2).

The behavior of the PS during masking is influenced by how the galaxies emitting the lines are distributed within the 3D tomography. Lines from galaxies that are highly localized within the survey volume, such as CO(3-2) at 350 GHz, exhibit a sharp decrease in their PS when masking targets them. Additionally, there is almost no increase in PS when masking targets other lines due to the minimal residuals left after masking. In contrast, lines from galaxies more evenly distributed throughout the survey volume, such as CO(4-3) at 225 GHz, show a less pronounced decrease in PS when masked, but a stronger increase when other lines are masked, because there remains a substantial amount of residual emission that gets amplified. A key indicator of how uniformly the intensity of each line is distributed in the tomography is the CV of its intensity, as shown in Fig. 8 and described in detail in Sect. 4.1.

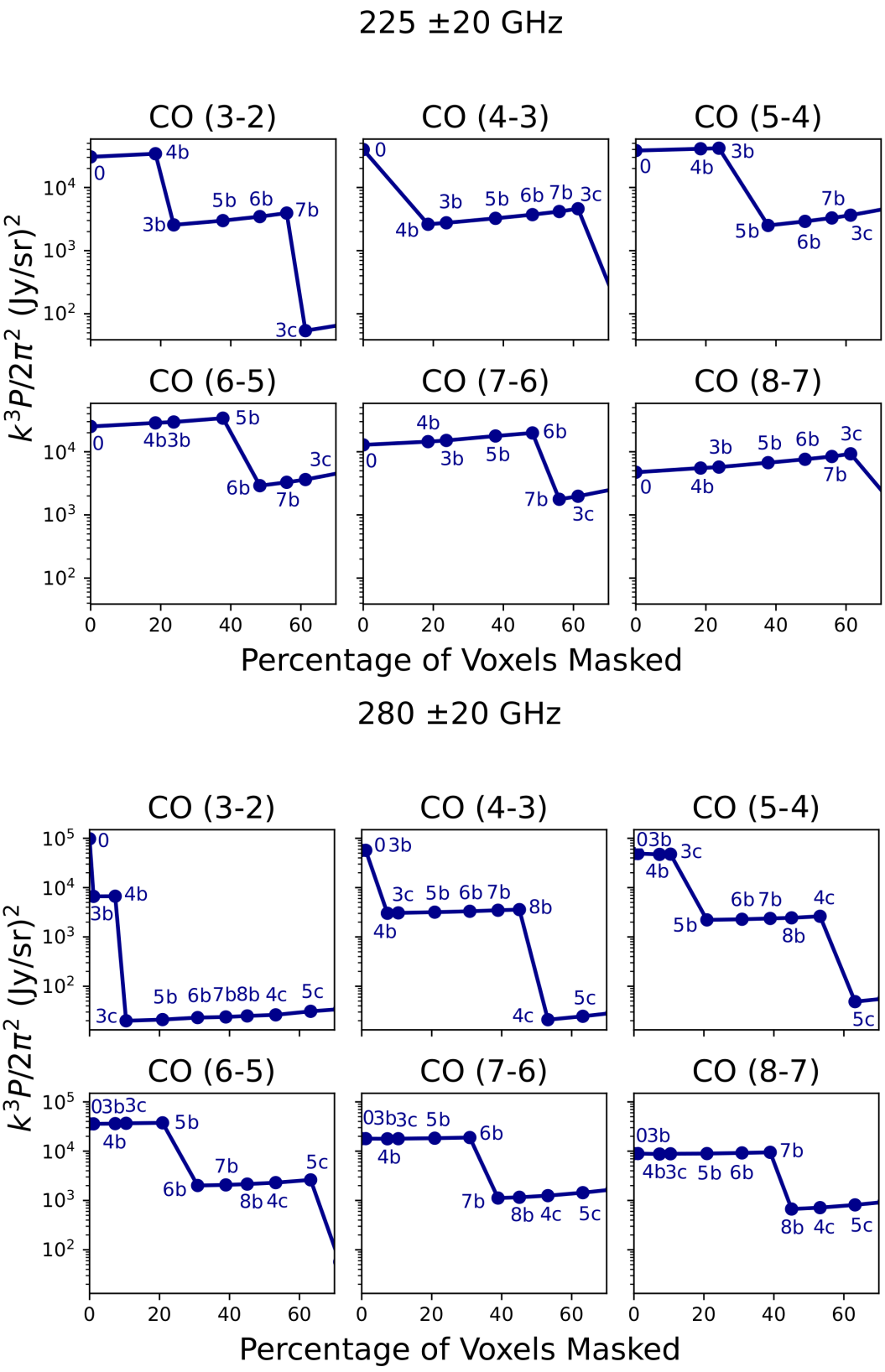
225 ±20 GHz
CO (3-2)
CO (4-3)
CO (5-4)
CO (6-5)
CO (7-6)
CO (8-7)
$k^3P/2\pi^2$ (Jy/sr)^2
Percentage of Voxels Masked
280 ±20 GHz
CO (3-2)
CO (4-3)
CO (5-4)
CO (6-5)
CO (7-6)
CO (8-7)
$k^3P/2\pi^2$ (Jy/sr)^2
Percentage of Voxels Masked

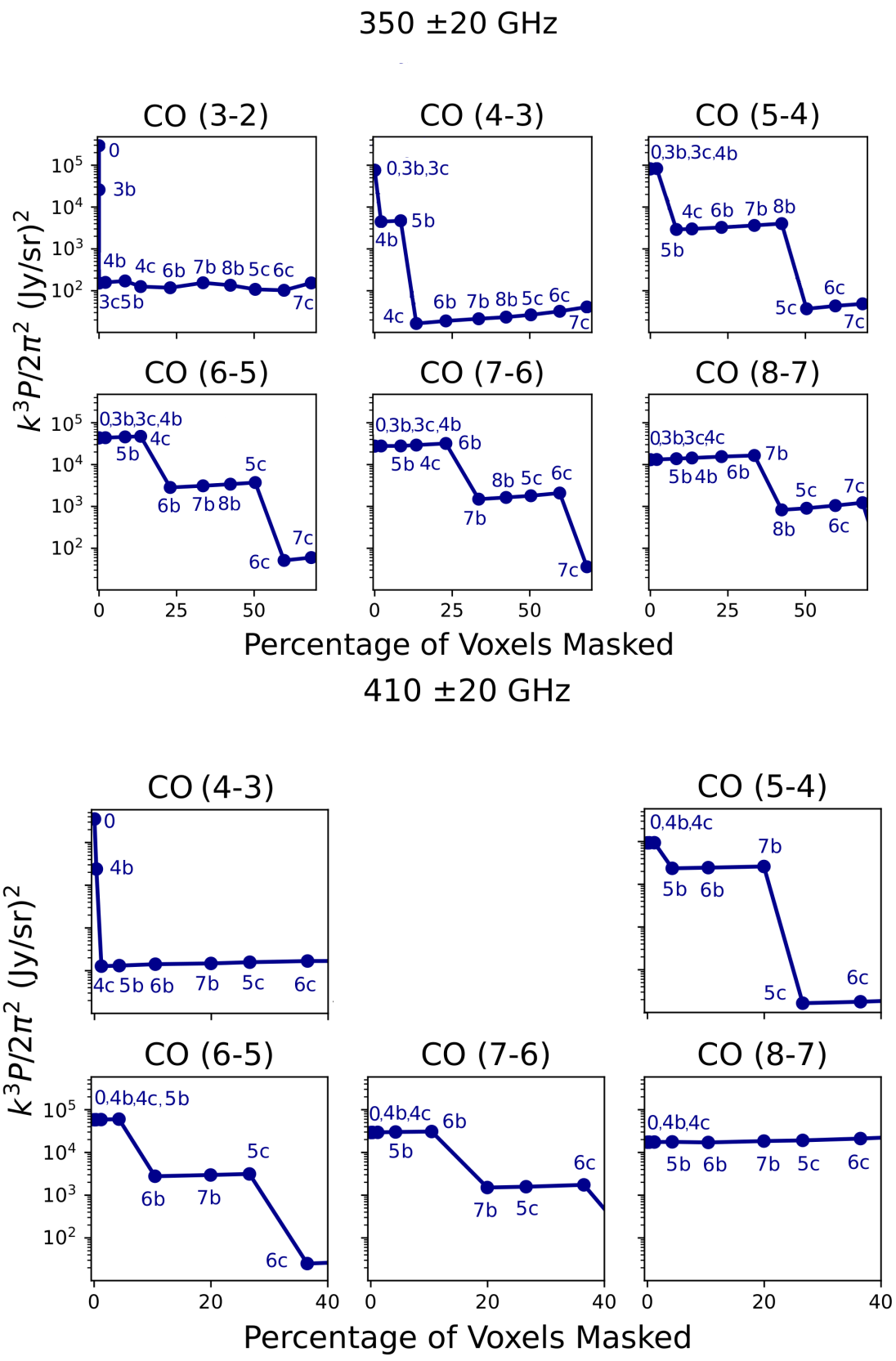

Fig. A1: Effect of masking on the PS of the brightest individual CO lines ($J_{up} = 3 - 8$). The lines represent our fiducial model, with the same optimal masking sequence applied as in Fig. 9 and Fig. 11. The results are plotted for the frequency ranges 225 ± 40 GHz (corresponding to $z_{[CII]} = 7.4$), 280 ± 40 GHz ($z_{[CII]} = 5.8$), 350 ± 40 GHz ($z_{[CII]} = 4.3$), and 410 ± 40 GHz ($z_{[CII]} = 3.7$).

List of Figures

Acknowledgements

I would like to thank Benjamin for always pushing me to be the best version of myself. I am deeply grateful to Frank for his unwavering support in all my plans and for never denying me an opportunity.Emilio for always being there every time I needed to discuss something about science and carrier –or even something random. Also I would like to thank my office-mate Tsan-Ming: without his friendship, support and positive attitude I would not have survived the lock-down.

I would like to thank our secretaries, Christina and Sabine, not only for helping me navigate the German bureaucracy but also for bringing such positive energy to our institute.

Over the years, I have made many friends and traveled to many places. I want to thank Ankur, Maude, and Vyoma for our great times in NYC; Eleni and Eric for always joining me for lunch; Kevin for the fun times in so many different places; Mary for the wonderful memories in Morocco; Jens for the unforgettable time in Atacama; Cosima for hiking with me in Patagonia; Angie for the great time in Valencia; Jakob for the adventures in Granada; Enrico for our fun trip to Croatia; Victoria for attending concerts with me; David for hosting the best parties; Dianna and Ivana for taking driving lessons together; Abel for organizing poker nights; Kostas for an unforgettable Greek Easter; Hasan for keeping me up-to-date; and Toma and Vlad for all the crazy conversations. I would also like to especially thank Karolina, who has always been there for me since we met in Leiden.

I would like to express my gratitude to Dongwoo, Dominik, and Gordon for their relentless efforts in advancing the EoR-Spec science with me over the years.

I am grateful for the financial support through the DFG Collaborative Research Centre 956, Project number 184018867.

A special thanks goes to Chrysa, Yannick, and Paris for being my family away from home, and to Sven for our long bike trips together.

I am deeply grateful to my family: Giorgos, Areti, Giorgakis, Anastasia, Natasa, Lampros, Dora, Giorgis, and Thanasis, as well as Alexandros, my friend since school, for their constant support.

And last but not least, I want to thank myself for doing all the hard work and for never quitting.